2019

Design of two-dimensional material-based electrocatalysts via hetero-interface engineering

Yaping Chen
University of Wollongong

UNIVERSITY
OF WOLLONGONG
AUSTRALIA

Design of two-dimensional material-based electrocatalysts via hetero-interface engineering

Yaping Chen

Supervisors:

Prof. Shi Xue Dou & Dr. Wenping Sun

This thesis is presented as part of the requirement for the conferral of the degree:

Doctor of Philosophy

University of Wollongong

School of Physics

November 2019

Abstract

With ever-incresing concern about energy crisis, environmental pollution, and climate change, seaking for clean and renewable energy sources has become one of the biggest challenges for the sustainable development of society. The key to address this concern is the development of advanced energy conversion technologies, such as water electrolysis for hydrogen generation, fuel cells, and metal-air batteries. Developing high−efficient electrocatalysts for the next-generation energy conversion devices has become a primary focus of research. Since two-dimensional (2D) graphene was discovered, numerous 2D nanomaterials have aroused more research interest in the fields of energy conversion and storage. In particular, the novel 2D nanomaterials have become one of the most promising components for design and development of heterogenous electrocatalysts because of their unique physicochemical properties and adjustable electronic structure. However, some 2D nanomaterials are not active enough because of the large reaction free energy, low amount of active sites or poor conductivity. Some 2D materials are inert for electrocatalysis reactions, but are able to work as the functional substrates for the development of hybrid electrocatalysts. Thus, specific strategies are urgently desired to modulate the physicochemical and surface/interface properties of 2D material-based electrocatalysts, and to make full use of the functionalities of functional 2D material substrates to achieve fast catalytic reaction kinetics. In this regard, hetero-interface engineering strategy has been deployed into designing and preparing three different 2D material-based elctrocatalysts with well-defined interfaces for the enhanced oxygen evolution reaction (OER), hydrogen evolution reaction (HER), and oxygen reduction reaction (ORR).

For the first work, the superhydrophilic GCN/$Ni(OH)_2$ (GCNN) heterostructures with monodispersed $Ni(OH)_2$ nanoplates strongly anchored on GCN were synthesized for enhanced water oxidation catalysis. Owing to the superhydrophilicity of functionalized GCN, the surface wettability of GCNN (contact angle 0°) was substantially improved as compared with bare $Ni(OH)_2$ (contact angle 21°). Besides, GCN nanosheets can effectively suppress $Ni(OH)_2$ aggregation to help expose more active sites. Benefiting from the well-defined catalyst surface, the optimal GCNN hybrid showed a significantly enhanced electrochemical performance over bare $Ni(OH)_2$ nanosheets, although GCN is electrochemically inert. In addition, similar performance promotion resulting from wettability improvement induced by the incorporation of hydrophilic functionalized GCN was also successfully demonstrated on $Co(OH)_2$.

For the second work, we design and synthesize new molybdenum dichalcogenide-based heterostructures with the basal planes decorated with SnS_2 quantum dots towards enhanced alkaline HER activity. The

electrochemical results reveal that the alkaline hydrogen evolution kinetics of molybdenum dichalcogenides is substantially accelerated after incorporation of SnS_2 quantum dots. The optimal $MoSe_2/SnS_2$ heterostructure delivers a much lower overpotential of 285 mV than $MoSe_2$ (367 mV) to reach a current density of 10 mA cm^{-2} in 1 M KOH. The improved catalytic activity is predominantly owing to the enhanced water dissociation kinetics of the heterostructures with well-defined interfaces. Density functional theory (DFT) calculations reveal that the presence of SnS_2 significantly promotes the water adsorption capability of $MoSe_2$ nanosheets, which consequently facilitates the subsequent water dissociation process. These results open up a new avenue for the rational design of well-defined heterostructures with enhanced water adsorption/dissociation capability for the development of high-performance alkaline HER electrocatalysts.

For the third work, hexagonal boron nitride (h-BN) nanosheets are for the first time developed as the multifunctional supports for constructing durable and efficient heterostructured electrocatalysts for oxygen reduction reaction (ORR). As a proof-of-concept application, h-BN/Pd heterostructured electrocatalysts are designed and synthesized by assembling Pd nanoparticles (NPs) on ultrathin h-BN nanosheets towards enhanced ORR kinetics. Firstly, the robust h-BN serves as a durable platform to ensure the structural integrity of the heterostructured catalyst, uniform distribution of Pd NPs and maximal exposure of the active sites. More importantly, the h-BN is capable of modulating the electronic structure of Pd active centers by establishing unique heterostructrued interfaces, downshifting the position of Pd d-band center accordingly and eventually optimizing the affinity with the reaction intermediates for faster reaction kinetics. Meanwhile, the presence of h-BN can also contribute to the creation of a superhydrophobic surface of the heterostructured catalysts, promoting the adsorption capability and diffusion kinetics of O_2. Benefiting from the favorable characters enabled by the multifunctional h-BN support, the heterostructured catalyst delivers exceptional ORR catalytic performance with a high half-wave potential, enhanced mass and specific activity, and decent durability.

In summary, three different heterostructured electrocatalysts with well-defined interface have been designed and synthesized for enhanced OER, HER, or ORR kinetics. The constructionof heterointerface can induce novel physicochemical properties and synergistic effects, which efficiently optimize the affinity/interaction with reactants, intermediate species, or products, further facilitating the electrocatalytic kinetics. Thus, I believe this thesis can open new avenues for the rational design and development of heterostructured electrocatalysts with well-defined interfaces based on 2D materials and

beyond towards a wide range of electrocatalysis applications.

Acknowledgments

I want to say a big thank you to Dr. Wenping Sun, for his professional guidance, substantial support and help, and timely encouragement all the time. He always encourages me and offers valuable advice when I encounter obstacles during my study process. He patiently and continuously guides me how to make the correct and good science, and logically analyse and process my experiment data, which are highly beneficial to me. He directs the way forward in my PhD life. Therefore, I can definitely say that I am the luckiest and happiest student to have his earnest and tireless education.

I would also like to earnestly express gratitude to Prof. Shi Xue Dou. Prof. Dou provides such an excellent platform for my doctoral research career. He professionally guide and support my research all the time, and gives very valuable suggestion for my manuscripts. It is because of his support that I can smoothly complete my doctoral thesis. I also wish to thank Prof. Huakun Liu for her kindly help and support. She creates a happy family to make everyone in ISEM unity love, positive and uplifting.

I want to sincerely express my appreciation to all the co-authors, including A/Prof. Xusheng Zheng, Dr. Peixin Cui, Prof. Haibo Yu, and Dr. Xingyong Wang for their great contributions for my research. With their help, I learned much more for XAFS analysis and DFT calculations, and these are very important to improve my research work. I also should take this opportunity to express my thanks to Dr. Xun Xu, Dr. Patricia Hayes, Dr. Zhenwei Yu, and Dr. Kosta Konstantinov for their training on experimental devices and Dr. Dongqi Shi for his XPS measurement. I would also like to give my appreciation to Dr. David Mitchell, who taught me the TEM technique and some basic knowledge, and Dr. Gilberto Casillas-Garcia, who provided his precious time for the TEM test. I also want to thank Dr. Tony Romeo for his SEM training. I have to thank all the staffs and technicians, Prof. Xiaolin Wang, Dr. Germanas Peleckis, Dr. Tania Silver, Mrs. Crystal Mahfouz, Mrs. Narelle Badger, and Mrs. Naomi Davies for administrative support, and Dr. Candace Gabelish and Mrs. Joanne George, who contribute their strength for the ISEM construction.

Sincerely, I would like to show my appreciation toward my groupmates: Prof. Kun Rui, Prof. Yu Zhang, Dr. Dan Zhang, Mrs Qian Zhou, Miss Mengmeng Lao, Mr Guoqiang Zhao, Mr Xiaobo Zheng, Mr Peng Li, Mr Jiayi Chen, Mr Xiaowei Wang, Mr Xin Li, and Dr. Shaolan Wang for their help and support in my academic careers. I truly appreciate to my close friends, Dr. Wenchao Zhang and Dr. Enhui Wang for their encouragement, help and happy sharing with me. I also wish to thank Mr. Borui Liu, Dr. Binwei Zhang, Dr. Mingzhe Chen, Mr. Zichao Yan, Mr. Qi Zhang, Dr. Yuhai Dou, Dr. Lei Zhang, Dr. Weihong

Acknowledgments

Lai, Mr Zhi Zheng, Miss Yanxia Wang, Miss Jingjing Yu, Dr. Haipeng Guo, Dr. Long Ren, Miss Ningyan Cheng, Mrs Xiaolin Sun, Miss Qiuran Yang, and Miss Daolan Liu for their very great help during my PhD careers. I also thank Mr. Wei Ding for his supportive caring, loving, and sharing all the time.

The most should be grateful to my families, including my parents, sisters and brother. My parents raised me up and always believed in and supported me to pursue my dreams. My sisters and brother always support and encourage me in whatever way they could during my pursuits. I would certainly say that they continue to be the onward impetus and push me forward.

Finally, the author is grateful for financial support from the Australian Research Council (ARC) DECRA Grant (DE160100596), AIIM FOR GOLD Grant (2017, 2018). Especially thank the funding support from the China Scholarship Council (CSC).

Certification

I, Yaping Chen declare that this thesis submitted in fulfilment of the requirements for the conferral of the degree Doctor of Philosophy from the University of Wollongong, is wholly my own work unless otherwise referenced or acknowledged. This document has not been submitted for qualifications at any other academic institution.

_____

Yaping Chen

1st November 2019

List of Names or Abbreviations

0D	Zero-dimensional
1D	One-dimensional
2D	Two-dimensional
3D	Three-dimensional
CA	Contact angle
CFP	Carbon fibre paper
CNT	Carbon nanotube
CV	Cyclic voltammetry
DFT	Density function theory
DOS	Density of state
ECSA	Electrochemical specific area
EDS	Energy-dispersive X-ray spectroscopy
EELS	Electron energy loss spectroscopy
EXAFS	Extended X-ray absorption fine structure
FFT	Fast Fourier transform
FT-IR	Fourier-transform infrared spectroscopy
FTO	Fluorine-doped tin oxide
GCN	Graphitic carbon nitride
GC	Glassy carbon
GO	Graphene oxide
h-BN	Hexagonal boron nitride
HER	Hydrogen evolution reaction
HAADF	High angle annual dark field image
HMOT	Hückel molecular orbital theory
HRTEM	High resolution transmission electron microscopy
ICP	Inductively coupled plasma
ITO	Indium tin oxide
LDH	Layered double hydroxide

LSV	Linear sweep voltammetry
NF	Nickel foam
OER	Oxygen evolution reaction
ORR	Oxygen reduction reaction
RDE	Rotating disk electrode
RDS	Rate determining step
RGO	Reduced graphene oxide
RHE	Reverse hydrogen electrode
SEM	Scanning electron microscopy
SHE	Standard hydrogen electrode
STEM	Scanning transmission electron microscopy
TEM	Transmission electron microscopy
TGA	Thermal gravimetric analysis
TMD	Transition metal dichalcogenide
TMN	Transition metal nitride
TMO	Transition metal oxide
TMOH	Transition metal hydroxide
TMP	Transition metal phosphide
TOF	Turn over frequency
XAFS	X-ray absorption fine structure
XANES	X-ray absorption near edge structure
XPS	X-ray photoelectron spectroscopy
XRD	X-ray diffraction

List of Organizations

ISEM	Institute for Superconducting and Electronic Materials
EMC	Electron Microscopy Centre
AIIM	Australian Institute of Innovative Materials
UOW	University of Wollongong
ARC	Australian Research Council
CSC	China Scholarship Council

Table of Contents

List of Tables, Figures and Illustrations

Tables

Note. [a]N: coordination numbers; [b]R: bond distance; [c]σ^2: Debye-Waller factors; [d] ΔE_0: the inner potential correction. R factor: goodness of fit. S_0^2 was set to 0.829, according to the experimental EXAFS fit of Pd foil reference by fixing CN as the known crystallographic value.

Figures

Chapter 1

1. Introduction

1.1. Research Background

Our rapid energy depletion and serious environmental deterioration have had serious negative effects on the development of modern society in recent years. Finding sustainable sources of energy is highly desirable to meet these challenges, although the unpredictability and intermittency of renewable energy severely limit its utilization efficiency. To efficiently utilize renewable energy, exploiting advanced energy conversion technologies is essential, such as oxygen reduction for liquid fuel generation and water splitting for hydrogen production.[1-4] The key to developing these technologies is research on several electrochemical processes, including the oxygen evolution reaction (OER) or the hydrogen oxygen reaction (HOR) occurring at the cathode, and the hydrogen evolution reaction (HER) or the oxygen reduction reaction (ORR) occurring at the anode (**Figure 1.1**).[5-7] To promote these electrocatalytic processes, designing highly active electrocatalysts is the most crucial factor. Currently, noble metal based catalysts, such as Pt, Ir, and Ru, are extensively utilized as the state-of-the-art electrocatalysts for these electrochemical reactions.[7-11] Nonetheless, they suffer from rarity, high cost, and insufficient stability, which would seriously limit large-scale applications. Therefore, exploring cost-effective alternatives with high performance compared to noble-metal electrocatalysts plays a pivotal role for fundamental research and the practical applications of electrochemical energy storage and conversion technologies.[12]

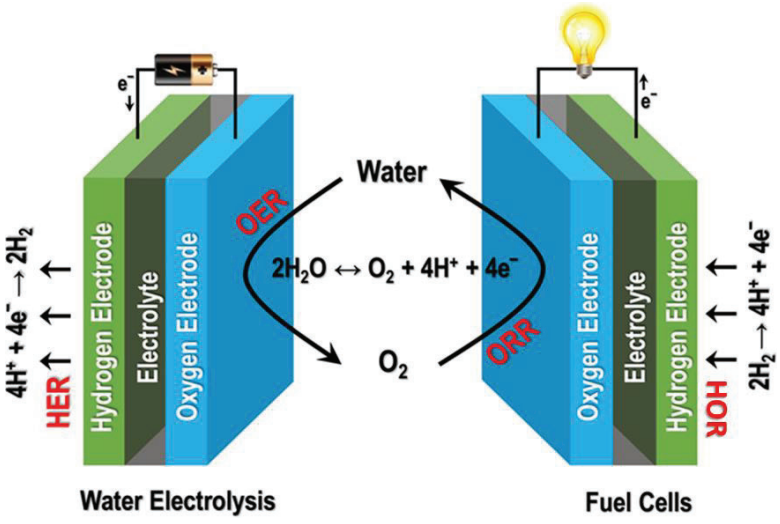

Figure 1.1. Schematic illustration of water splitting and fuel cell reactions. Reproduced with the

permission.[21] Copyright © 2017 American Chemical Society.

Since two-dimensional (2D) graphene was discovered, numerous 2D nanomaterials have aroused an abundance of research interest in the fields of energy conversion and storage.[13-14] In particular, 2D nanomaterials have become one of the most promising candidate materials for the design and development of electrocatalysts, due to their unique physico-chemical properties and electronic structures.[15-18] Some 2D nanomaterials are not active enough, however, because of their poor intrinsic activity, low amount of active sites, or weak conductivity. Some 2D nanomaterials are inert for electrocatalysis, but can act as functional substrates to boost the catalytic activity of hybrid electrocatalysts. Thus, numerous strategies, such as heteroatom doping, heterostructure engineering, geometric tuning, and defect engineering, have been developed to modulate the physico-chemical and electronic properties of 2D material-based electrocatalysts, and to make full use of the functionalities of functional 2D nanomaterial substrates to achieve fast catalytic reaction kinetics.[19-25] Among these modification strategies, engineering hetero-interfaces employing 2D nanomaterial-based matrices could not only modulate their physico-chemical properties and electronic structures, but also endow them with many new properties, such as controllable wettability, excellent electronic conductivity, proper affinity of molecules, decent durability, and structural stability, which are beneficial to the enhancement of electrocatalytic activities.[26-29] Heteroatom doping, as another way of engineering hetero-interfaces, is also an effective route to exploiting novel hybrid electrocatalysts. Generally, the catalytic activities of heteroatom-doped electrocatalysts are limited by the species and numbers of heteroatoms. For example, the catalytic performance of single-doped (N, P, or S-doped) carbon is inferior to that of bi- or tri-doped carbon-based electrocatalysts.[30] In addition to the selection of dopants, the precise control of the doping level of is still challenge.[31]

Thus, engineering heterointerfaces based on 2D nanomaterial matrices is a promising strategy to attain high-efficiency heterostructured electrocatalysts, because it can introduce unique electronic structures and surface/interface properties, which are favourable for the extrinsic and intrinsic activity of electrocatalysts. Specifically, these properties include: (1) maximally exposing and distributing the active sites; (2) shortening the distance for charge/ion migration; (3) changing the local coordination environment of active centres; and (4) optimizing the adsorption energy of reactants and intermediates. Based on these favourable properties, great efforts can be profitably undertaken to investigate the structure-activity relationships of heterostructured electrocatalysts.

1.2. Objectives of the Research

In this thesis, three different heterostructured electrocatalysts for enhancement of the OER, HER, and ORR have been designed and investigated. Specifically, functionalized graphitic carbon nitride, g-C_3N_4 (GCN), nanosheets (NSs) have been successfully deployed for constructing 2D GCN/$Ni(OH)_2$ (GCNN) heterostructures with monodispersed $Ni(OH)_2$ nanoplates anchored on the GCN NSs. The superhydrophilic GCN not only endows the hetrostructures with superhydrophilicity, facilitating mass diffusion, but also substantially ensures the exposure of active sites. Meanwhile, the strong interfacial coupling between the robust GCN and $Ni(OH)_2$ can efficiently enhance the electrode performance and structural stability. These favourable merits give GCNN heterostructured electrocatalysts the ability to deliver significantly enhanced catalytic performance towards the OER as compared to bare ultrathin $Ni(OH)_2$ NSs.

2D molybdenum dichalcogenides, in particular, MoS_2 and $MoSe_2$, are very promising nonprecious-metal-based electrocatalysts for the hydrogen evolution reaction (HER) in acidic media. They exhibit inferior alkaline HER activity, however, due to the sluggish water dissociation process. Thus, in order to improve the alkaline HER activity of molybdenum dichalcogenides, we designed novel $MoSe_2/SnS_2$ and MoS_2/SnS_2 heterostructures with SnS_2 quantum dots decorated on the basal planes of the molybdenum dichalcogenides. It has been confirmed by density functional theory (DFT) calculations that the incorporation of SnS_2 brings in substantial enhancement of the water adsorption capability of $MoSe_2$, both on the edge sites and on the basal planes. Thus, benefiting from the enhanced water adsorption/dissociation capability, the well-defined heterostructures delivered significantly accelerated HER kinetics in comparison with pure $MoSe_2$ in alkaline media.

To further investigate whether engineering heterostructures with well-defined interfaces is an effective strategy for obtaining high-performance electrocatalysts, novel hexagonal boron nitride (h-BN)/Pd heterostructured electrocatalysts were obtained by assembling Pd nanoparticles (NPs) on ultrathin h-BN nanosheets towards enhanced ORR kinetics. The results demonstrated that the robust h-BN serves as a durable platform to ensure the structural integrity of the heterostructured catalyst, uniform distribution of Pd NPs, and maximal exposure of the active sites. More importantly, the h-BN is capable of modulating the electronic structure of Pd active centres by establishing unique heterostructured interfaces, downshifting the position of the Pd *d*-band centre accordingly, and eventually optimizing the heterostructure's affinity with the reaction intermediates for faster reaction kinetics. Meanwhile, the

presence of h-BN can also contribute to the creation of a superhydrophobic surface for the heterostructured catalysts, promoting the adsorption capability and diffusion kinetics of O_2. Benefiting from the favourable characters enabled by the multifunctional h-BN support, the heterostructured catalyst delivers exceptional ORR catalytic performance with a high half-wave potential, enhanced mass and specific activity, and decent durability. These findings open a new avenue for the rational design and development of heterostructured catalysts by interface engineering towards electrocatalysis applications.

1.3. Thesis Structure

Engineering heterostructures with well-defined interfaces is an effective strategy to obtain high-performance electrocatalysts. Thus, we designed 2D nanomaterial-based heterostructured electrocatalysts (including GCNN, $MoSe_2/SnS_2$, and h-BN/Pd) with unique interfacial functionalities for enhanced OER, HER, and ORR performance. The effects of unique surface/interface properties and electronic structures on the electrocatalytic performance of these heterostructures were investigated. Thus the outline of this thesis is briefly presented as follows:

Chapter 1 introduces the research background on electrocatalysis and its applications in the energy storage and conversion field, and identifies the significance of constructing heterostructures with well-defined interfaces in this work.

Chapter 2 presents a literature review on OER, HER, and ORR electrocatalysts and the basic theories on their activity, together with recent progress on heterostructured electrocatalysts.

Chapter 3 presents the detailed synthesis methods, as well as the componential, structural, and electrochemical characterization techniques used in this thesis work.

Chapter 4 investigates the functionalized GCN substrate deployed for the construction of 2D GCNN heterostructures with the decoration of monodispersed $Ni(OH)_2$ nanoplates towards enhanced water oxidation.

Chapter 5 presents novel $MoSe_2/SnS_2$ and MoS_2/SnS_2 heterostructures with electrocatalytically inactive SnS_2 quantum dots decorated on the basal planes of molybdenum dichalcogenides towards enhanced alkaline HER activity.

Chapter 6 investigates h-BN as a multifunctional substrate employed for engineering h-BN/Pd heterostructured electrocatalysts towards enhanced ORR kinetics.

Chapter 7 summarizes this thesis and proposes some current challenges and future perspectives for heterostructured electrocatalysts.

1.4. References

[1] S. Chu, A. Majumdar, Nature 2012, 488, 294.

[2] N. S. Lewis, D. G. Nocera, Proceedings of the National Academy of Sciences 2006, 103, 15729-15735.

[3] Z. Yang, J. Ren, Z. Zhang, X. Chen, G. Guan, L. Qiu, Y. Zhang, H. Peng, Chem. Rev. 2015, 115.

[4] W. Zhang, Z. Wu, J. Zhang, G. Liu, N. Yang, R. Liu, W. Pang, W. Li, Z. Guo. 2018, Nano energy 53, 967-974.

[5] A. Mahmood, W. Guo, H. Tabassum, R. Zou, Adv. Energy Mater. 2016, 6, 1600423.

[6] H. Jin, C. Guo, X. Liu, J. Liu, A. Vasileff, Y. Jiao, Y. Zheng, S.-Z. Qiao, Chem. Rev. 2018, 118.

[7] V. R. Stamenkovic, D. Strmcnik, P. P. Lopes, N. M. Markovic, Nat. Mater. 2016, 16, 57.

[8] Y. Lee, J. Suntivich, K. J. May, E. E. Perry, Y. Shao-Horn, J. Phys. Chem. Lett. 2012, 3, 399-404.

[9] S. H. Ahn, H. Tan, M. Haensch, Y. Liu, L. A. Bendersky, T. P. Moffat, Energy Environ. Sci. 2015, 8, 3557-3562.

[10] N. K. Chaudhari, J. Joo, B. Kim, B. Ruqia, S.-I. Choi, K. Lee, Nanoscale 2018, 10.1039/C8NR06554C.

[11] W. T. Hong, M. Risch, K. A. Stoerzinger, A. Grimaud, J. Suntivich, Y. Shao-Horn, Energy Environ. Sci. 2015, 8, 1404-1427.

[12] P. Xiao, W. Chen, X. Wang, Adv. Energy Mater. 2015, 5, 1500985.

[13] Yang, Z.; Ren, J.; Zhang, Z.; Chen, X.; Guan, G.; Qiu, L.; Zhang, Y.; Peng, H., Chem. Rev. 2015, 115 (11), 5159-5223.

[14] Zhang, H., ACS Nano 2015, 9 (10), 9451-9469.

[15] Xue, Y.; Zhang, Q.; Wang, W.; Cao, H.; Yang, Q.; Fu, L., Adv. Energy Mater. 2017, 7, 1602684.

[16] Tao, H.; Gao, Y.; Talreja, N.; Guo, F.; Texter, J.; Yan, C.; Sun, Z., J. Mater. Chem. A 2017, 5 (16), 7257-7284.

[17] Zhou, Q.; Chen, Y.; Zhao, G.; Lin, Y.; Yu, Z.; Xu, X.; Wang, X.; Liu, H. K.; Sun, W.; Dou, S. X., ACS Catal. 2018, 8 (6), 5382-5390.

[18] Wang, Y.; Mao, J.; Meng, X.; Yu, L.; Deng, D.; Bao, X., Chem. Rev. 2019, 119 (3), 1806-1854.

[19] Chen, G.; Xu, C.; Huang, X.; Ye, J.; Gu, L.; Li, G.; Tang, Z.; Wu, B.; Yang, H.; Zhao, Z.; Zhou, Z.; Fu, G.; Zheng, N., Nat. Mater. 2016, 15, 564.

[20] Choi, C. H.; Kim, M.; Kwon, H. C.; Cho, S. J.; Yun, S.; Kim, H.-T.; Mayrhofer, K. J. J.; Kim, H.; Choi, M., Nat. Commun. 2016, 7 (1), 10922.

[21] Han, L.; Dong, S.; Wang, E., Adv. Mater. 2016, 28 (42), 9266-9291.

[22] Tang, C.; Wang, H.-F.; Chen, X.; Li, B.-Q.; Hou, T.-Z.; Zhang, B.; Zhang, Q.; Titirici, M.-M.; Wei, F., Adv. Mater. 2016, 28 (32), 6845-6851.

[23] Strmcnik, D.; Lopes, P. P.; Genorio, B.; Stamenkovic, V. R.; Markovic, N. M., Nano Energy 2016, 29, 29-36.

[24] Seh, Z. W.; Kibsgaard, J.; Dickens, C. F.; Chorkendorff, I.; Nørskov, J. K.; Jaramillo, T. F., Science 2017, 355 (6321), eaad4998.

[25] Novoselov, K. S.; Mishchenko, A.; Carvalho, A.; Castro Neto, A. H., Science 2016, 353 (6298), aac9439.

[26] G. Zhao, K. Rui, S. X. Dou, W. Sun, Adv. Funct. Mater. 2018, 28, 1803291.

[27] W. Xu, Z. Lu, X. Sun, L. Jiang, X. Duan, Acc. Chem. Res. 2018, 51, 1590-1598.

[28] M. P. Browne, Z. Sofer, M. Pumera, Energy Environ. Sci. 2019, 10.1039/C8EE02495B.

[29] Q. Fu, X. Bao, Chem. Soc.Rev. 2017, 46, 1842-1874.

[30] H. Wang, H. Feng, J. Li, Small 2014, 10, 2165-2181.

[31] Y. P. Zhu, C. Guo, Y. Zheng, S.-Z. Qiao, Acc. Chem. Res. 2017, 50, 915-923.

Chapter 2

2. Literature Review

2.1. The history of electrocatalysis

Electrocatalysis is a type of catalysis that can improve the rate of electrochemical reaction occurring at the interface of electrode and electrolyte. It concentrates on researching the structure-activity relationships and mechanism in electrocatalytic reaction. The term of electrocatalysis was firstly used in a English scientific paper by Grubb in 1963 due to the investigation of fuel cell.[1] It was further claimed by Frumkin et al.[2] The rate of electrochemical reaction determines the efficiency of fuel cell. Thus, it can be inferred that the electrocatalysis was promoted by rising of fuel cells in the 1960s. The electrocatalytic pathway was firstly put forward and taken into practice by Bowden and Rideal in 1928.[3] To implement proof of concept, they deployed various catalysts into the same electrochemical reaction for hydrogen generation. At that time, they mainly focused on the fundamental experiment, rather than the relationship between catalysts and activities. Until 1935, theory anticipation was taken into interpreting the experimental results.[1] The famous theory that the adsorption energy of hydrogen proton strongly depends on the interaction between hydrogen atom and metal, is still adopted up to now in electrocatalytic field. The theory was further applied in the HER which possesses the simple mechanism and provides accessibly supporting experiment data. Thus, following the Butler's attempt,[4] Parsons[5] and Gerischer[6] completely applied the Horiuti and Polanyi's theory into hydrogen evolution reaction in the 1950s to confirm catalytic activity closely associated with the hydrogen adsorption energy.

With the development of electrocatalysis, different types of catalytic reactions and electrocatalysts spring up. Specifically, the investigation of electrocatalysts has attracted more attentions than that of the electrocatalytic reactions, although the various electrocatalytic reactions with the most important benefit in the practical application should be more in-depth research. In general, the electrocatalytic reactions mostly focused on water splitting involved in oxygen[7]and hydrogen evolution[8], oxygen reduction,[9] hydrogen peroxide production,[10] carbon dioxide reduction,[11] nitrogen reduction (NRR),[12] and carbon fuels oxidation like formic acid and methanol. In this regard, the classic Horiuti and Polanyi's theory has been applied to the various electrocatalytic reactions to establish the relationship between the activity and electrocatalysts, which can expressed by means of the binding energy of the intermediates on the surface of catalysts. Besides, some researchers empirically introduced the volcano-shaped plot to establish the

correlation of chemical reaction rate with the adsorption properties such as adsorption enthalpy. Thereafter, the "Volcano" plots were applied in other electrocatalytic reactions as descriptors of the adsorption energy of intermediates vs. catalytic reaction rate. So far, the conceptual electrocatalysis has been developed from hydrogen evolution to bioelectrocatalysis and photo-electrocatalysis, as well as from bulks or polycrystalline blocks to nanoparticles, clusters, quantum dots, single atoms, single crystals, (non)metal alloys, amorphous materials, oxides. Meanwhile, these developments have efficiently improved the progress of materials science.

2.2. The theories of OER, HER, and ORR

2.2.1. The mechanism for OER

The mechanism of OER is still intricate and debatable on metal oxide surfaces. Normally, the reaction has been proposed as four proton/electron-coupled processes in acid and alkaline electrolyte solutions. In acidic media, the four reaction steps of OER are considered to occur as follows,

$$H_2O + {}^* \leftrightarrow OH^* + H^+ + e^- \quad (2.1)$$

$$OH^* \leftrightarrow O^* + H^+ + e^- \quad (2.2)$$

$$O^* + H_2O \leftrightarrow OOH^* + H^+ + e^- \quad (2.3)$$

$$OOH^* \leftrightarrow O_2 + {}^* + H^+ + e^- \quad (2.4)$$

where * represents the active sites of catalysts, and O*, OH*, OOH* denote adsorbed intermediates. Similarly, the reaction pathways can be shown as the following elementary steps in alkaline media:

$$OH^- + {}^* \leftrightarrow OH^* + e^- \quad (2.5)$$

$$OH^* + OH^- \leftrightarrow O^* + H_2O + e^- \quad (2.6)$$

$$O^* + OH^- \leftrightarrow OOH^* + e^- \quad (2.7)$$

$$OOH^* + OH^- \leftrightarrow O_2 + {}^* + H_2O + e^- \quad (2.8)$$

According to aforementioned equations, each elementary step generates one electron. [13-14]

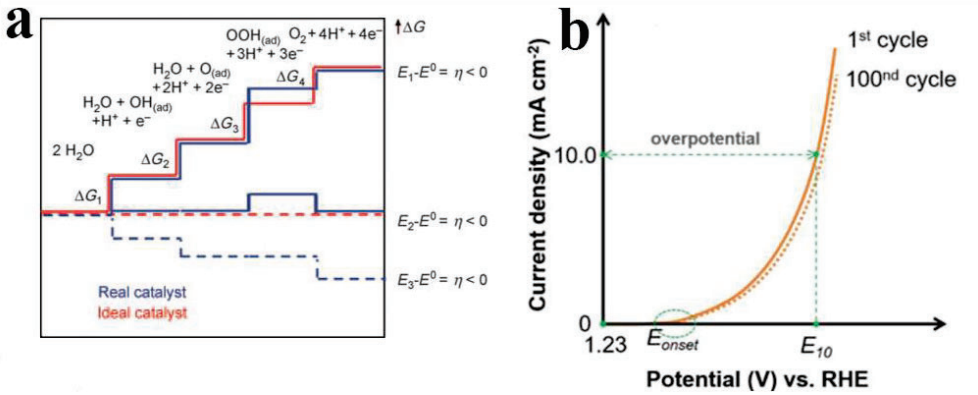

Figure 2.1. (a) Free energy diagram for OER, indicating the reactive species and intermediates. The dashed lines indicate downhill energetics for all steps at the electrode potential (i.e. thermochemical overpotential); ΔGi denotes the free reaction energy of each elementary reaction step. Reproduced with the permission.[15] Copyright © 2010 WILEY‐VCH Verlag GmbH & Co. KGaA, Weinheim. (b) A schematic polarization curve for OER. Reproduced with the permission.[16] Copyright © 2016 WILEY‐VCH Verlag GmbH & Co. KGaA, Weinheim.

Beyond the early concepts mentioned above, density functional theory (DFT) calculations have been adopted more recently to highlight the thermochemical aspects of OER.[15-16] The free reaction energy of the elementary reactions (ΔG_i) was used for thermochemical analysis. As depicted in **Figure 2.1a**, the Gibbs reaction energy order $\Delta G_3 > \Delta G_1 = \Delta G_2 > \Delta G_4$ indicates that the formation of the peroxide intermediate (ΔG_3) is the thermochemically least favorable step, while ΔG_3 and ΔG_4 are considered as the "potential-determining steps" controlling the activation energy. Theoretically, the ΔG_i of the overall reaction is equal to that of the sum of four-step elementary reaction with the same ΔG_i for an ideal catalyst, resulting in a same equilibrium voltage E =1.23 eV (4.92 eV/4 = 1.23 eV) vs RHE (reversible hydrogen electrode, afterwards all the potential noted is in terms of RHE, unless otherwise specified). In reality, however, there is still no ideal catalyst to achieve the same ΔG_i of each step, thus generating the overpotential of OER.

To evaluate and compare the performance of target electrocatalysts, overpotential or onset potential is considered as one of the most fundamental parameters. Since it is quite arbitrary to experimentally determine the precise value of onset potential, the value of potential at a current density of 10 mA cm^{-2} (E_{10}) is applied more frequently.[17] Overpotential is the difference between the equilibrium potential (E_0=1.23 V) and E_{10}. As indicated by typical polarization curves in **Figure 2.1b**, the current density tends to remain zero before reaction activated, and start increasing at the onset potential before a sharp

increase.[16]

Tafel slope is another parameter employed to provide insights into the reaction kinetics and electrocatalytic activity.[17] Specifically, Tafel slope contributes to elucidating the rate-determining step by employing the following equation.

$$\eta = b \cdot log(j/j_0) \quad (2.9)$$

Where η represents overpotential, b denotes the Tafel slope, j stands for current density and j_0 is exchange current density. In general, a smaller Tafel slope with faster increase in current density (j) is desired.

2.2.2. The mechanism for HER

HER is a typical two-electron transfer reaction in acid and alkaline solutions. In a cidic media, the reaction steps of HER are presented as follows:

Volmer step: $H^+ + {}^* + e^- \rightarrow H^*$ (2.10)

Heyrovsky step: $H^+ + {}^* + e^- + H^* \rightarrow H_2 + {}^*$ (2.11)

Tafel step: $2H^* \rightarrow H_2 + 2^*$ (2.12)

Where * represents the active sites of catalysts, and H* denote adsorbed hydrogen intermediates. Similarly, the reaction pathways can be displayed as the following elementary steps in alkaline media:

Volmer step: $H_2O + {}^* + e^- \rightarrow OH^- + H^*$ (2.13)

Heyrovsky step: $H_2O + {}^* + e^- + H^* \rightarrow H_2 + {}^* + OH^-$ (2.14)

Tafel step: $2H^* \rightarrow H_2 + 2^*$ (2.15)

According to aforementioned equations, it can be explicit for the hydrogen intermediates originated from hydronium ion or water dissociation in the different electrolyte. Then, the H^* would form H_2 by the Heyrovsky or Tafel step. In actual electrocatalytic reactions, the reaction pathway strongly depends on the physicochemical properties and electronic states of catalyst surface.

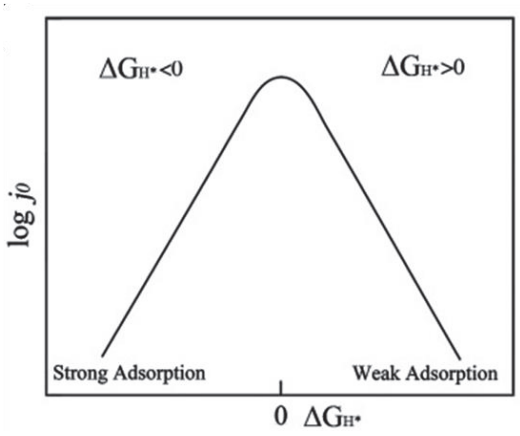

Figure 2.2. Relationship between j_0 and ΔG_H. Reproduced with the permission.[22] Copyright © 2015 WILEY‐VCH Verlag GmbH & Co. KGaA, Weinheim.

Generally, the HER activity can be directly evaluated by the parameters of overpotential, Tafel slopes, and TOF, which all can obtained from the electrochemical test. The hydrogen adsorption free energy, ΔG_H, the assessment of the HER kinetic, can be calculated by density functional theory (DFT). According to the Sabatier principle expressed by the volcano-shaped plot (**Figure 2.2**), the most active electrocatalyst (shown by exchange current density, j_0) is that the binding strength of hydrogen should be neither too weak nor too strong. [19-22] If the binding strength of hydrogen intermediates adsorbed on the electrode surface is too weakly, the Volmer step correlated with the overall reaction rate would be limited, while if binding strength is too strong, the Heyrovsky/Tafel step, i.e. the desorption step, would be restricted. Therefore, the necessary but not sufficient condition to achieve the optimal HER kinetics is ti_H is .[5, 18, 23, 24]

2.2.3. The mechanism for ORR

The oxygen reduction can occur through a two-electron ($2e^-$) transfer pathway to form the hydrogen peroxide in alkaline media or hydroperoxyl (HO_2^-) in acidic media, or by means of a four-electron ($4e^-$)transfer process to directly produce water.

Dissociative ($4e^-$):

$$O_2 + 2^* \quad O \tag{2.16}$$

$$2O^* + 2H^+ + 2e \tag{2.17}$$

$$2OH^* + 2H^+ + 2e \quad {}_2O + 2^* \tag{2.18}$$

Associative ($4e^-$):

$$O_2 + ^* \quad {}_2^* \tag{2.19}$$

$$O_2^* + H^+ + eH \tag{2.20}$$

$$OOH^* + H^+ + e \quad {}_2O \tag{2.21}$$

$$O^* + H^+ + e \tag{2.22}$$

$$OH^* + H^+ + e \quad {}_2O + ^* \tag{2.23}$$

Associative ($2e^-$):

$$O_2 + ^* O \ {}_2^* \tag{2.24}$$

$$O_2^* + H^+ + eH \tag{2.25}$$

$$OOH^* + H^+ + e \quad OOH^- + ^* \tag{2.26}$$

The selectivity of $2e^-$ or $4e^-$ process mainly depends on the free reaction energies of adsorbed intermediates on the electrode surface.[25] From the view of molecule, the direct $4e^-$ mechanism can proceed as two possible ways, dissociative or associative pathways. The primary distinction of the two

mechanisms is engineering different O_2 dissociation energy barrier. Such as, it has been demonstrated by DFT calculations that the dissociation barriers are so high on the carbon surface that the reaction proceeds by $4e^-$ dissociative pathway.[26] Thus, that's why almost carbon materials always tend to $2e^-$ reaction rather than $4e^-$.[27-28] In contrast, Pt-based catalysts for ORR process normally take a dissociative route because of the strong original O_2 dissociation energy barrier.[29] It has been evidenced that Pt-based electroctalysts is inclined to the $4e^-$ reaction pathway all the time. In addition, the adsorption energy of oxygen-containing intermediates can also determine the reaction pathway. If the adsorption energy is too weakly, the reaction facilitates $2e^-$ pathway, in verse, the reaction tend to $4e^-$ pathway.[30-31]

Commonly, some indicators like onset potential, half-wave potential ($E_{1/2}$), and diffusion-limiting current density (j_L) can be used as evaluation criteria of ORR performance for various electrocatalysts at the same test conditions. The ORR potential range deviates a lot from the equilibrium potential, and the reaction kinetics are multistep. Thus the exchange current density can not be served as the parameter of assessing performance. Catalytic selectivity can be assessed by the electron transfer number (n), which arecalculated by the Koutecky–Levich equation.[30]

The kinetic current (J_k) can be calculated by the Koutecky–Levich equation which is represented by

$$\frac{1}{J} = \frac{1}{J_k} + \frac{1}{J_d} \tag{2.27}$$

Where J stands for the measured current and J_d for the diffusion limited current.

The number of electrons transferred (n) can be estimated by the Levich equation:

$$J_d = 0.62nFAD^{2/3}\upsilon^{-1/6}\omega^{1/2}C_{O_2} \tag{2.28}$$

where F stands for Faraday's constant (96485 C mol^{-1}). A is the area of electrode (0.196 cm^2), and D is the diffusion coefficient of O_2 in 0.1 M KOH solution (1.93×10^{-5} cm^2 s^{-1}). υ stands for the kinematic viscosity of the electrolyte (1.01×10^{-2} cm^2 s^{-1}). ω represents the angular frequency of rotation: $\omega = 2\pi f/60$, f in r.p.m. is the RDE rotation rate, and C_{O_2} is the concentration of molecular oxygen in 0.1M KOH electrolyte (1.26×10^{-6} mol cm^{-3}).

2.3. 2D electrocatalysts

2D nanomaterials have been extensively applied in the electrocatalysts due to their adjustable and evenly exposed lattice planes, unique physicochemical properties, and electronic structures. These special features can have remarkable influences on the extrinsic and intrinsic activities of electrocatalysts. Apart from the adjustable catalytic activities, 2D nanomaterials can also work as functional supports because of

their large specific surface areas and robustness for the development of hybrid electrocatalysts.[32-38] However, most pure 2D electrocatalysts are inert or not active enough because of the poor intrinsic activity, low density of active sites, and low electrical conductivity. [39-40] Thus, some efficient optimization strategies (including heteroatom doping, surface/interface building, defect constructing, and geometric controlling, etc.) are already proposed for 2D electrocatalysts to achieve higher catalytic activities (**Figure 2.3**).[41] These optimization approaches aim to modulate the surface/interface properties and electronic structures correlated with intermediates adsorption free energy and charge/mass transfer kinetics, which would affect catalytic kinetics.

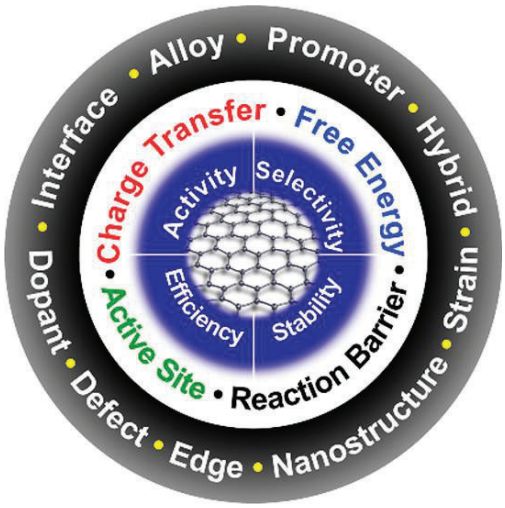

Figure 2.3. The engineering strategies of 2D nanomaterials and their effects on improving electrocatalytic performance.[41] Copyright © 2018 American Chemical Society.

2.3.1. 2D electrocatalysts for OER

2.3.1.1. Transition-metal oxides

In recent years, transition-metal oxides (TMD) like CoO_x, NiO_x, and FeO_x have drawn great attention in electrocatalysis application, due to the high electrocatalytic activity for OER in alkaline solutions. More efforts have already been devoted to boosting the catalytic activity through optimizing the nanostructured morphology and active surface area.[42-45] It is generally acknowledged that higher valence state of nickel and cobalt results in higher OER catalytic activity.[45-46] Thus, various approaches to prepare nickel oxides with higher valence state and improved catalytic performance have been pursued.[47] As a typical example, Zou et al. reported high-valence-state NiO/Co_3O_4 nanoparticles decorated on nitrogen-doped carbon for OER with low overpotential. Rich high-valence Ni^{3+} and Co^{3+} species were dispersed on the surface of the composite electrocatalysts. The combination of higher oxidation states of both Ni and Co

synergistically leads to outstanding OER activity.[48] As mentioned above, the surface Gibbs free energy (ΔG_s) also plays a critical role for water oxidation reaction. Zhang et al. prepared ultrafine NiO nanosheets with a platelet size of ~4.0 nm and thickness of ~1.1 nm stabilized by TiO_2 by calcining monolayer NiTi-layered double hydroxide (LDH) precursor.[49] The successful fabrication of ultrathin NiO heterostructured catalysts achieved high exposure of reactive NiO [50] facets, presence of Ni^{3+} and Ti^{3+} sites, and abundant interfaces, which demonstrated strong synergetic effects to accelerate H_2O adsorption and benefit charge transfer (**Figure 2.4a-c**). In fact, the surface Gibbs free energy (ΔG_s) follows the order of [50] ≈ [51] > [50] > [52] for NiO facets.[53] Surface reactivity, in that case, increases with ΔG_s, making it greatly desirable to fabricate ultrathin and ultra-small NiO nanosheets with more exposed [50] facets for enhanced performance.

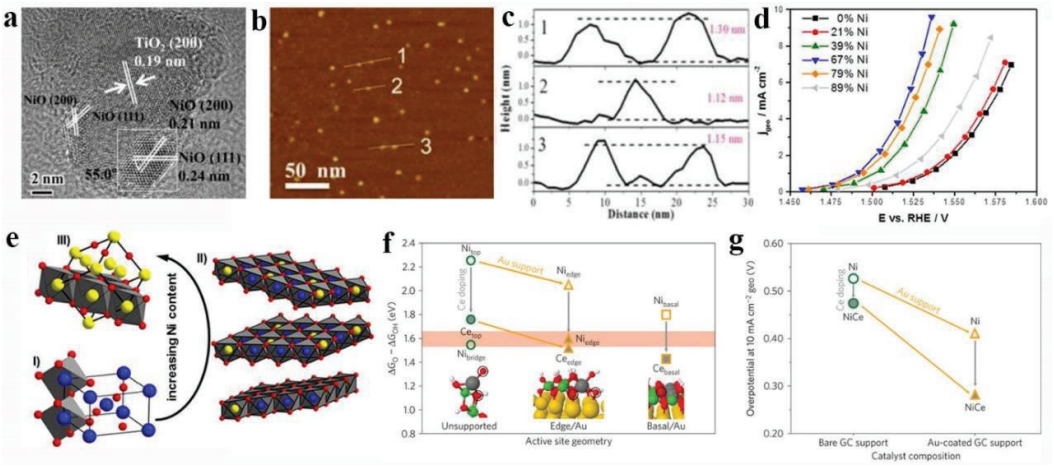

Figure 2.4. (a) HRTEM image of mono-NiTi-MMO. (b) AFM image and (c) corresponding height profiles of mono-NiTi-MMO. Reproduced with the permission.[49] Copyright © 2016 American Chemical Society. (d) iR corrected-LSV curves of Ir−Ni mixed oxide films with different ratios of Ir to Ni, (x% Ni-MO: x represents at% Ni). (e) Structural models representing: (I) rutile type (IrO_2) unit cell, (III) the bunsenite type (NiO) unit cell, and (II) 39%Ni-MO-ap. (red: O or OH; yellow: Ni; blue: Ir). Reproduced with the permission.[61] Copyright © 2015 American Chemical Society. (f) DFT + U calculations demonstrating effects owing to Ce doping, gold support and geometry. (g) Experimental overpotentials for NiO_x and $NiCeO_x$ supported on either bare or Au-coated GC substrates, (yellow: Au; green: Ni; grey: Ce; red: O; white: H). Reproduced with the permission.[62] Copyright © 2016, Springer Nature.

Cation doping is another strategy to improve the catalytic performance.[54-60] For example, well-defined thermally prepared Ir−Ni oxide thin film with a low ratio of Ir showed an unprecedented 20-fold increase in water oxidation activity and enhanced stability over pure Ir oxide electrocatalysts under highly

corrosive acidic conditions (**Figure 2.4d**).[61] Furthermore, an intuitive model for the formation of the catalytically active state of the bimetallic Ir−Ni oxide surface were proposed to identify the coverage of reactive surface hydroxyl groups as a suitable descriptor for the OER activity (**Figure 2.4e**). Later work by Jaramillo et al. demonstrated the remarkable enhancement of OER activity of electrodeposited NiO_x films, which benefited from the synergistic effects of employing Ce as the dopant and gold as the support. Superior OER performance was achieved by the $NiCeO_x$–Au catalyst in alkaline media, which was among the best reported at that time. Based on experimental observations and theoretical modelling, the excellent performance was ascribed to the integration of electronic, geometric and support effects. Modified electronic circumstance of host nickel oxide by Ce doping, leads to beneficial binding energies of the OER intermediates and promoted approach to highly active geometrical-coordinating Ni site simultaneously (**Figure 2.4f-g**).[62]

2.3.1.2. Layered transition-metal hydroxides and double hydroxides

Layered double hydroxides (LDHs) are a class of lamellar materials consist of positively charged layers and charge-balancing interlayer anions. The positively charged layers can be replaced by monovalent cations (Li^+), divalent cations (e.g. Mg^{2+}, Ni^{2+}, Co^{2+}, Mn^{2+}, Cu^{2+}, Ca^{2+}, Zn^{2+} et al) or trivalent cations (e.g. Al^{3+}, Fe^{3+}, Cr^{3+}). The interlayer anions are normally carbonate (CO_3^{2-}), which can easily be substituted by other anions (e.g. SO_4^-, NO_3^-, Cl^- and Br^-).[63-64] Endowed with chemical versatility, open structures as well as high accessibility to electrolytes by anion exchange, LDHs have been extensively investigated as promising candidates for electrochemical applications (e.g. supercapacitors, batteries, water splitting, etc.). In particular, NiFe LDH, has drawn considerable attention as electrocatalysts due to its prominent catalytic activities and stability during OER process.[51-52, 65-66] One of the major advantages of NiFe LDHs is that metal atoms can regularly located on the LDHs flakes to provide abundant exposed active sites. Besides, the features of anion-exchange as well as ease of delamination have provided more opportunities for engineering nanostructured assembly of LDHs towards enhanced OER performance.

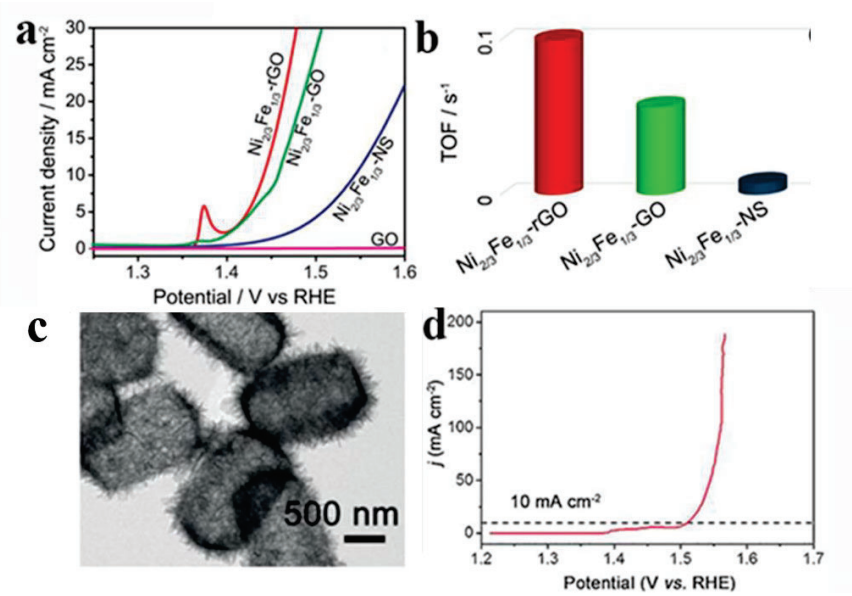

Figure 2.5. (a) Polarization curves of NiFe LDH based composites in 1.0 M KOH media. (b) TOF of $Ni_{2/3}Fe_{1/3}$-rGO, $Ni_{2/3}Fe_{1/3}$-GO, and $Ni_{2/3}Fe_{1/3}$-NS at the overpotential of 0.3 V. Reproduced with the permission.[71] Copyright © 2015 American Chemical Society. (c) TEM image of the hierarchical Ni-Fe LDH hollow nanoprisms. (d) Polarization curve for the Ni-Fe LDH hollow prisms in 1 M KOH media. Reproduced with the permission.[75] Copyright © 2018 Wiley‐VCH Verlag GmbH & Co. KGaA, Weinheim.

However, the low conductivity of LDHs has hindered their practical applications as OER catalysts. To resolve this problem, some researchers attempted to hybridize LDHs with conductive materials such as conductive carbon materials (rGO and CNTs), or directly grow them on conductive substrates (nickel foam and carbon fiber cloth).[67-70] Ma et al. prepared a superlattice-like $Ni_{2/3}Fe_{1/3}$ LDH nanosheets/GO ($Ni_{2/3}Fe_{1/3}$/GO) heterostructured composites via a homogeneous precipitation strategy. The resultant $Ni_{2/3}Fe_{1/3}$/GO delivered excellent OER performance (an overpotenial of 0.23 V at 10 mA cm^{-2}) with a small Tafel slope (42 mV dec^{-1}). The overpotenial can be further decreased to 0.21 V at 10 mA cm^{-2} by hybridizing $Ni_{2/3}Fe_{1/3}$ LDH with rGO. The improvement of catalytic activity can be ascribed to the interfacial interaction between $Ni_{2/3}Fe_{1/3}$ LDH and GO at a molecular level, which hampered the aggregation of LDHs and thus increased the active electrochemical surface areas, generating a synergistic effect for OER (**Figure 2.5a-b**).[71] On the other hand, the OER activity of an electrocatalyst can be optimized by tuning its geometric structure, since the OER process involves a series of surface/interface reactions. Thus, engineering nanostructures such as hollow, porous and complex 3D architectures is highly desirable to further boost the OER activity of Ni-based LDHs.[72-74] Lou's group successfully

synthesized hierarchical hollow nanoprisms composed of ultrathin Ni-Fe LDH nanosheets by self-sacrificing template method. Nickel-precursors tetragonal nanoprisms were employed as templates and dissolved by the hydrolysis of iron(II) sulfate for the simultaneous growth of ultrathin Ni-Fe LDH nanosheets on the surface (**Figure 2.5c**).[75] The wise design of advanced FeNi LDH nanostructures with large surface areas contributed to a low overpotential of 280 mV at 10 mA cm^{-2} (**Figure 2.5d**). The promoted activity can be possibly ascribed to their unique nanostructure and optimized chemical composition. Besides the synergistic effect between Ni and Fe, the hierarchical hollow nanoprisms with large surface areas could provide plenty of active sites for electrochemical reactions.

Meanwhile, other LDHs such as Ni-V monolayer double hydroxide,[50] NiCo LDHs,[76-78] NiMn LDH,[79] NiFeAl,[80] NiFeMn[81] and NiCoAl[82] ternary LDH nanosheets, were investigated for OER in alkaline electrolyte. Sun and co-workers reported a monolayer of nickel–vanadium LDH achieving a current density of 27 mA cm^{-2} (57 mA cm^{-2} after IR correction) driven by an overpotential of 350 mV for OER.[50] These enhanced catalytic activities were ascribed to enhanced conductivity, facilitated electron transfer and increased active sites. Wang and co-workers further reported ternary NiCoFe LDH nanosheets by cation exchange reaction at ambient temperatures.[83] The NiCoFe-LDH electrode reached a current density of 10 mA cm^{-2} with a low overpotential of 280 mV and showed excellent stability after 10 h with a retention rate of 98% in 1 M KOH electrolyte. Although emerging *in-situ* or in operando techniques have been used for in-depth investigation on the electrocatalysts for OER, systematic theoretical studies of the catalytic pathway and active sites of Ni-based LDHs in terms of various compositions and structures remain to be explored.

2.3.1.3. Metal-free OER electrocatalysts

2D metal-free nanomaterials have been extensively investigated in electrochemical energy storage and conversion fields, such as batteries, supercapacitor, and catalysis. As OER catalysts, they exhibit very promising catalytic activity with proper modification. Such as, N,P co-doped graphene/carbon nanosheets (N,P-GCNS) with N,P-doped carbon sandwiching few-layers-thick graphene were fabricated.[84] The N,P-GCNS nanosheets can maximally expose the active sites and highly enhance the conductivity due to the doped N and P. Meanwhile, the large specific surface areas and hierarchical pores can afford rapid transportation pathway and adequate combination between the electrode and electrolyte. As a result, the N,P-GCNS catalyst achieved lower overpotential at 10 mA cm^{-2} with smaller Tafel slope than that of RuO_2 benchmark. Notably, the N,P-GCNS is an effective bi-functional electrocatalysts for the enhanced

ORR process also.

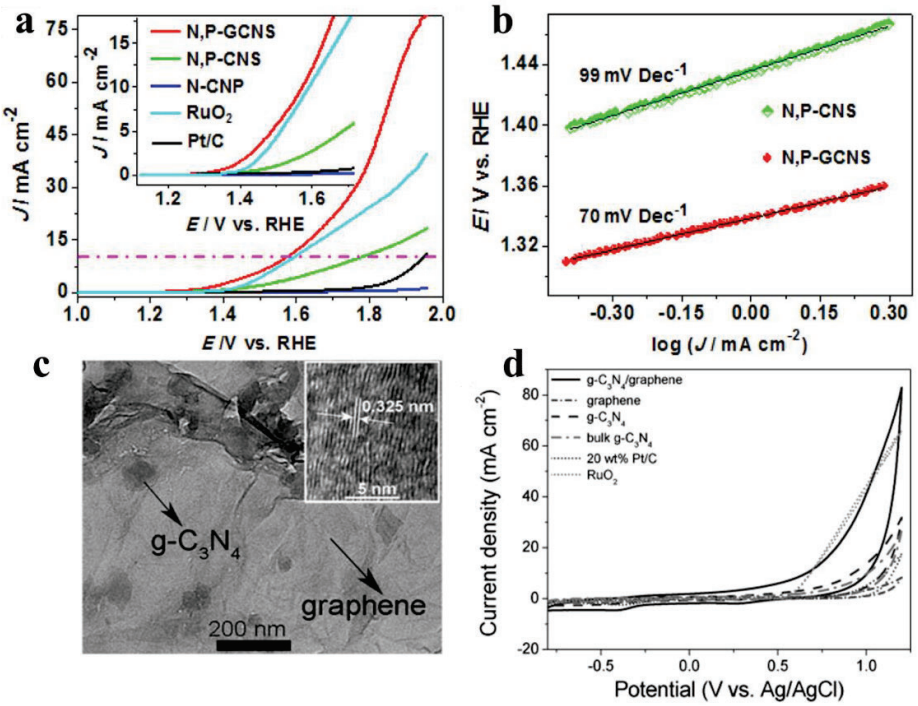

Figure 2.6. (a) The OER activity of various catalysts evaluated by LSV tests. (b) Tafel plots of N,P-CNS and N,P-GCNS. Reproduced with the permission.[84] Copyright © 2015 American Chemical Society. (c) TEM image of g‐C_3N_4/graphene composites (inset: the HRTEM image of a typical g‐C_3N_4 nanosheet). (d) CVs during the ORR and OER potential window of g‐C_3N_4/graphene composites, g‐C_3N_4, bulk g‐C_3N_4, graphene, RuO_2, and 20 wt% Pt/C in N_2‐saturated 0.1 M KOH. Reproduced with the permission.[88] Copyright © 2014 WILEY‐VCH Verlag GmbH & Co. KGaA, Weinheim.

2D graphitic carbon nitride g-C_3N_4 (GCN) has been widely implemented in the photocatalysis field due to its unique electronic band structure and high physicochemical stability.[85] Some effort has already been made to study GCN-based composites as electrocatalysts for water splitting.[86-87] It was found that bare GCN is nearly inert for OER and hydrogen evolution reaction (HER), and the delivered catalytic performance is mainly ascribed to the synergistic effect of GCN and the conductive carbonaceous materials (e.g., CNT and graphene). According to the strategy, ultrathin g-C_3N_4 nanosheets/graphene hybrid has been synthesized under ultrasonication-assisted method.[88] The g‐C_3N_4 and graphene are well hybridized by π‐stacking interactions due to π‐rich characteristics and their 2D configurations. The conductive graphene nanosheets work as high rapid electron‐transporting channels in the hybrid and the graphene nanosheets partially covered by g‐C_3N_4 can ensure effective electrical contacts

between them. Meanwhile, the thickness of g‐C_3N_4 nanosheet is only approximate 1.1 nm, while the largest distance of electron tunnelling is up to be 3 nm, so electrons could pass through the g‐C_3N_4 barrier. In addition, g‐C_3N_4 nanosheets exhibit high chemical stability. Therefore, the g‐C_3N_4/graphene hybrids delivered better OER performance and durability.

2.3.2. 2D electrocatalysts for HER

2.3.2.1. Graphene-based HER electrocatalysts

The basal plane of pristine graphene is inactive for the hydrogen evolution with a large hydrogen adsorption free energy, ΔG_{H^*} (1.85 eV) due to containing no free electrons for reaction.[89] Large positive ΔG_{H^*} means the sluggish HER process, which is corresponding with the experimental results. Therefore, doping graphene with one or more non-metallic atoms to redistribute the charge/spin in combination with the reactants/intermediates adsorption is the most effective strategy for boosting HER performance.[89-91] Among these single-heteroatom-doped graphene nanomaterials, B-doped graphene exhibits exceptional HER performance. But it remains not quite good enough in comparison with the MoS_2-based and Pt-based electrocatalysts. Moreover, it can be found that the Tafel slopes of all heteroatom-doped graphene are in close proximity to 120 mV dec^{-1}, indicating that the rate-determining step is Volmer step also evidenced by DFT calculations. Meanwhile, although doping heteroatoms in graphene can enhance the hydrogen adsorption ability, but the ΔG_{H^*} values are still more than the ideal ones, demonstrating unfavourable thermodynamic adsorption process. Thus, all heteroatom-doped graphene catalysts locate at the right bottom leg of the volcano curves (**Figure 2.7a**).[92] To rank the activity grades of volcano plots, a basic principle of optimizing ΔG_{H^*} was expounded by Qiao and co-authors according to the HMOT. They discovered a good linearity of the DOS peak position and the ΔG_{H^*} by examining the active-center DOS of all models (**Figure 2.7b**).[92] In view of the poor hydrogen adsorption on the built graphene models, the DOS peak position for the active centers should be closer to the Fermi level. Based on the above predication, dual-heteroatom-doped strategies were adopted to optimize the ΔG_{H^*} of graphene-based materials. Such as N,P-, N,S-, N,B-, N,P,S- co-doped graphene-based nanomaterials were designed towards HER process. As predicted, almost dual-atoms doped graphene-based catalysts exhibit accelerated HER performance in comparison with the single-atom doping ones except for N-, B-doped graphene. The results are also in agreement with the DFT calculations of ΔG_{H^*}. As is well-known, the catalytic activity is dominated by the inherent activity of every active site, as well as extrinsic physical and chemical characteristics associated with those exposed active sites. Particularly, for the doped

catalysts, the density of exposed active sites is closely connected with the degree of doping and the specific surface area of electrode. Thus, the HER activities for graphene-based catalysts can be enhanced by controlling the doping level and increasing the specific surface area.

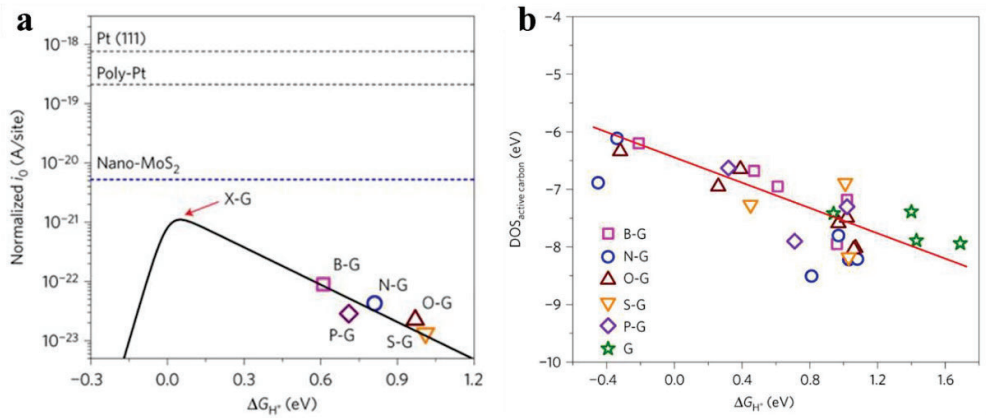

Figure 2.7. (a) HER volcano plots consisting of DFT calculated ΔG_{H*} of intermediates (x-axis) and experimentally tested i_0 (y-axis) as descriptors. (b) The relationship between ΔG_{H*} and the highest peak position of DOS of the active carbon, the red line as a guide. Reproduced with the permission.[92] Copyright © 2016, Springer Nature.

Apart from the above non-metal heteroatom doped graphene to modulate the HER intrinsic activity of graphene-based electrocatalysts, graphene and its derivatives also serve as important platforms for the support of metal nanoparticles, nanoclusters, and single atoms. Especially, the modified graphene substrate uniformly decorated by single atoms has been considered as an effective strategy for synthesizing alternative electrocatalysts to Pt-like non-noble metals. For example, Sun's group synthesized isolated single Pt atoms and clusters dispersed on the surface of N-doped graphene by the atomic layer deposition technique.[93] The N dopants can induce strong electronic interaction and chemical bonding between Pt and graphene matrix, modulating the electronic structure of Pt to facilitate the HER kinetics. The as-synthesized samples delivered better HER performance than that of state-of-the-art Pt/C catalysts. Both the XANES analysis and DFT calculations demonstrate that the N coordination of the isolated Pt single site modulated modulates the electronic structure of Pt and optimized optimizes the hydrogen adsorption energy, and thereby boosting the HER kinetics. Other than noble-metal single atoms, several transition-metal single atoms such as cobalt, nickel single atoms anchored on the functionalized graphene as high-performance HER electrocatalysts were also reported.[94-95] Therefore, doping heteroatoms or supporting active metals on the surface of graphene is both considered as an effective

strategy for engineering high-activity graphene-based electrocatalysts.

2.3.2.2. Transition-metal dichalcogenides

Recently, the development of 2D HER electrocatalysts are mainly concentrated on investigating the TMDs. Molybdenum dichalcogenides, in particular MoS_2 and $MoSe_2$, are the most promising TMDs electrocatalysts for the HER. Therefore, in the following discussion, MoS_2 is taken as a typical example. Both density functional theory (DFT) calculations and experimental findings have demonstrated that the HER catalytic activity of molybdenum dichalcogenides is mainly derived from their edge sites.[96-100] In this regards, various strategies, such as building various nanostructures or phases, engineering surface/interface and defects, or heteroatom doping, are taken to increase the number of exposed active sites, as well as modulate the ΔG_{H^*} and band structure of molybdenum-dichalcogenide-based electrocatalysts for enhanced HER activity.[101-103]

Engineering various nanostructures to increase the specific surface area is the most common method for improving the activity of MoS_2 electrocatalysts, such as constructing nanowires,[104] mesostructures,[105] nanoparticles,[106-107] and nanosheets,[108] etc. Generally, this strategy would not change the electronic states of pure MoS_2, but could physically enlarge the density of active sites to significantly improve the current density. Besides, as with doping graphene, doping heteroatom (e.g., Ni, Co) can alter the electronic properties and enhance the HER kinetics accordingly. Moreover, the identification of doping sites should be precisely confirmed so that to determine the impact on HER performance.[109-110]

Introducing defects of purpose in the MoS_2 basal planes is also an efficient approach to modify the band structures, and crack the basal planes to create more edge sites. For example, Xie's group reported a scalable approach to introduce defects into the surface of MoS_2 to generate more active edges.[111] HRTEM results indicated the relavant unordered atomic arrays on the basal planes, which can cause a cracking of the basal plane and lead to generating more additional edges (**Figure 2.8a-c**).

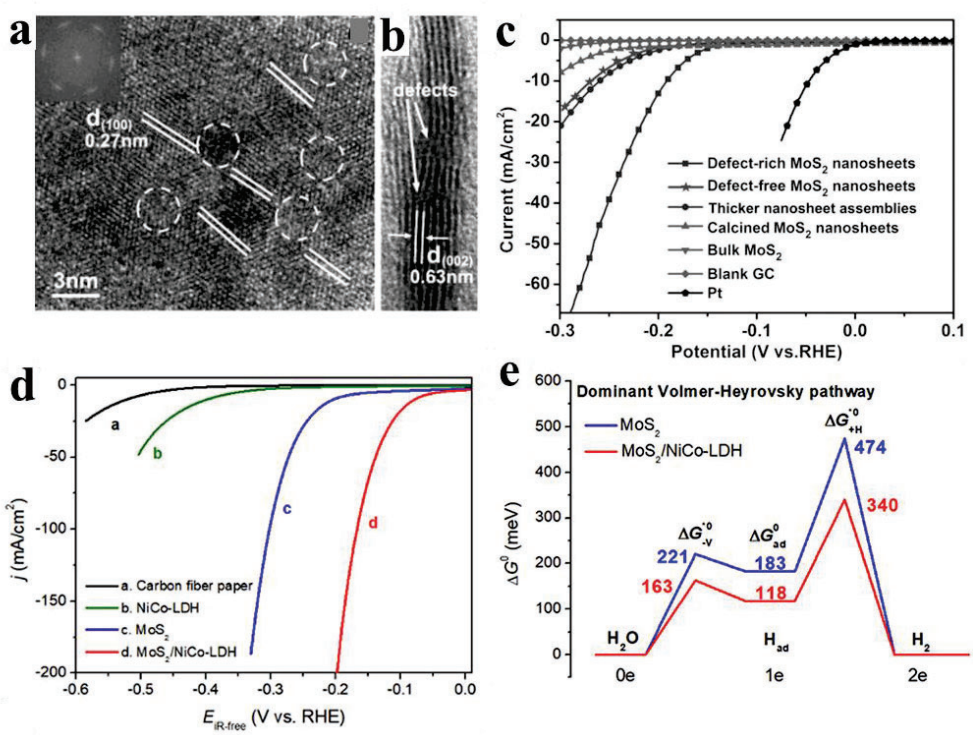

Figure 2.8. (a) HRTEM image and the corresponding FFT patterns. (b) Cross-sectional HRTEM image. (c) Polarization curves of various samples as shown. (d) Polarization curves of different samples as shown. (e) Free energy diagram of the dominant Volmer-Heyrovsky pathway for two samples as indicated. (a), (b), and (c) reproduced with the permission.[111] Copyright © 2013 WILEY‐VCH Verlag GmbH & Co. KGaA, Weinheim. (d) and (e) reproduced with the permission.[115] Copyright © 2017 Elsevier Inc.

Constructing hetero-interface via hybridizing with an additional phase (e.g., graphene and $Ni(OH)_2$) is another strategy to optimize the hydrogen adsorption energy on Mo edges, and further improving the catalytic activity of MoS_2. Under the guidance of the prediction, various MoS_2-based heterostructures are synthesized and normally delivered improved HER performance compared to pure MoS_2. The supported phases have a wide range of choice, including from 0D quantum dots to 3D foams.[112-116] For example, Feng's group presented the interface engineering of MoS_2/Ni_3S_2 as a bi-functional water splitting electrocatalysis.[116] Combining the experimental and theoretic results, it can be demonstrated that the engineered interfaces between MoS_2 and Ni_3S_2 is of great benefit to the chemisorption of hydrogen and oxygen intermediates, accordingly enhancing the overall water-splitting reaction performance. Yang's group also utilized the synergistic effects of heterostructure fabricated by MoS_2 hybridized with NiCo-LDH to improve the HER kinetics in base (**Figure 2.8d-e**).[115] In addition, phase engineering for TMDs

like the phase transition of 2H phase to 1T facilitates the activation of the basal plane, obviously alter band structures, and boost the charge transfer process, consequently enhancing the catalytic performance.

2.3.3. 2D electrocatalysts for ORR

2.3.3.1. Graphene-based ORR electrocatalysts

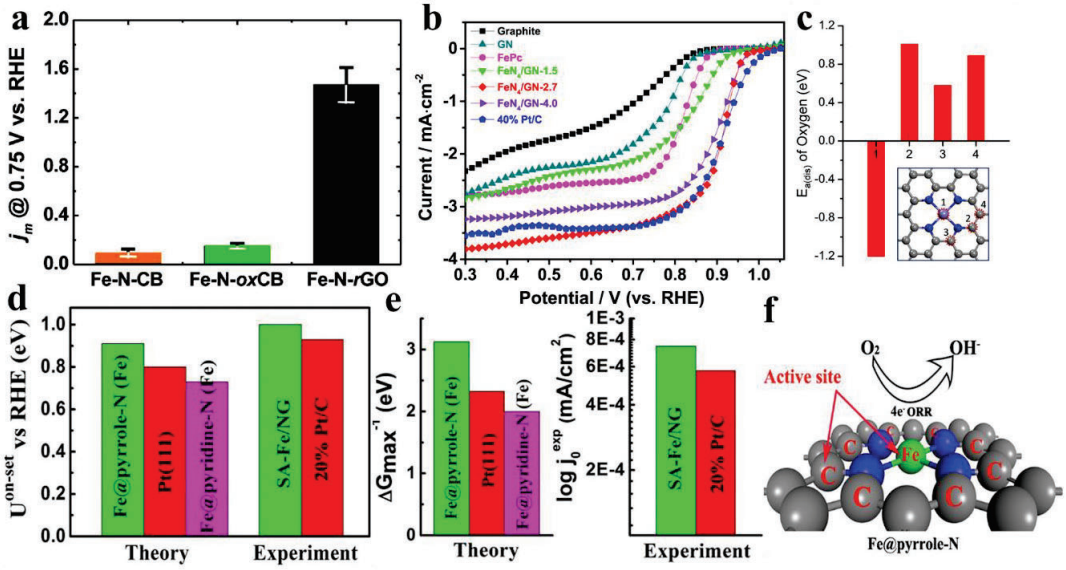

Figure 2.9. (a) ORR mass activity of three Fe−N−C catalysts at 0.75 V vs RHE. Reproduced with the permission.[122] Copyright © 2011 American Chemical Society. (b) ORR polarization curves of different graphene confining FeN_4 catalysts and other comparative samples. (c) Dissociative adsorption energy ($E_{a(dis)}$) of O_2 on various sites in FeN_4 model. (d) Comparison of onset potential with RHE (U_{onset}) for the theoretical calculation and experiment measurement in base. (e) Comparison of the theoretical free energy of potential-determining step at equilibrium potential (ΔG_{max}) and the exchange current density in experiment (j_0^{exp}) for different catalysts in base. (f) Computational models of Fe@pyrrolic N moieties for ORR. [124] (b) and (c) reproduced with the permission.[123] Copyright © 2016 Published by Elsevier Ltd.

Developing high-efficient and low-cost electrocatalysts is urgent demand for application of electrocatalytic technology. To a certain extent, the noble-metal-free strategy simulates the development of 2D electrocatalysts. Especially, the development of metal-N_x-confined graphene and the N-doped graphene ORR electrocatalysts was originated from the Pt-replacing strategy in fuel cells.[117-121] So far, the single-atom-confined graphene electrocatalysts exhibit a superior activity for the oxygen reduction process, surpassing 3D-carbon catalysts. For example, Yang's group reported Fe–N–C electrocatalyst based on functional graphene (Fe–N–rGO) synthesized by heating the mixture of Fe salt, g-C_3N_4, and

rGO.[122] The ORR performance of as-obtained Fe–N–rGO catalysts are better than that of carbon black-based FeN_x catalysts (**Figure 2.9a**). The enhanced activities of Fe–N–rGO catalysts might be attributed to the modified graphene with large surface area and unique electronic configuration, which could offer a platform to support the numerous FeN_x active sites. Bao's group also found that the single iron sites confined in graphene matrix exhibit a comparable ORR performance, as well as a higher stability and tolerance to SO_x, NO_x, and methanol over 40% commercial Pt/C (**Figure 2.9b**).[123] To reveal the origins of catalytic activity and reaction mechanism, DFT calculations were applied. The DFT results suggested that the high ORR performance can be due to the high dispersion and high-density coordination of unsaturated Fe sites, which can serve as the active sites and effectively activate O species (**Figure 2.9c**). Also, the high stability can be ascribed to the chemical confinement of 4N atoms by graphene matrix. Recently, Cao's group further unveiled that incorporating Fe atoms into the N-doped graphene matrix can activate the C atoms next to the pyrrolic N atoms to serve as the additional active sites, resulting in the increasing of active sites by orders of magnitude (**Figure 2.9d-f**).[124] Engineering Fe-pyrrolic-N_4 model has great potential in catalytic fields for energy storage and conversion.

Apart from Fe single atoms, some other transition-metal atoms, such as Cu, Mn, and Ru, can be confined by functional graphene matrix for high-performance ORR electrocatalysts.[125-127] For example, Sun's group reported that Cu single atoms uniformly anchored on graphene (Cu/G) matrix with a loading of 5.4 wt% as an ORR electrocatalysts. The Cu/G hybrid catalyst exhibits outstanding ORR activity, even surpassing the commercial Pt/C.[127] Tour's group reported single-dispersion Ru atoms embedded on N-doped graphene matrix (Ru-N/G) for high-ORR activity.[125] The isolated single Ru-N_4 species as the oxygen-reduction active sites have been computationally confirmed. Also, the Ru-oxo-N_4 structure should take responsibility for the enhanced ORR activity.

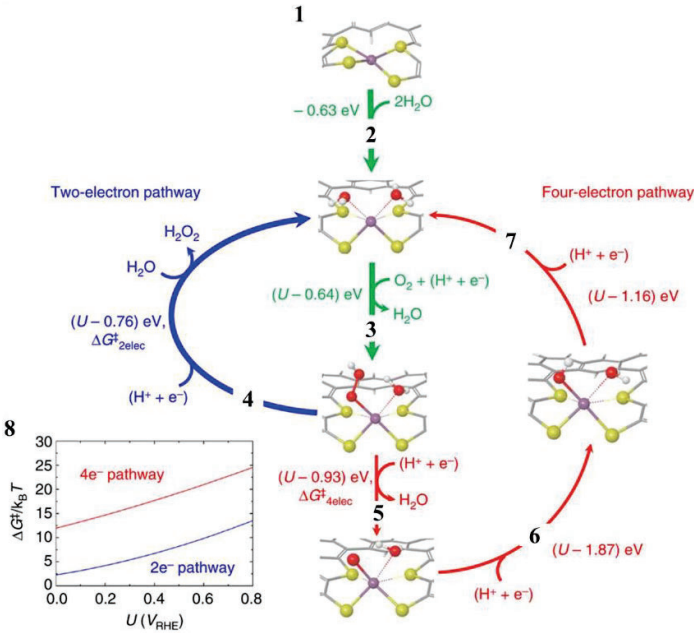

Figure 2.10. The ORR mechanism of the PtS_4 catalyst.[128]

In addition to the N as the ligands to confine the single atoms on the modified graphene matrix, S incorporated into the graphene can be also as the ligands to anchor the metal atoms. However, this would apply in different catalytic reaction. Such as, Choi and co-authors reported that PtS_4 moieties anchored on the graphene can selectively catalyze the two-electron H_2O_2, rather than the four-electron ORR process. As expounded by **Figure 2.10**, all elementary pathways are conducive to thermodynamic-dominated processes, which is not consistent with the experimental results.[128] Therefore, it can be inferred that the catalytic reaction on the PtS_4 species might be dynamic-dominated processes.

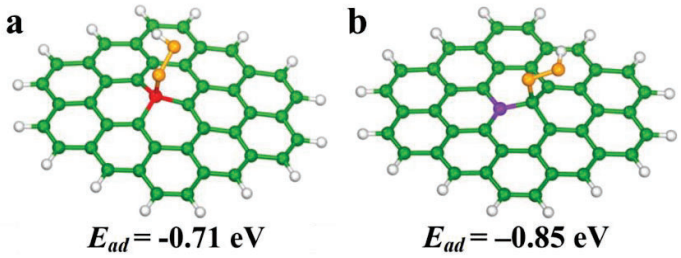

Figure 2.11. HO_2 adsorption model in (a) B-doped graphene, and (b) graphitic N-doped graphene. Reproduced with the permission.[129] Copyright © 2013 WILEY - VCH Verlag GmbH & Co. KGaA, Weinheim.

Except for the metal atoms confined in the graphene-based electrocatalysts, some non-metal elements such as B, N, and S doped or dual-doped into graphene matrix for ORR. Similar to the HER, due to the different size and electronegativity of the heteroatoms from C atoms, doping heteroatoms can modulate

the electronic structures of graphene. It is worth noting that B- and N-doped graphene electrocatalysts exhibit almost different catalytic mechanism. As demonstrated by Qiao's group, the adsorption sites for HO_2 on B-doped graphene are B atoms themselves (**Figure 2.11a**), whereas those on N-doped graphene are C atoms adjacent to graphitic N atoms that is far from the edges (**Figure 2.11b**).[129] The different adsorption sites might originate from the distinguished electronegativity. The N electronegativity is higher than that of C, resulting in the charge transfer from C atom to N atom in N-doped graphene. Accordingly, the adsorption and activation of O_2 were significantly improvedsuggestingthat N atom could activate the inactive graphene to accelerate the oxygen reduction process. In contrast, the electronegativity of B atoms in B-doped graphene is lower than that of C atoms, which would lead to the charge transfer from B atoms to C atoms. As a result, the B sites with positive charges can be served as the active sites. Besides, the dual-doped graphene electrocatalysts can show better catalytic activity as compared to single-doped graphene due to the synergistic effects between the different dopants, which can be also documented by combining theoretical analysis and experimental findings.[91, 129-131]

Apart from the heteroatom-doped graphene-based catalysts, some dopant-free graphene like defective graphene electrocatalysts also show remarkable ORR activity, and even are superior to those of dual-doped graphene.[132-136] The defective graphene can introduce additional active sites by constructing extra edges or structure defects to alter the electronic properties of graphene, and further enhancing the catalytic activities. Wang and co-authors discovered that there are more active sites on the edges of graphene than that of the basal plane due to the highly charged edge. Further, it can be inferred that there are also similar edge sites in various carbon matrixes, such as 0D-graphene quantum dots and 1D-graphene nanoribbons, which both are widely investigated as efficient ORR catalysts.[137-138]

2.3.3.2. Graphitic carbon nitride-based ORR electrocatalysts

Although bare GCN is nearly inert for electrocatalysis due to the wide band gap (2.7 eV), it possesses high-level pyridinic N, which can not only serve as the metal coordination sites, but also help to identify the active sites. Some investigations have indicated that the GCN-based ORR electrocatalysts delivered high catalytic performance mainly originated from the synergistic effects between GCN and the active metal sites or conductive carbonaceous materials (e.g., carbon black, CNT and graphene).[139-142] For example, Qiao's group prepared a g-C_3N_4@carbon ORR electrocatalyst by uniformly anchoring g-C_3N_4 on the carbon to improve the charge-transfer ability of g-C_3N_4.[139] In fact, the C_3N_4@CMK-3 electrocatalyst showed a better catalytic activity than the individual components and physical mixtures.

The enhanced ORR activity for C_3N_4@CMK-3 is ascribed to the incorporation of carbon support, which could effciently accumulates electrons on the surface of g-C_3N_4 to increases the charge transfer kinetics of ORR process. Moreover, the Qiao's group reported a g-C_3N_4/carbon catalyst with three-dimensional interconnected macropores via hard-template method.[143] This resultant samples exhibited a comparable ORR performance over the commercial Pt/C because of the strong carbon framework.

2.4. Engineering protocols for 2D electrocatalysts

As aforementioned in above parts, most pure 2D electrocatalysts are inactive because of the large reaction free energy, low amount of active sites and conductivity.[8, 39, 120] Thus, some efficient optimization strategies (including heteroatom doping, surface/interface building, defect constructing, and geometric controlling, etc.) are already proposed for 2D electrocatalysts to achieve higher catalytic activities. These optimization approaches aim to modulate the surface/interface properties and electronic structures correlated with hydrogen adsorption free energy and charge/mass transfer kinetics, which would affect catalytic kinetics. In this section, a variety of design strategies for 2D nanomaterial-based electrocatalysts are summarized.

2.4.1. Heteroatom doping

Heteroatom doping is considered as an efficient approach to modulating the electronic states, controlling the surface/interface properties, and altering the elementary compositions of 2D electrocatalysts. So far, heteroatom doping method for 2D nanomaterials is mainly applied in the cases of LDHs, graphene, transition-metal dichalcogenides (TMDs), and g-C_3N_4, etc. Both non-metal atoms and metal atoms have been extensively studied as the dopants. Doping graphene with one or more non-metal heteroatoms is the most efficient way for boosting electrocatalytic performance of graphene-based catalysts. Among the single-heteroatom-doped graphene nanomaterials, N-doped graphene-based catalysts are the pioneer of non-metal-atom doped 2D electrocatalysts. N atom is the most common and efficient dopant for carbonaceous materials. Since the size and electronegativity of N atoms are different from those of C atoms, the electronic states of carbonaceous catalysts could be modulated by N doping via the conjugation effects between nitrogen lone electronic pairs and carbon π-system.[144-145] Motivated by the findings, N, P, S, Br, and O heteroatoms have been provided as the single or dual dopants. These heteroatoms commonly substituted or disrupt the carbon atoms at the edge areas and basal planes to form the defect sites, which can work as the active sites, facilitating the eletrocatalytic processes. Notably,

various types and amount of dopants can induce the differences of active sites, which affects the catalytic performance.[129-131,146] In addition to doping the carbon matrix, doping other types of 2D matrix, such as O-doped MoS_2, alter the electronic structures of matrixes as well, and further affect the electrocatalytic activity.[147] On the other hand, metal-atom doping mainly investigated the effects of metal-based particle size on the catalytic performance. It has been demonstrated that the catalytic performance depended on size effects were generally exhibited in the order, single atoms > sub-nanocluster > nanoparticles. Especially, the single-atom catalysts supported on the 2D substrates can create more active sites for various catalytic activities. Other than carbon-based 2D electrocatalysts as discussed in the previous sections, metal doping can also change the electronic states of TMDs, including the creation of more additional active sites and the activation of inert basal planes. For example, doping Fe, Co, and Ni could also modulate the electronic states of TMDs, which facilitates the activation of in-plane S sites.[8,148-150] This promotion is because Co, Ni could lower the binding strength of edge S induced by a reduced occupation of antibonding states. Thus, it is not difficult to find that doping heteroatom is an effective and tailorable strategy to modulate 2D nanomaterials for unique electrocatalytic activities.

2.4.2. Defect engineering

Engineering defects (nano holes, vacancies, etc.) is an efficient way to the modulation of electronic structures and physicochemical properties of 2D nanomaterial-based electrocatalysts, which strongly affect the extrinsic and intrinsic activities.[152-153] Some reports claimed that the catalytic activity of MoS_2 originates from the edge Mo sites. Introducing S vacancies into the basal planes can not only modify the band gaps but also create additional exposed Mo edge sites.[154] Xie's group utilized a large-scale approach to introducing defects on the surface of MoS_2 to generate more active edges. [155] The HRTEM results confirm the formation of disordered atomic arrays on the basal planes, which can cause the crack of the basal planes, generating more additional edges. Ajayan's group constructed abundant defects within the monolayer of MoS_2 via hydrogen treatment and oxygen plasma exposure. [156] The formation of these defects significantly increases the total number of the exposed active edge sites, significantly enhancing HER kinetics. Moreover, the constructed defects can cause the lattice strains, which also modulate the band gaps of 2D materials. Li et al. introduced S vacancies and strains in the monolayer 2H-MoS_2 basal plane for improved HER activity. [157] The S vacancies with band states approaching the Fermi level can facilitate hydrogen adsorption. The ΔG_H can be dominated by strains induced by S vacancies, and thereby improving the HER kinetics. The synergistic effects of S vacancies and strains

lead to an optimal ΔG_H = 0 eV and attain significantly enhanced intrinsic HER activity. Thus, constructing defects for 2D nanomaterial-based electrocatalysts has been an important strategy for accelerating catalytic activity. However, controllable tuning of defects is necessary for the in-depth understanding of defects and the effects on reaction mechanisms. For example, Yao's group engineered defect-abundant graphene via removing the doped N.[158] They found that the promoted catalytic performance is strongly correlated with the defect contents induced by the removal of nitrogen, and the lower nitrogen content, the higher catalytic performance, further indicating that defect-engineering strategy is feasible to achieve high catalytic activity for graphene-based catalysts.

2.4.3. Interface engineering

Interface engineering is an essential strategy to constructing highly active catalysts with well-defined heterointerfaces. Engineering hetero-interface employing different components can modulate the surface/interface properties and electronic structures of 2D nanomaterial-based electrocatalysts, inducing novel physicochemical properties and synergistic effects, which are beneficial to the enhancement of electrocatalytic activities.[159-160] Generally, heterointerface could be classfied into the synergistic interaction and heterostructure engineering, which usually involves each other. The different components consisting of heterostructures is usually combined by chemical bonds at the interface, while the two phases existing in the synergistic interaction with coupled electron transit are physically connected. In addition, interface constructing can induce unique physicochemical properties, which also facilitates the electrocatalytic performance. The design principles of heterointerface for 2D electrocatalysts are commonly following several factors. Firstly, the components should possess similar crystal structure for favourably forming the heterostructures. Secondly, at least one component has the target catalytic activity. Thirdly, the heterostructured catalysts should be conductive so that meet the demand of electron transfer to the reactive intermediates. Finally, the two components can fill the gap of electrocatalytic properties each other and synergistically improve the catalytic performance.

2.4.4. Geometric engineering

The geometric configurations of 2D electrocatalysts significantly affect the catalytic performance due to the following reasons .[133] (1) decreasing the lateral size of 2D electrocatalysts could expose more active sites; (2) altering the thickness of 2D nanomaterials could modulate the electronic properties; (3) reducing the thickness of 2D nanomaterials to the atomic scale is beneficial to generating more in-plane defects as additional active sites, and optimizing the electrical conductivity. Jaramillo's group controlled the surface

morphology of MoS_2 at the atomic scale to investigate its effect on the HER performance.[105] They discovered that reducing the thickness to sub-nanometres can induce the lattice distortions, which can creates many vacancies for enhanced catalytic activities. Another characteristic of tuning thickness can possibly expose the maximal areas for the favourable ECSA. Besides, Zheng's group developed the freestanding Pd NSs for plasmonic property and electrocatalytic activity for the oxidation of formic acid. The Pd NSs exhibited a higher current density due to the larger ECSA as compared to commercial Pd black. According to this concept, a series of synthesis strategies for various metal or metal-based alloys NSs have been reported, such as Rh, Pd-Cu, and Pt-Cu.[159-161]

2.4.5 Phase engineering

Phase engineering for TMDs (from the semiconducting 2H phase to the metastable metallic 1T phase) can alter the bandgaps and enhance electronic conductivity. Generally, the strategies for phase engineering include alkali metal intercalation, hydrothermal method , and heterostructure construction, etc.[162-163] Chhowalla's group utilized the solvent free intercalation method to obtain the exfoliated MoS_2 nanosheets with a large amount of metallic 1T phases as the highly active HER electrocatalysts.[164] The MoS_2 nanosheets of 1T phase deliver superior HER kinetics after the removal of surface excess negative charges. Moreover, the HER performance of 2H phase can be significantly promoted by adding the conductive SWNTs, indicating the poor conductivity of 2H phase is unfavourable to the catalytic activity. The results further demonstrate that 1T phase shows a better electron-transfer property than 2H phase, which is an important factor for the enhancement of the HER performance.[165] Therefore, the phase transition of TMDs from semiconductor 2H phase to metallic 1T phase via chemical exfoliation is an efficient way for the promotion of HER catalytic activity.

2.5. References

[1] W. T. Grubb, *Nature* 1963, *198*, 883-884.

[2] A. Frumkin, N. Polianovskaya, I. Bagotskaya, N. Grigoryev, *Journal of Electroanalytical Chemistry and Interfacial Electrochemistry* 1971, *33*, 319-328.

[3] F. P. Bowden, E. K. Rideal, T. M. Lowry, *Proceedings of the Royal Society of London. Series A, Containing Papers of a Mathematical and Physical Character* 1928, *120*, 59-79.

[4] J. A. V. Butler, J. P. Kendall, *Proceedings of the Royal Society of London. Series A - Mathematical and Physical Sciences* 1936, *157*, 423-433.

[5] R. Parsons, *Transactions of the Faraday Society* 1958, *54*, 1053-1063.

[6] H. Gerischer, *Zeitschrift fur Physikalische Chemie* 1956, *8*, 137-153.

[7] I. C. Man, H.-Y. Su, F. Calle-Vallejo, H. A. Hansen, J. I. Martínez, N. G. Inoglu, J. Kitchin, T. F. Jaramillo, J. K. Nørskov, J. Rossmeisl, *ChemCatChem* 2011, *3*, 1159-1165.

[8] T. F. Jaramillo, K. P. Jørgensen, J. Bonde, J. H. Nielsen, S. Horch, I. Chorkendorff, *Science* 2007, *317*, 100-102.

[9] J. K. Nørskov, J. Rossmeisl, A. Logadottir, L. Lindqvist, J. R. Kitchin, T. Bligaard, H. Jónsson, *The Journal of Physical Chemistry B* 2004, *108*, 17886-17892.

[10] A. Verdaguer-Casadevall, D. Deiana, M. Karamad, S. Siahrostami, P. Malacrida, T. W. Hansen, J. Rossmeisl, I. Chorkendorff, I. E. L. Stephens, *Nano Lett.* 2014, *14*, 1603-1608.

[11] K. P. Kuhl, T. Hatsukade, E. R. Cave, D. N. Abram, J. Kibsgaard, T. F. Jaramillo, *J. Am. Chem. Soc.* 2014, *136*, 14107-14113.

[12] J. H. Montoya, C. Tsai, A. Vojvodic, J. K. Nørskov, *ChemSusChem* 2015, *8*, 2180-2186.

[13] V. Vij, S. Sultan, A. M. Harzandi, A. Meena, J. N. Tiwari, W.-G. Lee, T. Yoon, K. S. Kim, *ACS Catal.* 2017, *7*, 7196-7225.

[14] M. Gong, H. Dai, *Nano Res.* 2015, *8*, 23-39.

[15] H. Dau, C. Limb erg, T. Reier, M. Risch, S. Roggan, P. Strasser, *ChemCatChem* 2010, *2*, 724-761.

[16] C. Tang, H.-F. Wang, X.-L. Zhu, B.-Q. Li, Q. Zhang, *Part. .Part. Sys. Charact.* 2016, *33*, 473-486.

[17] C. C. L. McCrory, S. Jung, J. C. Peters, T. F. Jaramillo, *J. Am. Chem. Soc.* 2013, *135*, 16977-16987.

[18] J. K. Nørskov, T. Bligaard, A. Logadottir, J. R. Kitchin, J. G. Chen, S. Pandelov, U. Stimming, *J.. Electrochem. Soc.* 2005, *152*, J23-J26.

[19] J. Greeley, M. Mavrikakis, *Nat. Mater.* 2004, *3*, 810-815.

[20] J. Greeley, T. F. Jaramillo, J. Bonde, I. Chorkendorff, J. K. Nørskov, *Nat. Mater.* 2006, *5*, 909.

[21] E. Skúlason, V. Tripkovic, M. E. Björketun, S. Gudmundsdóttir, G. Karlberg, J. Rossmeisl, T. Bligaard, H. Jónsson, J. K. Nørskov, *J. Phys. Chem. C* 2010, *114*, 18182-18197.

[22] Y. Zheng, Y. Jiao, M. Jaroniec, S. Z. Qiao, *Angew. Chem. Int. Edit.* 2015, *54*, 52-65.

[23] Z. W. Seh, J. Kibsgaard, C. F. Dickens, I. Chorkendorff, J. K. Nørskov, T. F. Jaramillo, *Science* 2017, *355*, eaad4998.

[24] J. Rossmeisl, E. Skúlason, M. E. Björketun, V. Tripkovic, J. K. Nørskov, *Chemical Physics Letters* 2008, *466*, 68-71.

[25] S. Siahrostami, A. Verdaguer-Casadevall, M. Karamad, D. Deiana, P. Malacrida, B. Wickman, M. Escudero-Escribano, E. A. Paoli, R. Frydendal, T. W. Hansen, I. Chorkendorff, I. E. L. Stephens, J. Rossmeisl, *Nat. Mater.* 2013, *12*, 1137.

[26] H. J. Yan, B. Xu, S. Q. Shi, C. Y. Ouyang, *Journal of Applied Physics* 2012, *112*, 104316.

[27] G.-L. Chai, Z. Hou, T. Ikeda, K. Terakura, *J. Phys. Chem. C* 2017, *121*, 14524-14533.

[28] J. Park, Y. Nabae, T. Hayakawa, M.-a. Kakimoto, *ACS Catal.* 2014, *4*, 3749-3754.

[29] C. M. Pedersen, M. Escudero-Escribano, A. Velázquez-Palenzuela, L. H. Christensen, I. Chorkendorff, I. E. L. Stephens, *Electrochim. Acta* 2015, *179*, 647-657.

[30] Y. Jiao, Y. Zheng, M. Jaroniec, S. Z. Qiao, *J. Am. Chem. Soc.* 2014, *136*, 4394-4403.

[31] V. Viswanathan, H. A. Hansen, J. Rossmeisl, J. K. Nørskov, *ACS Catal.* 2012, *2*, 1654-1660.

[32] D. Brownson, C. Banks, *Physical chemistry chemical physics : PCCP* 2012, *14*, 8264-8281.

[33] H. Zhang, *ACS Nano* 2015, *9*, 9451-9469.

[34] C. Tan, Z. Lai, H. Zhang, *Adv. Mater.* 2017, 10.1002/adma.201701392, 1701392-n/a.

[35] C. Tan, X. Cao, X.-J. Wu, Q. He, J. Yang, X. Zhang, J. Chen, W. Zhao, S. Han, G.-H. Nam, M. Sindoro, H. Zhang, *Chem. Rev.* 2017, *117*, 6225-6331.

[36] Y. Sun, S. Gao, F. Lei, Y. Xie, *Chem. Soc.Rev.* 2015, *44*, 623-636.

[37] H. Tao, Y. Gao, N. Talreja, F. Guo, J. Texter, C. Yan, Z. Sun, *J. Mater. Chem. A* 2017, *5*, 7257-7284.

[38] R. Frisenda, E. Navarro-Moratalla, P. Gant, D. Perez De Lara, P. Jarillo-Herrero, R. V. Gorbachev, A. Castellanos-Gomez, *Chem. Soc.Rev.* 2017, 10.1039/C7CS00556C.

[39] Y. Zheng, Y. Jiao, Y. Zhu, L. H. Li, Y. Han, Y. Chen, A. Du, M. Jaroniec, S. Z. Qiao, *Nat. Commun.* 2014, *5*, 3783.

[40] H. Li, C. Tsai, A. L. Koh, L. Cai, A. W. Contryman, A. H. Fragapane, J. Zhao, H. S. Han, H. C. Manoharan, F. Abild-Pedersen, J. K. Nørskov, X. Zheng, *Nat. Mater.* 2015, *15*, 48-54.

[41] H. Jin, C. Guo, X. Liu, J. Liu, A. Vasileff, Y. Jiao, Y. Zheng, S.-Z. Qiao, *Chem. Rev.* 2018, *118*.

[42] M. Tahir, L. Pan, F. Idrees, X. Zhang, L. Wang, J.-J. Zou, Z. L. Wang, *Nano Energy* 2017, *37*, 136-157.

[43] H. Kuhlenbeck, S. Shaikhutdinov, H.-J. Freund, *Chem. Rev.* 2013, *113*, 3986-4034.

[44] E. Arciga-Duran, Y. Meas, J. J. Perez-Bueno, J. C. Ballesteros, G. Trejo, *Electrochim. Acta* 2018, *268*, 49-58.

[45] A. Bergmann, E. Martinez-Moreno, D. Teschner, P. Chernev, M. Gliech, J. F. de Araújo, T. Reier, H. Dau, P. Strasser, *Nat. Commun.* 2015, *6*, 8625.

[46] D. K. Bediako, B. Lassalle-Kaiser, Y. Surendranath, J. Yano, V. K. Yachandra, D. G. Nocera, *J. Am. Chem. Soc.* 2012, *134*, 6801-6809.

[47] X. Zheng, B. Zhang, P. De Luna, Y. Liang, R. Comin, O. Voznyy, L. Han, F. P. García de Arquer, M. Liu, C. T. Dinh, T. Regier, J. J. Dynes, S. He, H. L. Xin, H. Peng, D. Prendergast, X. Du, E. H. Sargent, *Nature Chemistry* 2017, *10*, 149.

[48] M. Tahir, L. Pan, R. Zhang, Y.-C. Wang, G. Shen, I. Aslam, M. A. Qadeer, N. Mahmood, W. Xu, L. Wang, X. Zhang, J.-J. Zou, *ACS Energy Letters* 2017, *2*, 2177-2182.

[49] Y. Zhao, X. Jia, G. Chen, L. Shang, G. I. N. Waterhouse, L.-Z. Wu, C.-H. Tung, D. O'Hare, T. Zhang, *Journal of the American Chemical Society* 2016, *138*, 6517-6524.

[50] K. Fan, H. Chen, Y. Ji, H. Huang, P. M. Claesson, Q. Daniel, B. Philippe, H. Rensmo, F. Li, Y. Luo, L. Sun, *Nat. Commun.* 2016, *7*.

[51] S. Anantharaj, K. Karthick, M. Venkatesh, T. V. S. V. Simha, A. S. Salunke, L. Ma, H. Liang, S. Kundu, *Nano Energy* 2017, *39*, 30-43.

[52] C. Andronescu, S. Barwe, E. Ventosa, J. Masa, E. Vasile, B. Konkena, S. Möller, W. Schuhmann, *Angew. Chem. Int. Edit.* 2017, *56*, 11258-11262.

[53] D. Su, M. Ford, G. Wang, *Sci Rep* 2012, *2*, 924.

[54] G. Wu, W. Chen, X. Zheng, D. He, Y. Luo, X. Wang, J. Yang, Y. Wu, W. Yan, Z. Zhuang, X. Hong, Y. Li, *Nano Energy*, https://doi.org/10.1016/j.nanoen.2017.05.044.

[55] Y. P. Zhu, C. Guo, Y. Zheng, S.-Z. Qiao, *Acc. Chem. Res.* 2017, *50*, 915-923.

[56] B. Zhang, X. Zheng, O. Voznyy, R. Comin, M. Bajdich, M. García-Melchor, L. Han, J. Xu, M. Liu, L. Zheng, F. P. García de Arquer, C. T. Dinh, F. Fan, M. Yuan, E. Yassitepe, N. Chen, T. Regier, P. Liu, Y. Li, P. De Luna, A. Janmohamed, H. L. Xin, H. Yang, A. Vojvodic, E. H. Sargent, *Science* 2016, *352*, 333-337.

[57] J. Hou, Y. Sun, Y. Wu, S. Cao, L. Sun, *Adv. Funct. Mater.* 2018, *28*, 1704447-1704459.

[58] K. Fominykh, P. Chernev, I. Zaharieva, J. Sicklinger, G. Stefanic, M. Döblinger, A. Müller, A. Pokharel, S. Böcklein, C. Scheu, T. Bein, D. Fattakhova-Rohlfing, *ACS Nano* 2015, *9*, 5180-5188.

[59] B. Zhang, C. Xiao, S. Xie, J. Liang, X. Chen, Y. Tang, *Chem. Mater.* 2016, *28*, 6934-6941.

[60] B. Li, S. Chen, J. Tian, M. Gong, H. Xu, L. Song, *Nano Res.* 2017, *10*, 3629-3637.

[61] T. Reier, Z. Pawolek, S. Cherevko, M. Bruns, T. Jones, D. Teschner, S. Selve, A. Bergmann, H. N. Nong, R. Schlögl, K. J. J. Mayrhofer, P. Strasser, *J. Am. Chem. Soc.* 2015, *137*, 13031-13040.

[62] J. W. D. Ng, M. García-Melchor, M. Bajdich, P. Chakthranont, C. Kirk, A. Vojvodic, T. F. Jaramillo, *Nat. Energy* 2016, *1*, 16053.

[63] G. Fan, F. Li, D. G. Evans, X. Duan, *Chem. Soc.Rev.* 2014, *43*, 7040-7066.

[64] Q. Wang, D. O'Hare, *Chem. Rev.* 2012, *112*, 4124-4155.

[65] G. Wei, L.-R. Zhang, Z. Liu, *Phys. Chem. Chem. Phys.* 2018, 10.1039/C8CP05079A.

[66] Y. Gong, H. Yuan, C.-L. Wu, P. Tang, S.-Z. Yang, A. Yang, G. Li, B. Liu, J. van de Groep, M. L. Brongersma, M. F. Chisholm, S.-C. Zhang, W. Zhou, Y. Cui, *Nat. Nanotechnol.* 2018, *13*, 294-299.

[67] M. Gong, Y. Li, H. Wang, Y. Liang, J. Z. Wu, J. Zhou, J. Wang, T. Regier, F. Wei, H. Dai, *J. Am. Chem. Soc.* 2013, *135*, 8452-8455.

[68] H. Liu, J. Zhou, C. Wu, C. Wang, Y. Zhang, D. Liu, Y. Lin, H. Jiang, L. Song, *ACS Sustain. Chem. Eng.* 2018, *6*, 2911-2915.

[69] S. Yin, W. Tu, Y. Sheng, Y. Du, M. Kraft, A. Borgna, R. Xu, *Adv. Mater.* 2018, *30*.

[70] C. Tang, H.-S. Wang, H.-F. Wang, Q. Zhang, G.-L. Tian, J.-Q. Nie, F. Wei, *Adv. Mater.* 2015, *27*, 4516-4522.

[71] W. Ma, R. Ma, C. Wang, J. Liang, X. Liu, K. Zhou, T. Sasaki, *ACS Nano* 2015, *9*, 1977-1984.

[72] T. Kwon, H. Hwang, Y. J. Sa, J. Park, H. Baik, S. H. Joo, K. Lee, *Adv. Funct. Mater.* 2017, *27*, 1604688.

[73] G. Prieto, H. Tüysüz, N. Duyckaerts, J. Knossalla, G.-H. Wang, F. Schüth, *Chem. Rev.* 2016, *116*, 14056-14119.

[74] J. Nai, B. Y. Guan, L. Yu, X. W. Lou, *Sci. Adv.* 2017, *3*.

[75] L. Yu, J. F. Yang, B. Y. Guan, Y. Lu, X. W. D. Lou, *Angew. Chem. Int. Edit.* 2018, *57*, 172-176.

[76] H. Liang, F. Meng, M. Cabán-Acevedo, L. Li, A. Forticaux, L. Xiu, Z. Wang, S. Jin, *Nano Lett.* 2015, *15*, 1421-1427.

[77] J. Shi, N. Du, W. Zheng, X. Li, Y. Dai, G. He, *Chem. Eng. J.* 2017, *327*, 9-17.

[78] X. Li, J. Zhou, X. Li, M. Xin, T. Cai, W. Xing, Y. Chai, Q. Xue, Z. Yan, *Electrochim. Acta* 2017, *252*, 275-285.

[79] A. Sumboja, J. Chen, Y. Zong, P. S. Lee, Z. Liu, *Nanoscale* 2017, *9*, 774-780.

[80] H. Liu, Y. Wang, X. Lu, Y. Hu, G. Zhu, R. Chen, L. Ma, H. Zhu, Z. Tie, J. Liu, Z. Jin, *Nano Energy* 2017, *35*, 350-357.

[81] Z. Lu, L. Qian, Y. Tian, Y. Li, X. Sun, X. Duan, *Chem. Commun.* 2016, *52*, 908-911.

[82] S. B. Khan, S. A. Khan, A. M. Asiri, *Appl. Surf. Sci.* 2016, *370*, 445-451.

[83] T. Wang, W. Xu, H. Wang, *Electrochim. Acta* 2017, *257*, 118-127.

[84] R. Li, Z. Wei, X. Gou, *ACS Catalysis* 2015, *5*, 4133-4142.

[85] K. S. Lakhi, D. H. Park, K. Al-Bahily, W. Cha, B. Viswanathan, J. H. Choy, A. Vinu, *Chem. Soc. Rev.* 2017, *46*, 72-101.

[86] T. Y. Ma, S. Dai, M. Jaroniec, S. Z. Qiao, *Angew. Chem. Int. Ed.* 2014, *53*, 7281-7285.

[87] J. Duan, S. Chen, M. Jaroniec, S. Z. Qiao, *ACS Nano* 2015, *9*, 931-940.

[88] J. Tian, Q. Liu, A. M. Asiri, K. A. Alamry, X. Sun, *ChemSusChem* 2014, *7*, 2125-2130.

[89] Y. Zheng, Y. Jiao, L. H. Li, T. Xing, Y. Chen, M. Jaroniec, S. Z. Qiao, *ACS Nano* 2014, *8*, 5290-5296.

[90] L. Zhang, Z. Xia, *The Journal of Physical Chemistry C* 2011, *115*, 11170-11176.

[91] J. Liang, Y. Jiao, M. Jaroniec, S. Z. Qiao, *Angew. Chem. Int. Ed.* 2012, *51*, 11496-11500.

[92] Y. Jiao, Y. Zheng, K. Davey, S.-Z. Qiao, *Nature Energy* 2016, *1*, 16130.

[93] N. Cheng, S. Stambula, D. Wang, M. N. Banis, J. Liu, A. Riese, B. Xiao, R. Li, T.-K. Sham, L.-M. Liu, G. A. Botton, X. Sun, *Nat. Commun.* 2016, *7*, 13638.

[94] H.-J. Qiu, Y. Ito, W. Cong, Y. Tan, P. Liu, A. Hirata, T. Fujita, Z. Tang, M. Chen, *Angew. Chem. Int. Edit.* 2015, *54*, 14031-14035.

[95] H. Fei, J. Dong, M. J. Arellano-Jiménez, G. Ye, N. Dong Kim, E. L. G. Samuel, Z. Peng, Z. Zhu, F. Qin, J. Bao, M. J. Yacaman, P. M. Ajayan, D. Chen, J. M. Tour, *Nature Communications* 2015, *6*, 8668.

[96] K. Tang, X. Wang, Q. Li, C. Yan, *Adv. Mater.* 2018, *30*, 1704779-1704786.

[97] K. K. Ghuman, S. Yadav, C. V. Singh, *J. Phys. Chem. C* 2015, *119*, 6518-6529.

[98] C. Tsai, K. Chan, F. Abild-Pedersen, J. K. Nørskov, *Phys. Chem. Chem. Phys.* 2014, *16*, 13156-13164.

[99] Y. Shi, Y. Zhou, D. Yang, W. Xu, C. Wang, F. Wang, J. Xu, X. Xia, H. Chen, *J. Am. Chem. Soc.* 2017, *139*, 15479–15485.

[100] N. Xue, P. Diao, *J. Phys. Chem. C* 2017, *121*, 26686–26697.

[101] H. Shu, D. Zhou, F. Li, D. Cao, X. Chen, *ACS Appl. Mater. Inter.* 2017, *9*, 42688–42698.

[102] O. Lehtinen, H.-P. Komsa, A. Pulkin, M. B. Whitwick, M.-W. Chen, T. Lehnert, M. J. Mohn, O. V. Yazyev, A. Kis, U. Kaiser, A. V. Krasheninnikov, *ACS Nano* 2015, *9*, 3274-3283.

[103] Y. Yin, Y. Zhang, T. Gao, T. Yao, X. Zhang, J. Han, X. Wang, Z. Zhang, P. Xu, P. Zhang, X. Cao, B. Song, S. Jin, *Adv. Mater.* 2017, *29*, 1700311-1700319.

[104] Z. Chen, D. Cummins, B. N. Reinecke, E. Clark, M. K. Sunkara, T. F. Jaramillo, *Nano Lett.* 2011, *11*, 4168-4175.

[105] J. Kibsgaard, Z. Chen, B. N. Reinecke, T. F. Jaramillo, *Nat. Mater.* 2012, *11*, 963.

[106] H. Vrubel, D. Merki, X. Hu, *Energy Environ. Sci.* 2012, *5*, 6136-6144.

[107] H. Wang, Z. Lu, D. Kong, J. Sun, T. M. Hymel, Y. Cui, *ACS Nano* 2014, *8*, 4940-4947.

[108] X. Zheng, J. Xu, K. Yan, H. Wang, Z. Wang, S. Yang, *Chem. Mater.* 2014, *26*, 2344-2353.

[109] J. Zhang, T. Wang, P. Liu, S. Liu, R. Dong, X. Zhuang, M. Chen, X. Feng, *Energy Environ. Sci.* 2016, *9*, 2789-2793.

[110] X.-Y. Yu, Y. Feng, Y. Jeon, B. Guan, X. W. Lou, U. Paik, *Adv. Mater.* 2016, *28*, 9006-9011.

[111] J. Xie, H. Zhang, S. Li, R. Wang, X. Sun, M. Zhou, J. Zhou, X. W. Lou, Y. Xie, , 5807-5813.

[112] S. Xu, D. Li, P. Wu, *Adv. Funct. Mater.* 2015, *25*, 1127-1136.

[113] J. Guo, H. Zhu, Y. Sun, L. Tang, X. Zhang, *Electrochim. Acta* 2016, *211*, 603-610.

[114] L. Yang, W. Zhou, J. Lu, D. Hou, Y. Ke, G. Li, Z. Tang, X. Kang, S. Chen, *Nano Energy* 2016, *22*, 490-498.

[115] J. Hu, C. Zhang, L. Jiang, H. Lin, Y. An, D. Zhou, M. K. H. Leung, S. Yang, *Joule* 2017, *1*, 383-393.

[116] J. Zhang, T. Wang, D. Pohl, B. Rellinghaus, R. Dong, S. Liu, X. Zhuang, X. Feng, *Angew. Chem. Int. Edit.* 2016, *55*, 6702-6707.

[117] G. Wu, K. L. More, C. M. Johnston, P. Zelenay, *Science* 2011, *332*, 443-447.

[118] M. Lefèvre, E. Proietti, F. Jaouen, J.-P. Dodelet, *Science* 2009, *324*, 71-74.

[119] R. Bashyam, P. Zelenay, in *Materials for Sustainable Energy*, 10.1142/9789814317665_0034, pp. 247-250.

[120] L. Qu, Y. Liu, J.-B. Baek, L. Dai, *ACS Nano* 2010, *4*, 1321-1326.

[121] K. Gong, F. Du, Z. Xia, M. Durstock, L. Dai, *Science* 2009, *323*, 760-764.

[122] H. R. Byon, J. Suntivich, Y. Shao-Horn, *Chem. Mater.* 2011, *23*, 3421-3428.

[123] X. Chen, L. Yu, S. Wang, D. Deng, X. Bao, *Nano Energy* 2017, *32*, 353-358.

[124] L. Yang, D. Cheng, H. Xu, X. Zeng, X. Wan, J. Shui, Z. Xiang, D. Cao, *Proceedings of the National Academy of Sciences* 2018, *115*, 6626-6631.

[125] C. Zhang, J. Sha, H. Fei, M. Liu, S. Yazdi, J. Zhang, Q. Zhong, X. Zou, N. Zhao, H. Yu, Z. Jiang, E. Ringe, B. I. Yakobson, J. Dong, D. Chen, J. M. Tour, *ACS Nano* 2017, *11*, 6930-6941.

[126] H. Wu, H. Li, X. Zhao, Q. Liu, J. Wang, J. Xiao, S. Xie, R. Si, F. Yang, S. Miao, X. Guo, G. Wang, X. Bao, *Energy Environ. Sci.* 2016, *9*, 3736-3745.

[127] G. Han, Y. Zheng, X. Zhang, Z. Wang, Y. Gong, C. Du, M. N. Banis, Y.-M. Yiu, T.-K. Sham, L. Gu, Y. Sun, Y. Wang, J. Wang, Y. Gao, G. Yin, X. Sun, *Nano Energy* 2019, *66*, 104088.

[128] C. H. Choi, M. Kim, H. C. Kwon, S. J. Cho, S. Yun, H.-T. Kim, K. J. J. Mayrhofer, H. Kim, M. Choi, *Nat. Commun.* 2016, *7*, 10922.

[129] Y. Zheng, Y. Jiao, L. Ge, M. Jaroniec, S. Z. Qiao, *Angew. Chem. Int. Edit.* 2013, *52*, 3110-3116.

[130] K. Qu, Y. Zheng, X. Zhang, K. Davey, S. Dai, S. Z. Qiao, *ACS Nano* 2017, *11*, 7293-7300.

[131] X. Wang, J. Wang, D. Wang, S. Dou, Z. Ma, J. Wu, L. Tao, A. Shen, C. Ouyang, Q. Liu, S. Wang, *Chem. Commun.* 2014, *50*, 4839-4842.

[132] J. Zhang, Z. Zhao, Z. Xia, L. Dai, *Nat Nanotechnol* 2015, *10*, 444-452.

[133] L. Tao, Q. Wang, S. Dou, Z. Ma, J. Huo, S. Wang, L. Dai, *Chem. Commun.* 2016, *52*, 2764-2767.

[134] X. Wang, X. Li, C. Ouyang, Z. Li, S. Dou, Z. Ma, L. Tao, J. Huo, S. Wang, *J. Mater. Chem. A* 2016, *4*, 9370-9374.

[135] Y. Jiang, L. Yang, T. Sun, J. Zhao, Z. Lyu, O. Zhuo, X. Wang, Q. Wu, J. Ma, Z. Hu, *ACS Catal.* 2015, *5*, 6707-6712.

[136] C. Tang, H.-F. Wang, X. Chen, B.-Q. Li, T.-Z. Hou, B. Zhang, Q. Zhang, M.-M. Titirici, F. Wei, *Adv. Mater.* 2016, *28*, 6845-6851.

[137] X. Tong, Q. Wei, X. Zhan, G. Zhang, S. Sun, *Catalysts* 2017, *7*, 1.

[138] Z. Zhang, J. Zhang, N. Chen, L. Qu, *Energy Environ. Sci.* 2012, *5*, 8869-8890.

[139] Y. Zheng, Y. Jiao, J. Chen, J. Liu, J. Liang, A. Du, W. Zhang, Z. Zhu, S. C. Smith, M. Jaroniec, G. Q. Lu, S. Z. Qiao, *J. Am. Chem. Soc.* 2011, *133*, 20116-20119.

[140] S. M. Lyth, Y. Nabae, S. Moriya, S. Kuroki, M.-a. Kakimoto, J.-i. Ozaki, S. Miyata, *J. Phys. Chem. C* 2009, *113*, 20148-20151.

[141] Y. Sun, C. Li, Y. Xu, H. Bai, Z. Yao, G. Shi, *Chem. Commun.* 2010, *46*, 4740-4742.

[142] S. Yang, X. Feng, X. Wang, K. Müllen, *Angew. Chem. Int. Edit.* 2011, *50*, 5339-5343.

[143] J. Liang, Y. Zheng, J. Chen, J. Liu, D. Hulicova-Jurcakova, M. Jaroniec, S. Z. Qiao, *Angew. Chem. Int. Edit.* 2012, *51*, 3892-3896.

[144] D. Deng, X. Pan, L. Yu, Y. Cui, Y. Jiang, J. Qi, W.-X. Li, Q. Fu, X. Ma, Q. Xue, G. Sun, X. Bao, Chem. Mater. 2011, 23, 1188-1193.

[145] Y. Li, Z. Zhou, P. Shen, Z. Chen, *ACS Nano* 2009, *3*, 1952-1958.

[146] Y. Jiao, Y. Zheng, M. Jaroniec, S. Z. Qiao, *J. Am. Chem. Soc.* 2014, *136*, 4394-4403.

[147] D. Deng, L. Yu, X. Pan, S. Wang, X. Chen, P. Hu, L. Sun, X. Bao, *Chem. Commun.* 2011, *47*, 10016-10018.

[148] J. Xie, J. Zhang, S. Li, F. Grote, X. Zhang, H. Zhang, R. Wang, Y. Lei, B. Pan, Y. Xie, *J. Am. Chem. Soc.* 2014, *136*, 1680-1680.

[149] Lauritsen, J. V., Helveg, S., Lægsgaard, E., Stensgaard, I., Clausen, B. S., Topsøe, H., Besenbacher, F. J. Catal. 2001, 197, 1-5.

[150] Byskov, L. S. Nørskov, J. K. Clausen, B. S. Topsøe, H. J. Catal. 1999, 187, 109-122.

[151] Bonde, J. Moses, P. G., Jaramillo, T. F. Norskov, J. K., Chorkendorff, I., 2009, 140, 219-231.

[152] Ç. Ö. Girit, J. C. Meyer, R. Erni, M. D. Rossell, C. Kisielowski, L. Yang, C.-H. Park, M. F. Crommie, M. L. Cohen, S. G. Louie, A. Zettl, *Science,* 2009, *323*, 1705-1708.

[153] Chen, Y., Huang, S., Ji, X., Adepalli, K., Yin, K., Ling, X., Wang, X., Xue, J., Dresselhaus, M., Kong, J., Yildiz, B.: Tuning Electronic Structure of Single Layer MoS2 through Defect and Interface Engineering. ACS Nano. 12. 2569-2579. (2018)

[154] Zhang, J., Wang, Y., Cui, J., Wu, J., Li, Y., Zhu, T., Kang, H., Yang, J., Sun, J., Qin, Y., Zhang, Y., Ajayan, P. M., Wu, Y.: Water-Soluble Defect-Rich MoS2 Ultrathin Nanosheets for Enhanced Hydrogen Evolution. J. Phys. Chem. Lett. 10. 3282-3289. (2019)

[155] X. Li, W. Cai, J. An, S. Kim, J. Nah, D. Yang, R. Piner, A. Velamakanni, I. Jung, E. Tutuc, S. K. Banerjee, L. Colombo, R. S. Ruoff, *Science,* 2009, *324*, 1312-1314.

[156] Xie, J., Zhang, H., Li, S., Wang, R., Sun, X., Zhou, M., Zhou, J., Lou, X. W., Xie, Y.: Defect-Rich MoS2 Ultrathin Nanosheets with Additional Active Edge Sites for Enhanced Electrocatalytic Hydrogen Evolution. Adv. Mater. 25. 5807-5813. (2013)

[157] Ye, G., Gong, Y., Lin, J., Li, B., He, Y., Pantelides, S. T., Zhou, W., Vajtai, R., Ajayan, P. M.:

Defects Engineered Monolayer MoS2 for Improved Hydrogen Evolution Reaction. Nano Lett. 16. 1097-1103. (2016)

[158] Li, H., Tsai, C., Koh, A. L., Cai, L., Contryman, A. W., Fragapane, A. H., Zhao, J., Han, H. S., Manoharan, H. C., Abild-Pedersen, F., Nørskov, J. K., Zheng, X.: Activating and optimizing MoS2 basal planes for hydrogen evolution through the formation of strained sulphur vacancies. Nat. Mater. 15. 48-53. (2016)

[159] K. S. Novoselov, A. Mishchenko, A. Carvalho, A. H. Castro Neto, *Science* 2016, *353*, aac9439.

[160] M. Gong, W. Zhou, M.-C. Tsai, J. Zhou, M. Guan, M.-C. Lin, B. Zhang, Y. Hu, D.-Y. Wang, J. Yang, S. J. Pennycook, B.-J. Hwang, H. Dai, Nat. Commun. 2014, 5, 4695.

[161] N. Yang, Z. Zhang, B. Chen, Y. Huang, J. Chen, Z. Lai, Y. Chen, M. Sindoro, A.-L. Wang, H. Cheng, Z. Fan, X. Liu, B. Li, Y. Zong, L. Gu, H. Zhang, *Adv. Mater.* 2017, *29*, 1700769.

[162] H. Duan, N. Yan, R. Yu, C.-R. Chang, G. Zhou, H.-S. Hu, H. Rong, Z. Niu, J. Mao, H. Asakura, T. Tanaka, P. J. Dyson, J. Li, Y. Li, *Nat. Commun.* 2014, *5*, 3093.

[163] F. Saleem, B. Xu, B. Ni, H. Liu, F. Nosheen, H. Li, X. Wang, *Adv. Mater.* 2015, *27*, 2013-2018.

[164] aD. Voiry, M. Salehi, R. Silva, T. Fujita, M. Chen, T. Asefa, V. B. Shenoy, G. Eda, M. Chhowalla, Nano Lett. 2013, 13, 6222-6227; bM. A. Lukowski, A. S. Daniel, C. R. English, F. Meng, A. Forticaux, R. J. Hamers, S. Jin, Energy Environ. Sci. 2014, 7, 2608-2613.

[165] X. Geng, W. Sun, W. Wu, B. Chen, A. Al-Hilo, M. Benamara, H. Zhu, F. Watanabe, J. Cui, T.-p. Chen, Nat. Commun. 2016, 7, 10672.

Note: Part of this chapter has been published in **Chemistry–A European Journal.** Permission regarding copyright has been obtained from the publishers. [Yaping Chen, Kun Rui, Jixin Zhu, Shi Xue Dou, Wenping Sun* Recent Progress on Nickel‐Based Oxide/(Oxy) Hydroxide Electrocatalysts for the Oxygen Evolution Reaction. **Chem. Eur. J. 2019, 25, 703.**]

Chapter 3

3. Experimental procedure

3.1. Overview

The experimental procedures are displayed in **Figure 3.1**. In general, the electrocatalysts are prepared mainly based on liquid methods. Sintering method might be employed for tuning their crystallinity or phase structures. Then the material's constituent, structure, and element states are evaluated based on several modern material characterization methods, aiming to provide essential information on the atomic and electronic structures of the electrocatalysts. Meanwhile, the electrochemical performance of the electrocatalysts is accessed. At last, the in-depth mechanism of the reaction is explored, and the structure-activity relationship is discussed.

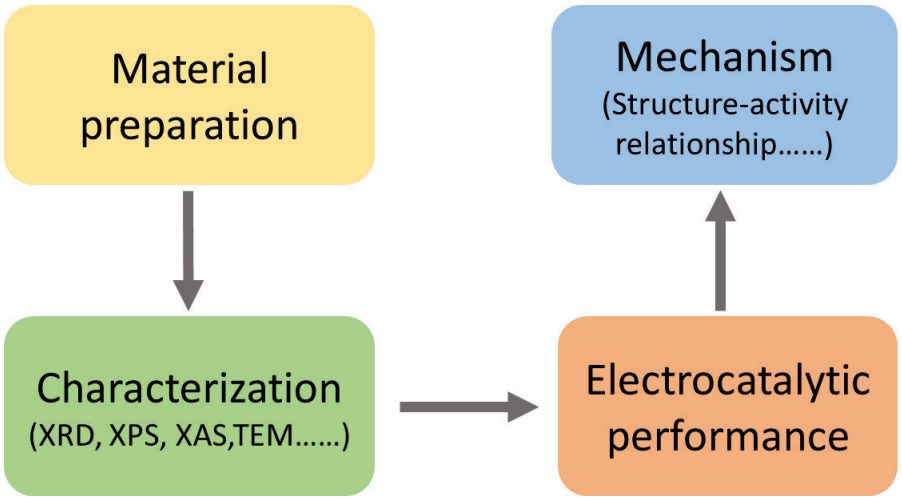

Figure 3.1. The flow chat of general experimental procedures.

3.2. Chemicals and Materials

The chemicals and materials used in this thesis are listed in Table 3.1. The chemicals are used as received without further purification. Ultrapure deionized water (DI water, 18 MΩ cm^{-1}) was used through this thesis work, which is generated using a Milli-Q® systems in ISEM, UOW.

Table 3.1. Chemicals and materials.

Chemicals	Formula/ abbreviation	Purity (%)	Supplier
Ethanol	C_2H_5OH/ EtOH	96	Chem-Supply Pty. Ltd.

Isopropanol	C_3H_8O/ IPA	99	Chem-Supply Pty. Ltd.
Ethylene glycol	$C_2H_6O_2$/ EG	99.8	Sigma-Aldrich
Sodium borohydride	$NaBH_4$	>96	Sigma-Aldrich
Sodium molybdate	Na_2MoO_4	98	Sigma-Aldrich
Selenium powder	Se	>99.5	Sigma-Aldrich
Potassium hexachloroiridate(IV)	K_2IrCl_6	Technical grade	Sigma-Aldrich
Chloroplatinic acid hexahydrate	$H_2PtCl_6 \cdot 6H_2O$	ACS reagent	Sigma-Aldrich
Cobalt(II) nitrate hexahydrate	$Co(NO_3)_2 \cdot 6H_2O$	>98.5	Sigma-Aldrich
Nickel(II) nitrate hexahydrate	$Ni(NO_3)_2 \cdot 6H_2O$	>98.5	Sigma-Aldrich
Nickel (II) chloride hexahydrate	$NiCl_2 \cdot 6H_2O$	ReagentPlus®	Sigma-Aldrich
Ammonium molybdate tetrahydrate	$(NH_4)_6Mo_7O_{24} \cdot 4H_2O$	99.98	Sigma-Aldrich
Hexamethylenetetramine	$C_6H_{12}N_4$/ HMTA	≥99.0%	Sigma-Aldrich
Urea	CH_4N_2O	≥98%	Sigma-Aldrich
Thiourea	CH_4N_2S	>99	Sigma-Aldrich
Hexagonal boron nitride	h-BN	99	Thermal Scienctific
Potassium hydroxide	KOH	85	Chem-Supply Pty. Ltd.
Sulfuric acid	H_2SO_4	98	Sigma-Aldrich
Sodium tetrachloropalladate(II)	Na_2PdCl_4	98	Sigma-Aldrich
Nafion® 117 solution		5	Sigma-Aldrich

3.3. Materials Preparation

In this doctoral work, the electrocatalysts are mainly synthesized by wet-chemical method involving hydrothermal/solvothermal method, oil bath method, ultrasonic assisted method, etc. Generally, wet-chemical methods involve dispersing reactants into liquid solvents like water, EtOH, EG, etc., and then the reactions occur in the solutions. The morphology of as-prepared materials can be controlled by the varying concentration of precursors, the type of solvents, reaction temperature, and reaction time. Owing to their versatility, these wet-chemical methods now have been widely used for preparing 2D nanomaterials.

3.4. Characterization Techniques

3.4.1. XRD

XRD, a general and rapid analytical modern technique, can be used to identify the composition and crystalline characteristics of materials. Crystals are composed of regular atom arrays, and X-rays can be scattered when the incident X-rays interact with these atoms, leading a regular array of waves. When the Angle between the X-ray and the crystal changes, the intensity diagram of the scattered X-ray is recorded. In some specific directions, these scattered waves may add constructively, leading to well-defined peaks. When the X-rays arrive at the lattice planes of the crystal materials, interference will occur as the Bragg's law: $2dsin\theta = n\lambda$, where d represents the lattice spacing, θ is the incident angle of X-ray, n stands for any integer, and λ is the wavelength of X-ray. By comparing the measured peak positions with standard PDF cards, the crystal phases of the tested materials can be confirmed.

In this doctoral work, the crystalline characteristics of the as-prepared materials were recorded using a GBC enhanced mini-materials analyzer with $Cu_{K\alpha}$ radiation at a scan rate of 2 ° min^{-1} (Scientific Equipment LLC, Hampshire, IL, USA, λ = 1.541 Å, 25 mA, 40 kV) in AIIM, UOW.

3.4.2. XPS

XPS is a typical quantitative spectroscopic technique, it can be used for characterizing the materials surface composition and chemical state. Typically, a beam of X-rays irradiates the tested materials, and then the electrons within the materials obtain energy from the X-rays and escape from the surface of the material. The XPS spectra are recorded by irradiating the sample with a beam of X-rays, while simultaneously measuring the kinetic energy and number of electrons. XPS can be used to confirm the kind of elements in the measured material, and accordingly provide basic information on the chemical state of the elements. XPS is also an indispensable tool for accessing the interfacial electron interactions between different components of heterostructures. Typically, the electronic interaction modifies the chemical states of the interface, manifesting as a binding energy shift in XPS spectra. In this doctoral work, the XPS measurements were performed using a Thermo ESCALAB 250Xi instrument, and the binding energies were calibrated using the advantageous C 1s signal at 284.8 eV as a reference.

3.4.3. SEM

SEM is an electron microscopy technique for the surface morphology characterization. The incident electron beam scans the surface of samples, and the generated secondary electrons are used for creating image. The morphology and elemental composition of the materials can be observed via interaction between the electrons and the atoms in the materials. In this thesis, the sample morphologies were

characterized by a JEOL JSM-7500FA field-emission scanning electron microscope (FESEM) at an accelerating voltage of 5 kV in the EMC, UOW.

3.4.4. TEM

TEM is another important microscopy technique for material characterization including morphology, crystal structure, and electronic structure of a specimen, in which a beam of accelerated and focused electrons is transmitted through the sample to form an image. The sample should be less than 100 nm thickness, if not, the electron beam cannot successfully transmit through the material, leading to the failure of sample characterization. SAED is a crystallographic experimental technique that can be used inside the TEM. SAED can be applied to identify the crystal defects and crystal structures. SAED is different from conventional TEM, in which the electron beam is focused on a size-limited spot and scans over the sample in a raster pattern. The raster of the beam across the sample makes it available for various analysis techniques such as mapping by EDS, EELS, and HAADF imaging. These signals can be acquired simultaneously for the direct correlation of the image and quantitative data. In this doctoral work, TEM images are recorded by a JEM-2010 microscopy operating at a working voltage of 200 kV. STEM images are acquired on a probe-corrected JEOL ARM200F TEM operated at 80 kV equipped with a thermal field emission gun and an ultrahigh resolution pole-piece. Energy disperse X-ray mappings (EDS) were acquired on FEI Talos F200X equipped with four symmetrical EDS signal detectors, operated at 200 kV.

3.4.5. XAFS

XAFS is a widely used technique for the characterizing the electronic structures as well as the coordinate environment of selected elements. XAFS is a bulk-sensitive technique which provides averaged information. Based on the kinetic energy range, the XAFS spectra can be divided into XANES and EXAFS. The kinetic energy of XANES in the range from 10 to 150 eV above the chemical potential, called "shape resonances" in molecular spectra since the final states of short lifetime degenerate to the continuum with the Fano line-shape. EXAFS spectra dominated in the high kinetic energy range of the photoelectron the scattering cross-section with neighbor atoms, is obtained due to the interference between the excited and the single-backscattered photoelectrons, which provide details on coordination number, bond distance, and neighbor species of the absorbed atoms.

In this work, XAFS measurements at Pd k-edge in both transmission (for Pd foil) and fluorescence (for samples) mode were carried out at beamline BL14W1 in Shanghai Synchrotron Radiation Facility (SSRF).

The operation energy of storage ring was 3.5 GeV and at the current around 240 mA. The white X-ray was monochromatized using a fixed-exit double-crystal Si (111) monochromator and the energy was calibrated by using Pt foil. Pd standards and the prepared samples were compacted and collected in transmission mode at room temperature.

3.4.6. FT-IR

FT-IR is a spectroscopic technique which can be used to analyse the molecular structures and chemical compositions via detecting the material-characteristic absorption of infrared radiation with different wavelengths. The molecules, especially the organic molecules, and atoms that consist of the chemical bonds or functional groups are in the state of constant vibration. Because the vibration frequency is equivalent to the infrared vibration frequency, when the molecule is irradiated by infrared, the chemical bonds or functional groups in the molecule will vibrate and absorb. Different chemical bonds or functional groups possess different absorption frequencies, which are corresponding to characteristic peaks in the FT-IR spectrum. Thus, the information of the chemical bonds or functional groups can be acquired. In this work, the FT-IR spectrum was characterized by using a Shimadzu FTIR Prestige-21 in UOW with the range from 4000 cm^{-1} to 500 cm^{-1}.

3.5 Electrochemical Measurements

3.5.1. Three electrode system setup

In this work, The electrochemical measurements were performed on electrochemical workstation (Multichannel potentiostat/galvanostat VSP-300, BioLogic Science Instrument) connected to rotating disk electrode (Pine Research Instruments, Inc). Before the HER measurement, the electrolyte should be continuously feed by high purity N_2 for 30 min to remove the dissolved oxygen gas so as to prevent from occurring ORR. The Hg/HgO and Ag/AgCl reference electrode can be employed in different pH electrolyte according to their special properties. A Pt mesh electrode was used as the counter electrode for the HER ,OER and ORR. For the preparation of catalyst dispersions, 2 mg of catalysts are added into the mixture of 16 μL 5% Nafion solution, 100 μL IPA and 384 μL DI water, followed by ultrasonication for 2 h. The working electrode was prepared by dropping 10 μL aliquot of catalyst dispersion on a glassy carbon rotating electrode with a diameter of 5 mm (effective working area, 0.19625 cm^{-2}). The mass loading of all catalysts on glassy carbon was 0.203 mg cm^{-2}.

3.5.2. Overpotential

Overpotential, is the potential difference (voltage) between a half-reaction's thermodynamically

determined reduction potential and the potential at which the redox event is experimentally observed. It is regarded as one of the most important parameters for accessing the catalytic performance of water splitting system. Generally, it is the larger overpotential that will lead to the lower energy conversion efficiency of the electrochemical water electrolysis system. Linear sweep voltammetry (LSV) is commonly used to obtain the overpotential to evaluate the catalytic activity at a certain current density of 10 mA cm^{-2}, The current density is usually determined with respect to the geometric area of the electrode, which can also be calculated based on the specific geometric area of the catalyst, the electrochemical active specific area (ECSA) of the catalyst, or the catalyst mass. LSVs can be performed on a rotate disk electrode (RDE) system. The electrode continuously rotates when recording linear sweep voltammetry (LSV) curves to efficiently minimize the diffusion overpotential. The overpotential could activate the reaction to diffuse charge carriers. Meanwhile, the resistance overpotential can be corrected by IR compensation (eq. 3.1), where I is the current flowing in the circuit and Rs is the series resistance.

$$E_{corrected} = E_{uncorrected} - IR \tag{3.1}$$

3.5.3. Tafel slope and exchange current density

Tafel slope, a linear relationship between overpotential and log-current, are an inherent property of multi-step heterogeneous electrocatalytic reactions, which can uncover the reaction mechanism of HER on the catalyst surface. Generally, determining the Tafel slope derivatives to the theoretical Tafel slope can infer the reaction order and rate determining step (RDS). For HER process, the ideal Tafel slope for the Volmer step, the Heyrovsky step and the Tafel step is 120, 40 and 30 mV dec^{-1}, respectively. When the actual Tafel slope on the surface of the commercial Pt in 0.5 M H_2SO_4 is close to 30 mV dec^{-1}, demonstrating that the reaction pathway is dominated by the Volmer-Tafel process and the RDS for the reaction is the Tafel step. Following the generally accepted mechanism of the HER involving the initial proton discharge step to form the adsorbed hydrogen intermediate, which is desorbed either chemically or electrochemically, generalized expressions for the Tafel slope, reaction order and the a.c. impedance for the hydrogen evolution reaction are derived using the steady-state approach, taking into account the forward and backward rates of the three constituent paths and the lateral interactions between the chemisorbed intermediates.

The exchange current density is the rate of hydrogen evolution per surface area at the electrode potential, where the reaction is at equilibrium. It also represents the catalytic ability of a given metal to catalyze. Specifically, exchange current density reflects the intrinsic activity of charge transfer between electrode

and electrolyte, and to catalyze a reaction is to promote the exchange current density. It can be read out from the intersection of the extrapolated linear part of Tafel plots and the X-axis. The exchange current density tends to be larger on the surface of catalysts with higher catalytic activity.

3.5.4. Turnover frequency

The turnover frequency (TOF) is the number of the product molecule generated per active site in unit time (equation 10).[194–195] According to the definition, H_2 should be collected to evaluate the number of the H_2 molecules. Assuming the Faradic efficiency of 100%, the theoretical number of H_2 can be calculated from the charge flowing through the circuit based on the Faraday's laws of electrolysis (equation 11), where n is the amount of substance (mol), I is current (A), z is electron number transferred per molecule, and F is the Faraday constant (96485 C mol^{-1}). Then a TOF vs. overpotential curve can be achieved (eq. 3.2) according to eq. 3.3 together with eq. 3.4. Consequently, calculating TOF largely hinge on determining the number of active sites, which can be evaluated by various methods including the copper underpotential deposition method, calculating the number of molecules on the exposed surface,[196–198] or quantifying from CV tests.[106, 199–200] Apparently, to achieve a reasonable TOF or TOF-overpotential curve depends on how to define and evaluate the number of active sites. It is noteworthy that the overpotential value should always be indicated when reporting the TOF values since TOF increases with increasing overpotentials.

$$\mathrm{TOF} = \frac{Molecule\ number\ of\ product}{Number\ of\ active\ sites} \times \frac{1}{Unit\ time} \tag{3.2}$$

$$\mathrm{n} = \frac{It}{zF} \tag{3.3}$$

$$\mathrm{TOF} = \frac{I \times N_A}{zF \times Number\ of\ active\ sites} \tag{3.4}$$

3.5.5. Half-wave potential

Half-wave potential ($E_{1/2}$) is a potential at which polarographic wave current is equal to one half of diffusion current. In a given supporting electrolyte, the half-wave potential is unique for each element and its different valence states and chemical forms. Generally, it can be used to evaluated the catalytic kinetic, higher $E_{1/2}$ value, better catalytic kinetics.

Chapter 4

4. Electrochemically Inert g-C_3N_4 Promotes Water Oxidation Catalysis

4.1 Introduction

Recently, ever-increasing research interest has been focused on developing alternative strategies to efficiently utilize sustainable renewable energy worldwide. In addition to grid-scale energy storage, energy conversion, which means converting renewable energy into various chemical energies, is another important avenue. Water electrolysis (electrochemical water splitting) is one typical chemical process that converts electricity derived from renewable energy into hydrogen, and also presents a clean and potentially cost-effective pathway to achieve renewable energy conversion.[1] Compared with hydrogen evolution reaction (HER), oxygen evolution reaction (OER) is much more sluggish because four electrons need to be removed to form oxygen, and hence water electrolysis efficiency is greatly hindered by kinetically sluggish OER. On the other hand, OER is also an important half reaction involved in rechargeable metal–air batteries, and the corresponding OER reaction kinetics determines the battery performance as well.[2] Therefore, developing highly-efficient catalysts for OER are extremely urgent to address the challenges in artificial water-splitting systems and metal-air batteries.[3] Some noble-metal catalysts such as Ru- and Ir-based materials are state-of-the-art OER electrocatalysts; however, the considerable scarcity and high cost seriously limit their practical applications.[4] It is thus critical to explore low-cost and stable alternatives with promising catalytic performance towards water oxidation. To date, numerous efforts have been undertaken to design non-precious OER catalysts,[5] and non-precious metal-based oxides,[6] hydroxides,[7] and carbonaceous materials[8] have drawn much reacearch attention. In particular, Ni-based hydroxides and oxides demonstrated outstanding OER catalytic activities with a low overpotential and high electrolysis current in alkaline electrolytes.[5a, 7a]

In order to further enhance the electrocatalytic activity of the aforementioned Ni-based catalysts, current strategies mainly focuse on heteroatom doping, designing and synthesizing highly efficient nanostructures/nanocomposites.[7b, 7c, 9] It should be mentioned that most approaches aim to improve the intrinsic activity, expose more active sites, and/or enhance charge transfer ability of the catalysis. As is already known, in addition to exposed active sites and charge transfer ability, the electrocatalytic performance of the heterogeneous catalysis has close correlation with the adsorption and desorption

properties of the electrode surface, which determine the mass-diffusion kinetics of both the reactants and products. The adsorption of reactants/intermediate and desorption of products on the catalyst surface is forcefully affected by the catalyst wettability.[10] Bhaumik et al. displayed the hydroxylation of benzene to increase the hydrophobicity, which more profitably adsorbs and transfers the hydrophobic benzene reactant in the triphasic system.[10a] Li et al. successfully achieved enhanced water oxidation catalysis on phosphorylated NiFe hydroxide by tuning catalyst wettability.[10d] In this regard, engineering electrode materials with superwettability has a prominent aspect on promoting electrolyte penetration, mass diffusion and charge transfer as well, thereby achieving enhanced electrocatalytic activity.

Recently, 2D graphitic carbon nitride g-C_3N_4 (GCN) has been widely implemented in the photocatalysis field due to its unique electronic band structure and high physicochemical stability.[11] Some effort has already been made to study GCN-based composites as electrocatalysts for water splitting.[12] It was found that bare GCN is nearly inert for OER and hydrogen evolution reaction (HER), and the delivered catalytic performance is mainly ascribed to the synergistic effect of GCN and the conductive carbonaceous materials (e.g., CNT and graphene). Nevertheless, some unique physicochemical properties of GCN make it an attractive component for constructing high-performance electrocatalysis occurred in aqueous environment. It is worth noting that proton-functionalized GCN nanosheets show excellent water dispersion stability, and this would substantially improve the wettability of the composites containing such GCN nanosheets.[13] Besides, the GCN nanosheets can help achieve good dispersion and hinder agglomeration of active materials, ensuring substantial exposure of the active sites. Moreover, the excellent chemical stability enables GCN to function as a robust substrate for active materials towards durable performance.[14] Based on the aforementioned statement, we speculate that the catalyst hydrophicility would be greatly improved over bare $Ni(OH)_2$ by constructing GCN/$Ni(OH)_2$ (GCNN) hybrid. Besides, the introduction of GCN would efficiently realize good dispersion and hinder aggregation of $Ni(OH)_2$. These two unique properties together with the excellent stability of GCN would help the GCNN hybrid to achieve highly efficient and durable water oxidation catalysis. Herein, 2D GCNN hybrid with monodispersed $Ni(OH)_2$ nanoplates strongly coupled with GCN nanosheets were prepared by a facile one-pot hydrothermal process. As expected, the $Ni(OH)_2$ nanoplates are uniformly dispersed on GCN nanosheets, and the GCNN hybrid shows superhydrophilicity. Although the intrinsic electrocatalytic ability of GCN is negligible and less catalytic active material $Ni(OH)_2$ is present, the GCNN hybrid delivers significantly enhanced electrocatalytic ability for OER as compared with bare

ultrathin $Ni(OH)_2$ nanosheets. The excellent electrochemical performance suggests that, in addition to improve intrinsic catalytic ability and expose more active sites, engineering an efficient catalyst surface is also vital to gain accelerated catalytic reaction kinetics.

4.2. Experimental Section

4.2.1. Materials

All the chemicals were purchased from Sigma-Aldrich (A.R) and were used as received without further purification.

4.2.2. Materials Preparation

4.2.2.1. Preparation of Functionalized GCN

Bulk GCN powders were prepared by calcining melamine as precursor in air at 550 °C for 2 h with a heating rate of 2.3 °C min^{-1}. For the functionalization of GCN, bulk GCN powders were dispersed in 6 M HCl with ultrasonication for 1 h, and then stirred for 4 h at room temperature.[13] The functionalized GCN was centrifuged and washed with deionized water for several times.

4.2.2.2. Preparation of GCNN Nanocomposites

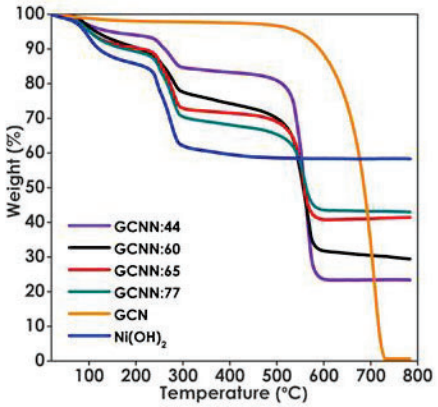

Figure 4.1. TGA curves of GCNN, GCN and $Ni(OH)_2$.

The as-prepared samples are named as GCNN:x, where "x" means the mass percentage content of $Ni(OH)_2$ in the hybrid, which is calculated based on the TGA results (**Figure 4.1**). Take the synthesis of GCNN:65 for an example, 20 mg functionalized GCN and 250 mg $Ni(NO_3)_2 \cdot 6H_2O$ were dispersed in 15 ml ethylene glycol followed by adding 20 ml deionized water with unltrasonication for 4 h. Then 103.2 mg urea was added into the above mixture under magnetic stirring to become homogeneous suspension. Next, the above reaction mixture was transferred to a Teflon stainless-steel autoclave with a capacity of

50 mL. The autoclave was sealed and heated at 120 °C for 10 h in an electric oven. The resulting products were collected by centrifugation and washed with ethanol and deionized water for three times respectively, and were eventually dried at 60 °C in oven overnight. Similarly, GCNN:x (x=44, 60, 77) was synthesized following the same procedure by adding different quantities of precursors (50, 30, 10 mg GCN, 156.2, 187.5, 281.7 mg $Ni(OH)_2$ and 64.5, 77.4, 116.3 mg urea for GCNN:44, GCNN:60, GCNN:77, respectively).

4.2.2.3. Preparation of $Ni(OH)_2$ and $Co(OH)_2$

Pure $Ni(OH)_2$ and $Co(OH)_2$ nanosheets were synthesized via a similar hydrothermal process. For $Ni(OH)_2$, 250 mg $Ni(NO_3)_2 \cdot 6H_2O$ and 103.2 mg urea were dissolved in mixed solvent containing15 ml ethylene glycol and 20 ml deionized water under magnetic stirring. For $Co(OH)_2$, 261.9 mg $Co(NO_3)_2 \cdot 6H_2O$ and 252.3 mg hexamethylenetetramine (HMT) worked as precursors instead. Then, the solution was transferred to a Teflon stainless-steel autoclave with a capacity of 50 mL. The autoclave was sealed and heated at 120 °C for 10 h in an electric oven. The resulting products were collected by centrifugation and washed with ethanol and deionized water for three times respectively, and were eventually dried at 60 °C in oven overnight.

4.2.3. Materials Characterization

X-ray diffraction (XRD) was carried out using GBC MMA X-ray diffractometer (λ = 1.5406 Å, 25mA, 40 Kv, step size of 0.02 ° s^{-1}). Fourier transform infrared (FTIR) spectra of the samples employed KBr as the background were determined by a Shimadzu FTIR Prestige-21 spectrometer in the frequency range of 4000–650 cm^{-1} with a resolution of 4 cm^{-1}. The morphology and microstructures of the samples were characterized by the field emission scanning electron microscope (FESEM, JEOL JSM-7500FA) equipped with energy-dispersive X-ray spectroscopy (EDS) and resolution transmission electron microscopy (HRTEM, JEM-2010, working voltage 200 kV) and selected area electron diffraction (SAED). X-ray photoelectron spectroscopy (XPS) measurements were carried out on a Thermo ESCALAB 250Xi instrument, using monochrome Al Ka (*hv* =1486.6 eV) as the X-ray excitation source. Contact angles were measured by Dataphysics OCA15 with 2 μL 1 M KOH solution for each testing. Three different spots per substrate on three different areas were measured. Thermogravimetric analysis (TGA): TGA (Mettler Toledo TGA/DSC 1) were performed from 30 to 780 °C at a heating/cooling rate of 10 °C min^{-1} in air to characterize the thermophysical properties.

4.2.4. Electrochemical Measurement

Rotating disk electrode and WaveDriver 20 bipotentiostat/galvanostat system (Pine Instruments) were used for electrochemical measurement. All electrocatalytic measurements were conducted in 1 M KOH aqueous solution employing Ag/AgCl (saturated KCl solution) as the reference electrode, a platinum wire as the counter electrode, and the glassy carbon electrode (0.196 cm^{-2} of effective working area) coated with different catalysts as the working electrodes. For the preparation of working electrodes, 2 mg catalysts were dispersed in a mixed solution containing 16 µL Nafion solution (Aldrich Co., 5 wt%), 384 µL deionized water and 100 µL isopropanol via sonicating for 30 min to obtain a homogeneous ink. Then 10 µL of the catalyst ink (containing 40 µg of catalyst) was cast onto the polished glassy carbon electrode, and subsequently the electrode was dried in ambient air. During the measurements, the working electrode was constantly rotated at 1600 rpm to remove generated O_2. LSV polarization curves were performed at 5 mV s^{-1} to demonstrate the OER activity. All LSV curves were corrected with 95% iR-compensation. Cyclic voltammetry (CV) was first conducted from 1.02 V to 1.62 V vs RHE at a scan rate of 10 mV s^{-1} to activate the catalysts before LSV test. Chronoamperometry measurement was conducted under the same potential of 0.6 V (vs. Ag/AgCl) to study the durability. Electrochemical impedance spectra (EIS) were measured at 0.6 V (vs. Ag/AgCl) in the frequency range of 0.1−100 kHz. The electrochemically active surface area (ECSA) is estimated based on the measured double-layer capacitance (C_{DL}) of the synthesized electrodes in 1 M KOH according to the reported method.[4c] The ECSA values were calculated according to the following equations:

$$i_c = vC_{DL} \quad (4.1)$$

Where the charging current i_c, is equal to the product of the electrochemical double layer capacitance C_{DL} and the scan rate v.

$$ECSA = \frac{C_{DL}}{C_S} \quad (4.2)$$

Here we can calculate the ECSA with C_{DL} and a general C_s = 0.04 mF cm^{-2} in 1 M KOH based on a typical reported value.

4.3. Results and Discussion

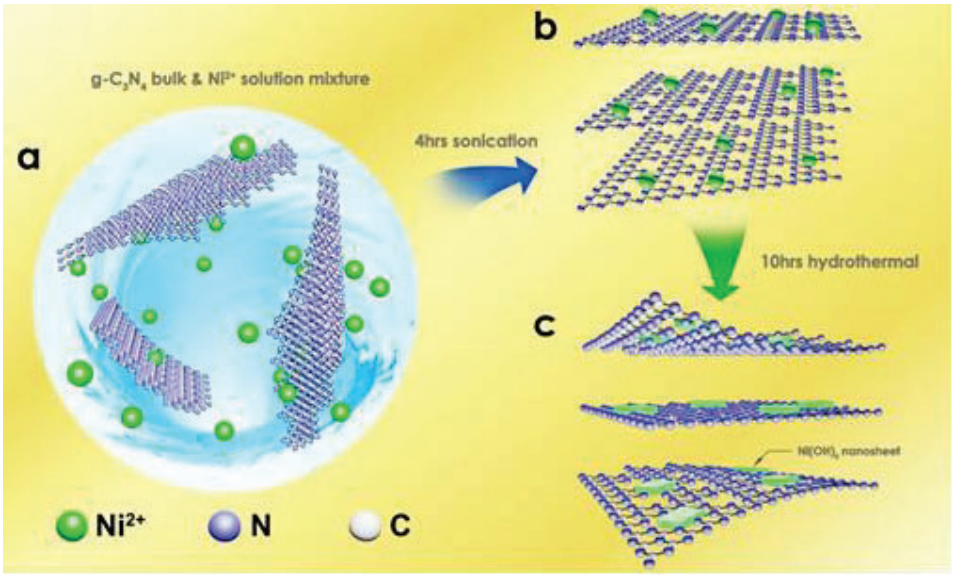

Figure 4.2. Schematic illustration of the synthesis of GCNN nanocomposites.

The schematic illustration of the synthetic route toward 2D GCNN hybrids is displayed in **Figure 4.2**. Firstly, Ni^{2+} ions are intercalated into the interlamination via ultrasonication treatment and this could effectively promote the exfoliation of functionalized GCN with lots of protons and aminos.[15] During the hydrothermal process, the adsorbed Ni^{2+} cations participate into the homogeneous precipitation reaction and form $Ni(OH)_2$ nanoplates on GCN nanosheets. It should be noted that the hydrothermal process also facilitates the exfoliation of GCN.

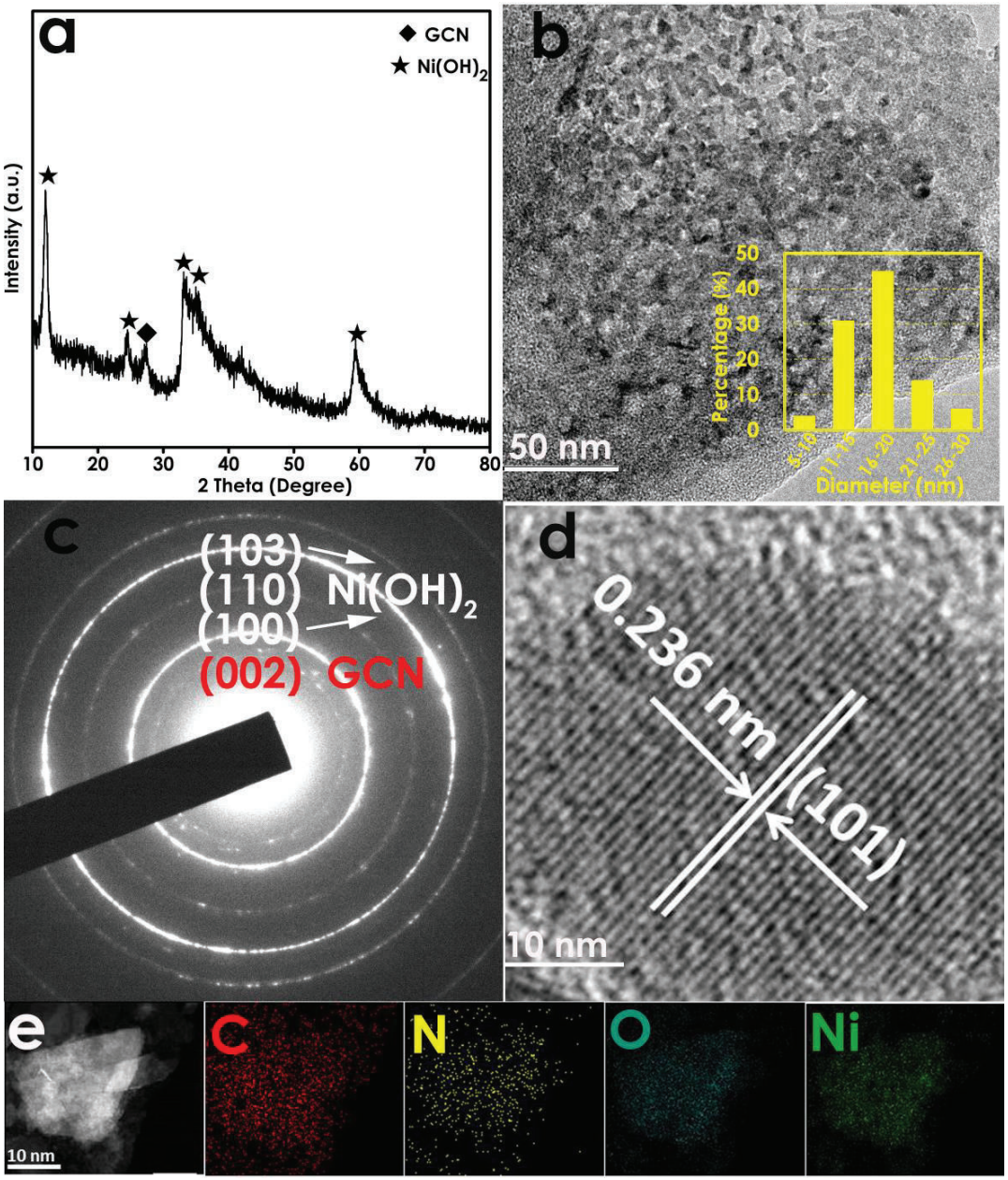

Figure 4.3. (a) XRD, (b) TEM image (inset: statistical result of the diameters of $Ni(OH)_2$ nanoplates), (c) SAED, (d) HRTEM, and (e) Dark-field STEM image and corresponding elemental mappings of GCNN:65.

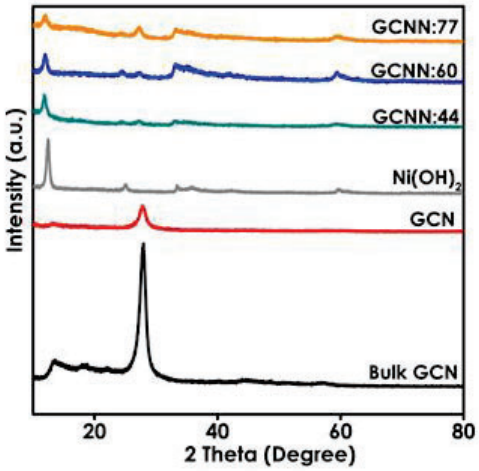

Figure 4.4. (a) XRD patterns of GCNN:77, GCNN:60, GCNN:44, pure $Ni(OH)_2$, functionalized GCN and bulk GCN.

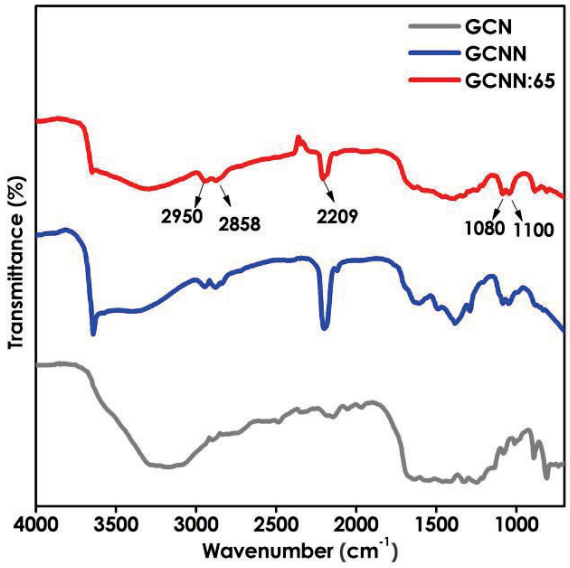

Figure 4.5. (a) FTIR of GCNN:65, pure $Ni(OH)_2$ and GCN.

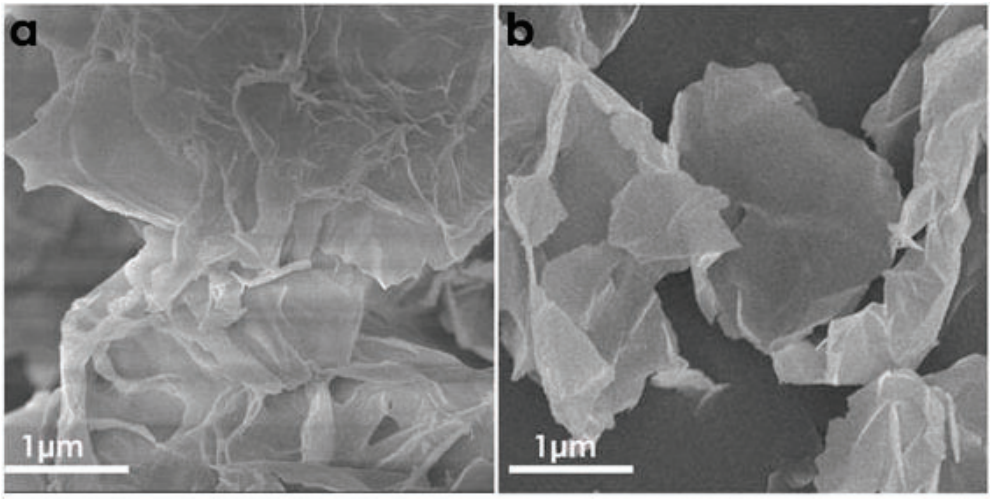

Figure 4.6. Typical SEM image of (a) the GCNN:65 and (b) pure $Ni(OH)_2$.

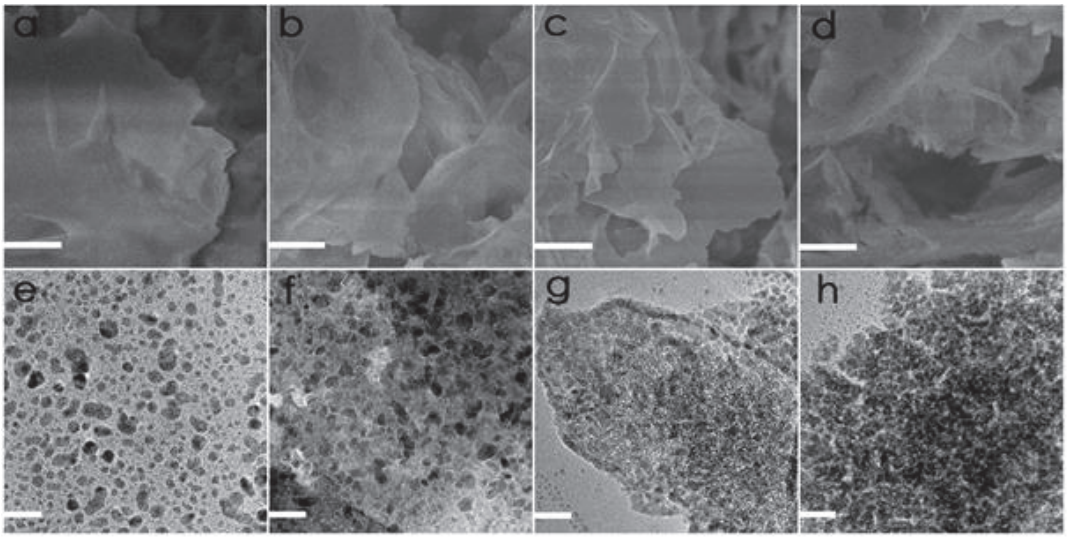

Figure 4.7. (a-d) SEM images of GCNN:44, GCNN:60, GCNN:65, GCNN:77 (scale bar: 100 nm). (e-h) TEM images of GCNN:44, GCNN:60, GCNN:65, GCNN:77 (scale bar, 50 nm).

Figure 4.3a shows the X-ray diffraction (XRD) pattern of the as-prepared GCNN:65 (65 wt% $Ni(OH)_2$) nanocomposite. It can be seen that the XRD pattern contains typical diffraction peaks of hexagonal phase α-$Ni(OH)_2$ and GCN, reflecting that the formation of GCNN.[16] Notably, the intensity of the GCN (002) peak at 27.4°, corresponding to the characteristic interlayer stacking structure, is evidently reduced compared to bulk GCN (**Figure 4.4**), indicating the formation of few-layered nanosheets.[13] Besides, all the other GCNN samples possess similar crystal structures (**Figure 4.4**). Fourier-transform infrared spectroscopy (FTIR) (**Figure 4.5**) further confirms the formation of GCNN:65. The broad band locating from 3200 cm^{-1} to 3600 cm^{-1} corresponds to the O-H vibration of hydrogen-bonded hydroxyl groups of $Ni(OH)_2$.[17] The strong absorption band located at 2202 cm^{-1} is the typical vibration of C≡N triple bonds

in the OCN^- anions produced in the urea hydrolysis.[18] The distinctive stretch mode of aromatic CN heterocycles from 1100 to 1600 cm^{-1} coupled with the breathing mode of the triazine units at 810 cm^{-1} evidence the presence of GCN.[19] Scanning electron microscopy (SEM) and transmission electron microscopy (TEM) characterizations were conducted to investigate the sample morphology. The SEM (**Figure 4.6a**) result suggests that GCNN:65 have flexible nanosheets morphology. As shown in **Figure 4.3b**, $Ni(OH)_2$ nanoplates (around 10-30 nm in lateral size) are strongly coupled with GCN nanosheets. As a functional substrate similar to graphene-like structures, the GCN nanosheets could effectively prevent $Ni(OH)_2$ nanoplates from agglomeration, ensuring the maximum exposure of active sites. Comparably, GCNN:44, GCNN:60, GCNN:77 exhibit disciplinary changes with increased amount of nickel precursors, the $Ni(OH)_2$ nanoplates tend to be dispersed on the surface of GCN nanosheets based on the extent of darkness (**Figure 4.7**). In contrast, bare $Ni(OH)_2$ nanosheets synthesized via similar process show flexible nanosheets morphology, which is several micro in lateral size (**Figure 4.6b**). The selected area electron diffraction (SAED) pattern can be fully indexed to the hexagonal α-$Ni(OH)_2$ phase (**Figure 4.3c**). A lattice spacing of 0.236 nm determined from the HRTEM image (**Figure 4.3d**) can be assigned to the (101) plane of $Ni(OH)_2$. Furthermore, the scanning transmission electron microscopy (STEM) elemental mappings (**Figure 4.3e**) show the uniform distribution of C, N, O and Ni across the GCNN:65 composite nanosheet, indicating the uniform hybridization of $Ni(OH)_2$ nanoplates and GCN nanosheets.

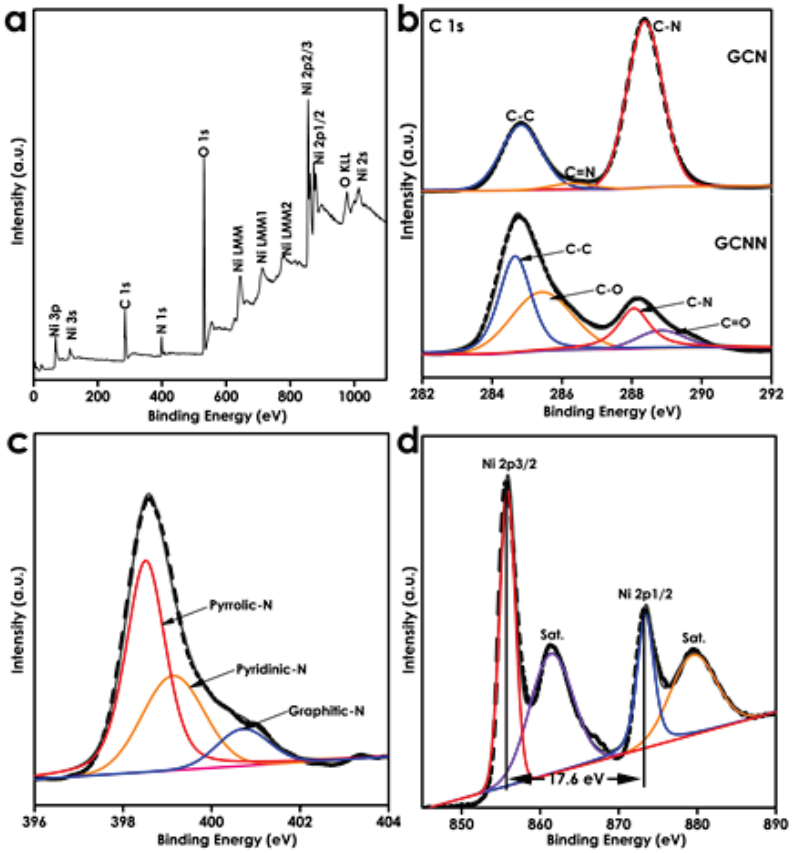

Figure 4.8. XPS spectra of GCNN:65: (a) survey spectrum, (b) C 1s, (c) N 1s and (d) Ni 2p.

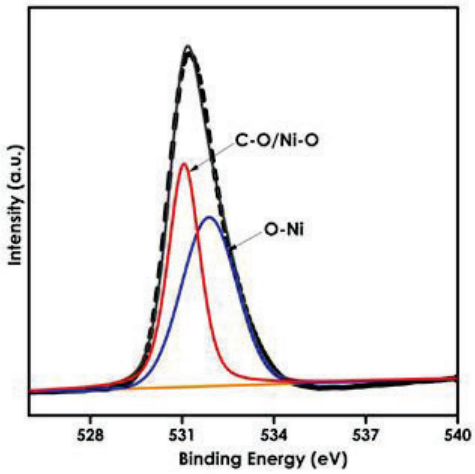

Figure 4.9. O 1s spectrum of GCNN:65.

The elemental composition and chemical states of GCNN:65 nanocomposite was also investigated by X-ray photoelectron spectra (XPS) analysis. The survey spectrum (**Figure 4.8**a) reveals the co-occurrence of

C, N, O and Ni elements.[20] C 1s spectra of GCN and GCNN:65, as shown in **Figure 4.8b**, show totally distinct profiles. The peaks of C 1s at 284.7 eV and 288.3 eV can be assigned to the typical graphitic sp^2 C–C and C–N=C bonds for GCN, respectively.[21] Two oxygenic groups (C-O at 286.2 eV and C=O at 288.7 eV) appear in GCNN:65, which can be attributed to the formation of oxygen functional bridges between $Ni(OH)_2$ nanoplates and GCN. Notably, C–O–Ni band rather than C–Ni–O is formed since the C–Ni bonds at 283.5 eV is absented in the C 1s spectrum.[22] The O 1s peak at 531.7 eV as shown in **Figure 4.9** confirms the presence of the O–Ni bond.[22-23] The present results suggest the formation of chemical bonding between GCN and $Ni(OH)_2$. The N 1 s spectrum (**Figure 4.8c**) shows three peaks at binding energies of 398.5, 399.6 and 400.9 eV, which is corresponding to the graphitic N, pyrrolic N and pyridinic N in GCN, respectively.[12b] In **Figure 4.8d**, besides two satellite peaks, two peaks with binding energies of 855.7 and 873.3 eV can be assigned to Ni $2p_{3/2}$ and Ni $2p_{1/2}$, respectively, and the spin-energy separation of 17.6 eV is the characteristic of Ni^{2+} in $Ni(OH)_2$.[24]

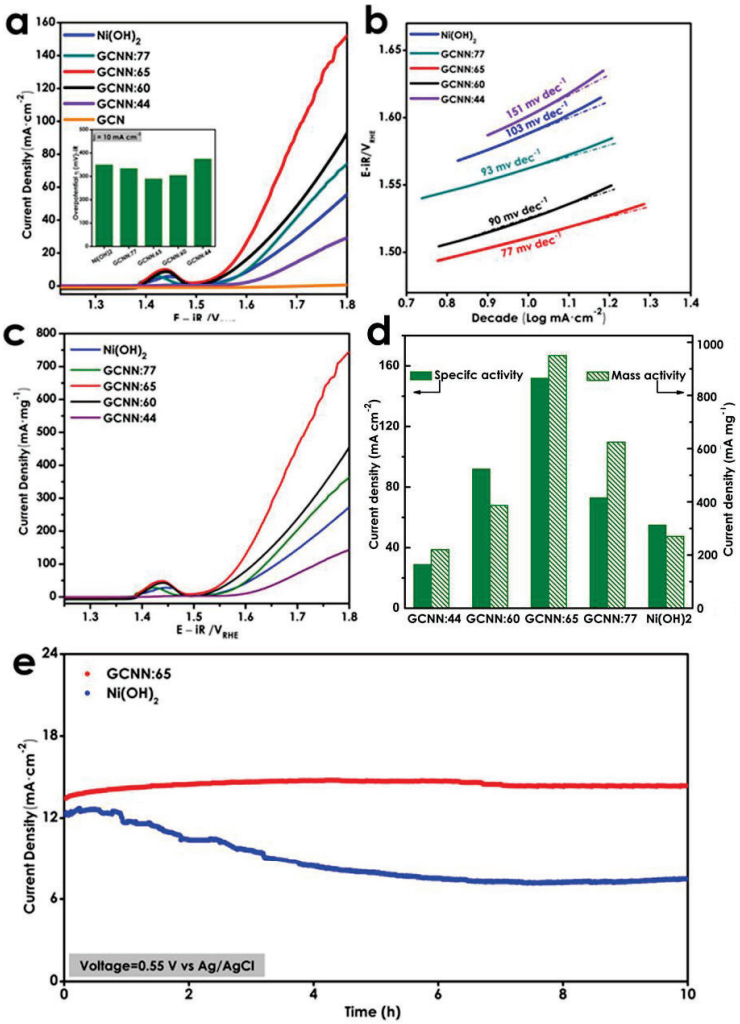

Figure 4.10. (a) LSV polarization curves (with IR-correction) measured at a scan rate of 5 mV s^{-1}. (b) Tafel plots (potential versus log(current density)) derived from LSV curves. (c) LSV curves plotted based on $Ni(OH)_2$ mass-normalized current density. (d) Current densities at 1.8 V vs. RHE. (e) Chronoamperometry at a constant potential of 0.55 V (vs. Ag/AgCl) without IR compensation.

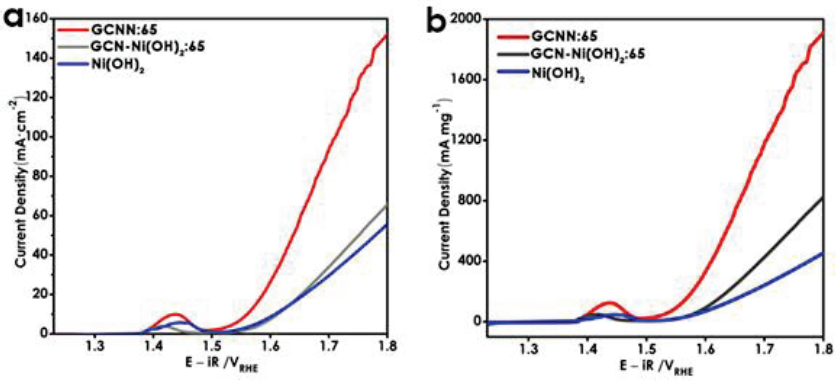

Figure 4.11. (a) LSV curves of GCNN:65, pure $Ni(OH)_2$ and physical mixture GCN-$Ni(OH)_2$:65 (35 wt% GCN) at a scan rate 5 mV s^{-1}. (b) LSV curves based on active $Ni(OH)_2$ mass-normalized current density.

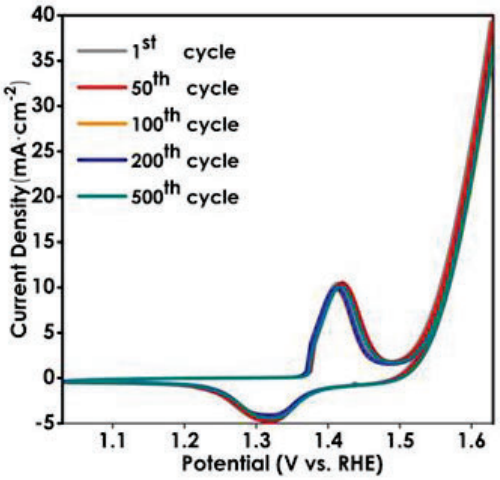

Figure 4.12. CV profiles of GCNN:65 at 10 mV s^{-1} during different cycles.

The electrocatalytic performances of 2D GCNN hybrids together with bare $Ni(OH)_2$ and GCN for OER were investigated under alkaline conditions using a typical three-electrode system. **Figure 4.10a** shows the iR-corrected linear sweep voltammetry (LSV) curves conducted in 1 M KOH aqueous solution at a scan rate of 5 mV s^{-1}. In the polarization curves, the peak located at around 1.43 V versus RHE can be ascribed to the redox reaction of Ni^{2+}/Ni^{3+} in $Ni(OH)_2$.[9] Clearly, GCN is inert to the water oxidation reaction, but the catalytic activity of the $Ni(OH)_2$ is dramatically enhanced by incorporating moderate

GCN nanosheets. The catalytic activity of the GCNN composites varies significantly with altering the content of GCN, and GCNN:65 containing around 35 wt.% GCN delivers the best performance. The GCNN:65 requires the lowest overpotential of 290 mV to achieve a current density of 10 mA cm^{-2}, which is significantly decreased as compared with $Ni(OH)_2$ (350 mV). In order to further evaluate the OER kinetics of the catalysts, Tafel plots are obtained from the polarization curves, as presented in **Figure 4.10b**. The Tafel slope initially decreases with increasing GCN content and reaches the smallest value for GCNN:65, and then increases accordingly. The Tafel slope of GCNN:65 is determined to be 77 mV dec^{-1}, and is much smaller than that of $Ni(OH)_2$ (103 mV dec^{-1}), confirming superior OER kinetics of GCNN:65. In addition, at a potential of 1.8 V (vs. RHE), GCNN:77, GCNN:65, GCNN:60, GCNN:44 and bare $Ni(OH)_2$ delivers 73, 152, 92, 29 and 55 mA cm^{-2}, respectively (**Figure 4.10d**). The performance of GCNN:65 is nearly triple that of $Ni(OH)_2$. In order to clearly distinguish the promotion effect of GCN on the electrocatalytic ability of $Ni(OH)_2$, the LSV curves presenting the mass activity (based on active $Ni(OH)_2$ mass) are plotted, as shown in **Figure 4.10c**. Much more significant performance enhancement can be observed when the performance is compared based on active $Ni(OH)_2$ mass. At the same potential of 1.8 V (vs. RHE), the current density is calculated to be 773, 1900, 1249, 540 and 440 mA mg^{-1} for GCNN:77, GCNN:65, GCNN:60, GCNN:44 and bare $Ni(OH)_2$, respectively (Figure 3d). Impressively, the electrochemical performance of active $Ni(OH)_2$ is increased more than three times after incorporating 35 wt% functionalized GCN. Even for the simply mixed GCN-$Ni(OH)_2$:65 sample (35 wt% GCN), it also exhibits improved catalytic performance over $Ni(OH)_2$, and the current density reaches 65 mA cm^{-2} and 823 mA mg^{-1} at 1.8 V (**Figure 4.11**). The long-term stability of a catalyst is another crucial factor to consider for commercial applications. Continuous chronoamperometry (CA) at a constant potential of 0.55 V (vs. Ag/AgCl) was carried out in 1 M KOH to evaluate the cycling stability of GCNN:65. As shown in Figure 3e, the current density steadily increases over time and retains 102% of the initial current (96% of the peak current density) after 10-h operation. In contrast, the current density of $Ni(OH)_2$ at the same potential decays quickly after 1-h operation and eventually only 65% current density is retained. The CV profiles conducted at 10 mv s^{-1} nearly overlap each other over 500 cycles (**Figure 4.12**), further revealing the good cycle stability of GCNN:65.

Generally, OER in alkaline solution involves migration of hydroxyl groups, oxidation of hydroxyl groups, and oxygen release. Migration and oxidation of hydroxyl groups takes place at solid-liquid (electrode-electrolyte) interface, and oxygen release occurs at solid-gas (electrode-oxygen) interface. Therefore,

developing efficient electrode surface chemistry is of great importance towards enhanced catalytic performances. Basically, the oxidation kinetics of hydroxyl is determined by the intrinsic catalytic activity of the catalyst and the density of the active sites. The efficiency of migration of hydroxyl groups and oxygen release are closely associated with the catalyst wettability. Apparently, for a specific OER catalyst, creating more active sites and engineering superhydrophilic surface are vital to improve the overall electrochemical reaction kinetics. In this work, the GCNN:65 nanocomposite simultaneously has these two key characteristics, and hence delivers substantially improved catalytic performance as compared with bare $Ni(OH)_2$.

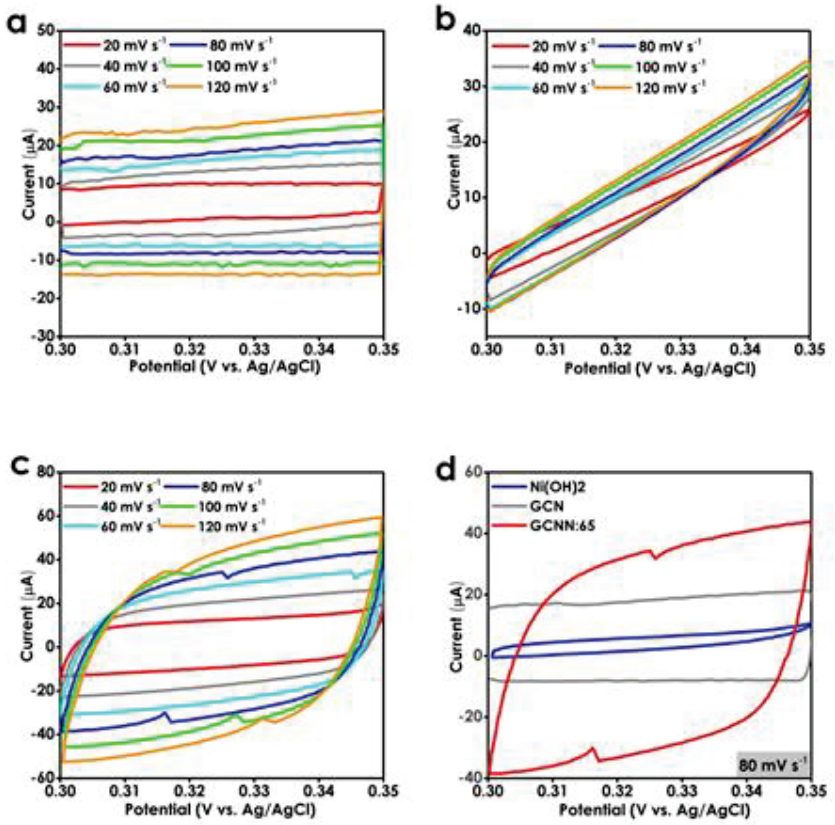

Figure 4.13. CV curves measured in a non-Faradaic region of the voltammogram at scan rates from 20 to 120 mV s^{-1} in 1 M KOH: (a) GCN, (b) pure $Ni(OH)_2$, (c) GCNN:65, and (d) comparison of the CV curves of the three samples measured at a scan rate of 80 mV s^{-1}.

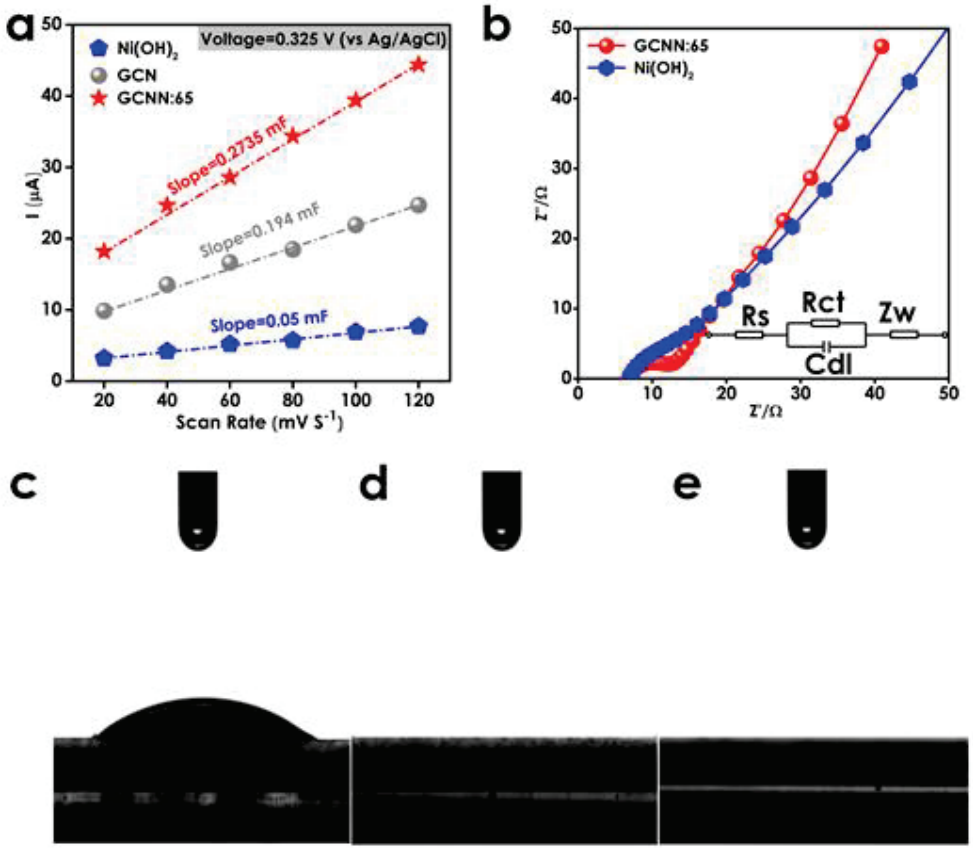

Figure 4.14. (a) The current at 0.325 V (vs. Ag/AgCl) versus scan rate measured in a non-Faradaic range. (b) Electrochemical impedance spectra of GCNN:65 and $Ni(OH)_2$ recorded at 0.6 V (vs. Ag/AgCl) (inset: equivalent circuit model). Contact angle measurements of $Ni(OH)_2$ (c), GCNN:65 (d), and GCNN (e).

Firstly, the incorporation of functionalized GCN effectively prevents $Ni(OH)_2$ from agglomeration, and monodispersed $Ni(OH)_2$ nanoplates are strongly coupled with the ultrathin GCN nanosheets, ensuring the maximum exposure of active sites and high electrochemical active surface areas (ECSA). The ECSA of the catalysts are estimated by determining the double-layer capacitance (C_{DL}) based on CVs measured in a non-Faradaic region (**Figure 4.13a-c**). As shown in **Figure 4.13d**, the GCNN:65 hybrid catalyst shows much higher current than that of bare $Ni(OH)_2$ and GCN. The ECSA of GCNN:65, bare $Ni(OH)_2$ and GCN is calculated to be 6.83, 1.25 and 4.85 cm^2, respectively, based on the C_{DL} values of the catalysts, as present in **Figure 4.14a**. The results suggest that the ECSA of $Ni(OH)_2$ in GCNN:65 nearly doubles that of bare $Ni(OH)_2$ nanoplates, revealing that more accessible active sites are created after introducing GCN, thereby resulting in greatly enhanced catalytic performance.

Figure 4.15. Contact angle measurement of physical mixture GCN-$Ni(OH)_2$:65 (35 wt% GCN).

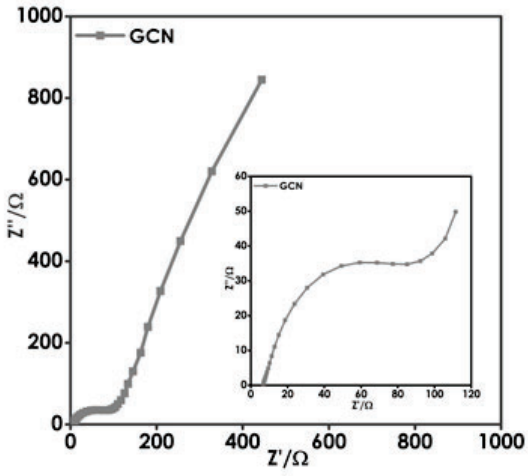

Figure 4.16. Electrochemical impedance spectra of functionalized GCN measured at 0.6 V (vs. Ag/AgCl).

Secondly, the surface wettability of GCNN:65 is greatly improved after combining $Ni(OH)_2$ with GCN, resulting in fast diffusion of hydroxyl ions and desorption of oxygen gas. The static contact angle measurements were performed to investigate the surface wettability of the catalysts. $Ni(OH)_2$ is hydrophilic with a contact angle of 21° (**Figure 4.14c**). As shown in **Figure 4.14d**, the contact angle of GCNN:65 nanocomposite is dramatically decreased to 0° after incorporating functionalized GCN (**Figure 4.14e**), suggesting the formation of a superhydrophilic catalyst surface. The simply mixed GCN-$Ni(OH)_2$:65 sample (35 wt% GCN) also has a superhydrophilic surface (**Figure 4.15**). Considering that $Ni(OH)_2$ in GCN-$Ni(OH)_2$:65 sample shows nearly identical physicochemical properties, in particular the density of active sites, with bare $Ni(OH)_2$, it can be concluded that the enhanced catalytic performance of GCN-$Ni(OH)_2$:65 is induced by the substantially improved wettability. The superhydrophilic surface

would ensure fast electrolyte penetration to the catalyst surface and accelerated diffusion of hydroxyl-based reactants.[10d] In addition, the superhydophilic surface is very beneficial to rapid removal of gas bubbles and to maintain sufficient electrode working area.[10b] All the unique functionalities are of great significance to deliver enhanced electrocatalytic performance. Furthermore, as can be seen from the electrochemical impedance spectra (**Figure 4.14b**), the charge transfer (R_{ct}) resistance of GCNN:65 is around 5.3 Ω, and it is much smaller than that of $Ni(OH)_2$ (17.6 Ω) and GCN (up to 143.2 Ω) (**Figure 4.16**), revealing accelerated charge transfer and surface reaction kinetics at the GCNN:65 electrode/electrolyte interface. The enhanced reaction kinetics of GCNN:65 can be attributed to the synergistic effect of the significantly improved wettability and monodispersed $Ni(OH)_2$ nanoplates with substantial exposure of active sites.

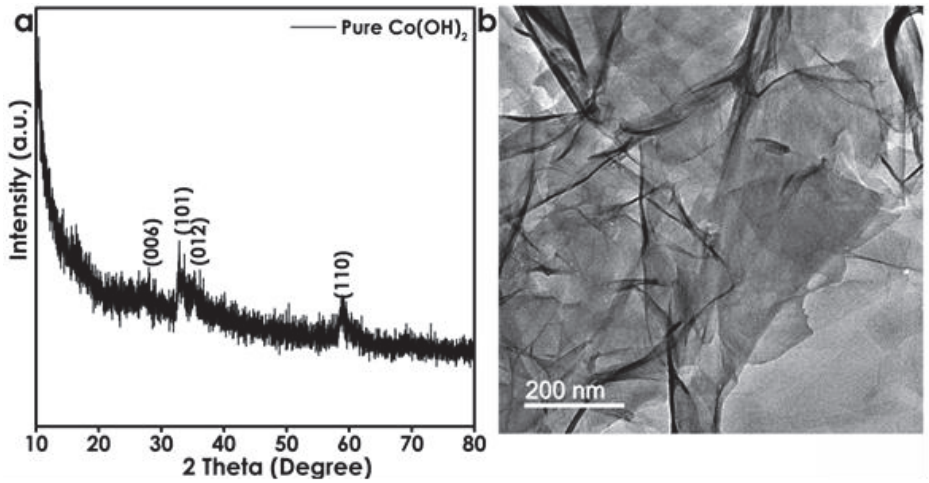

Figure 4.17. (a) XRD and (b) TEM of $Co(OH)_2$ nanosheets. All characteristic peaks are in accordance with the standard card of hexagonal layered α-$Co(OH)_2$ (JCPDS NO. 51-7131). From the TEM image, we can see that the α-$Co(OH)_2$ possesses flexible ultrathin nanosheet morphology.

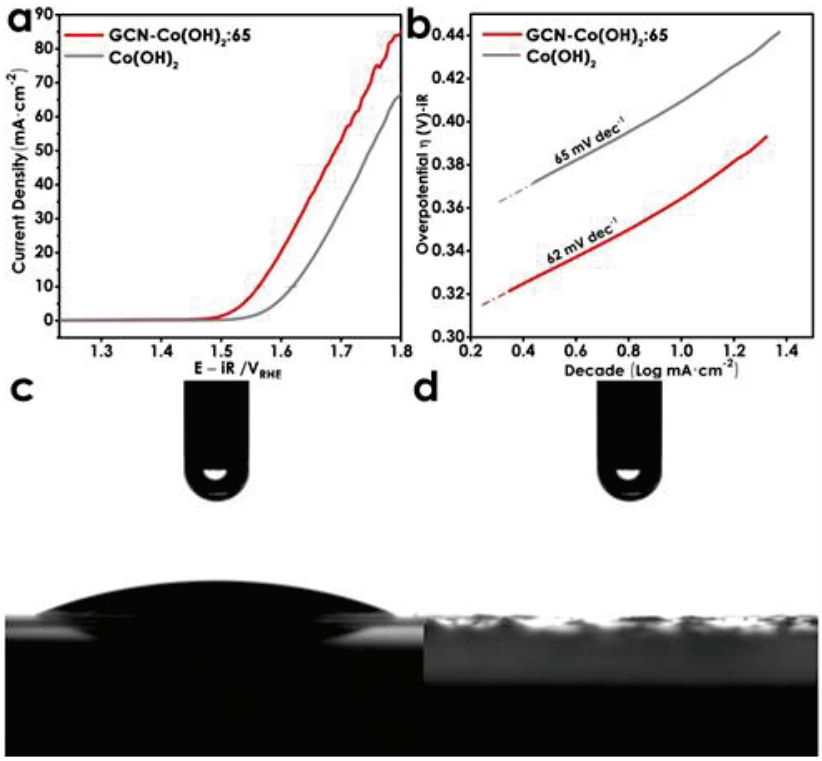

Figure 4.18. (a) LSV curves and (b) Tafel curves of pure $Co(OH)_2$ and physical mixture GCN-$Co(OH)_2$:65 (35 wt% GCN) at a scan rate of 5 mV s^{-1} in 1 M KOH. Contact angle measurements of (c) pure $Co(OH)_2$ and (d) physical mixture GCN-$Co(OH)_2$:65 (35 wt% GCN).

Similar performance promotion resulting from the wettability improvement induced by the incorporation of hydrophilic functionalized GCN is also successfully demonstrated on $Co(OH)_2$. Pure $Co(OH)_2$ nanosheets (**Figure 4.17**) and simply mixed GCN-$Co(OH)_2$:65 sample (35 wt% GCN) were prepared and the corresponding OER performances were evaluated in 1 M KOH. As shown in **Figure 4.18a and b**, the GCN-$Co(OH)_2$:65 sample exhibits lower overpotential and Tafel slope (332 mV at 10 mA cm^{-2}, 62 mV dec^{-1}) than that of bare $Co(OH)_2$ (388 mV at 10 mA cm^{-2}, 65 mV dec^{-1}), clearly demonstrating improved catalytic performance after incorporating GCN. Obviously, although GCN-$Co(OH)_2$:65 contains less active material, it shows higher current density than bare $Co(OH)_2$ under same operating potentials. Notably, the GCN/$Co(OH)_2$ hybrid will no doubt deliver more exceptional performance if similar well-defined structure like GCNN:65 is prepared. As compared with bare $Co(OH)_2$ (contact angle 22°), the contact angle of GCN-$Co(OH)_2$:65 is 0°, revealing a superhydrophilic surface (**Figure 4.18c and d**). Therefore, it can be concluded that introducing hydrophilic functionalized GCN can significantly promote water oxidation catalysis by delivering a superhydrophilic catalyst surface.

4.4. Conclusion

In summary, we reported that electrochemically inert functionalized GCN can substantially promote water oxidation catalysis by improving the wettability and active site exposure of the catalysts. As a proof-of-concept demonstration, superhydrophilic GCNN hybrid nanosheets were synthesized towards efficient water oxidation catalysis. In addition to the superhydrophilic catalyst surface, plenty of monodispersed $Ni(OH)_2$ nanoplates were strongly coupled with GCN, ensuring the maximum exposure of active sites. Consequently, the GCNN hybrid with moderate GCN content exhibited significantly enhanced electrocatalytic performance as compared with bare $Ni(OH)_2$ nanosheets. Similar performance enhancement was also successfully demonstrated on $Co(OH)_2$ after integrating with superhydrophilic GCN. This work opens a new avenue for the development of highly efficient catalysts for electrochemical reactions taking place in aqueous and non-aqueous medium.

4.5. References

[1] G. Wu, K. L. More, C. M. Johnston, P. Zelenay, *Science* **2011**, 332, 443.

[2] a) M. Zhou, H. L. Wang, S. Guo, *Chem Soc Rev* **2016**, 45, 1273; b) J. Fu, F. M. Hassan, C. Zhong, J. Lu, H. Liu, A. Yu, Z. Chen, *Adv. Mater.* **2017**, 29, 1702526.

[3] Q. Kang, L. Vernisse, R. C. Remsing, A. C. Thenuwara, S. L. Shumlas, I. G. McKendry, M. L. Klein, E. Borguet, M. J. Zdilla, D. R. Strongin, *J. Am. Chem. Soc.* **2017**, DOI: 10.1021/jacs.6b09184.

[4] a) M. E. G. Lyons, L. D. Burke, *J. Chem. Soc., Faraday Trans. 1* **1987**, 83, 299; b) S. Ardizzone, G. Fregonara, S. Trasatti, *Electrochimica Acta* **1990**, 35, 263; c) C. C. McCrory, S. Jung, J. C. Peters, T. F. Jaramillo, *J. Am. Chem. Soc.* **2013**, 135, 16977.

[5] a) N. T. Suen, S. F. Hung, Q. Quan, N. Zhang, Y. J. Xu, H. M. Chen, *Chem Soc Rev.* **2017**, 46, 337; b) X.-F. Lu, P.-Q. Liao, J.-W. Wang, J.-X. Wu, X.-W. Chen, C.-T. He, J.-P. Zhang, G.-R. Li, X.-M. Chen, *J. Am. Chem. Soc.* **2016**, 138, 8336.

[6] a) J. Suntivich, K. J. May, H. A. Gasteiger, J. B. Goodenough, Y. Shao-Horn, *Science* **2011**, 334, 1383; b) F. Cheng, J. Shen, B. Peng, Y. Pan, Z. Tao, J. Chen, *Nat Chem.* **2011**, 3, 79; c) K. L. Nardi, N. Yang, C. F. Dickens, A. L. Strickler, S. F. Bent, *Adv. Energy Mater.* **2015**, 5, 1500412; d) M. S. Burke, L. J. Enman, A. S. Batchellor, S. Zou, S. W. Boettcher, *Chem. Mater.* **2015**, 27, 7549; e) Y. Zhu, W. Zhou, J. Sunarso, Y. Zhong, Z. Shao, *Adv. Funct. Mater.* **2016**, 26, 5862; f) L. Xu, Q. Jiang, Z. Xiao, X. Li, J. Huo, S. Wang, L. Dai, *Angew. Chem. Int. Ed.* **2016**, 55, 5277.

[7] a) R. Subbaraman, D. Tripkovic, K. C. Chang, D. Strmcnik, A. P. Paulikas, P. Hirunsit, M. Chan, J. Greeley, V. Stamenkovic, N. M. Markovic, *Nat Mater.* **2012**, 11, 550; b) M. Gong, Y. Li, H. Wang, Y.

Liang, J. Z. Wu, J. Zhou, J. Wang, T. Regier, F. Wei, H. Dai, *J. Am. Chem. Soc.* **2013**, 135, 8452; c) F. Song, X. Hu, *Nat. Commun.* **2014**, 5, 4477; d) L. Chen, X. Dong, Y. Wang, Y. Xia, *Nat. Commun.* **2016**, 7, 11741; e) J. Ping, Y. Wang, Q. Lu, B. Chen, J. Chen, Y. Huang, Q. Ma, C. Tan, J. Yang, X. Cao, Z. Wang, J. Wu, Y. Ying, H. Zhang, *Adv. Mater.* **2016**, 28, 7640; f) H. Jin, S. Mao, G. Zhan, F. Xu, X. Bao, Y. Wang, *J. Mater. Chem. A* **2017**, 5, 1078; g) J.-X. Feng, H. Xu, Y.-T. Dong, S.-H. Ye, Y.-X. Tong, G.-R. Li, *Angew. Chem. Int. Ed.* **2016**, 55, 3694; h) J.-X. Feng, S.-H. Ye, H. Xu, Y.-X. Tong, G.-R. Li, *Adv. Mater.* **2016**, 28, 4698.

[8] a) H. B. Yang, J. Miao, S. F. Hung, J. Chen, H. B. Tao, X. Wang, L. Zhang, R. Chen, J. Gao, H. M. Chen, L. Dai, B. Liu, *Sci. Adv.* **2016**, 2, e1501122; b) Z. Wang, Y. Lu, Y. Yan, T. Y. P. Larissa, X. Zhang, D. Wuu, H. Zhang, Y. Yang, X. Wang, *Nano Energy* **2016**, 30, 368; c) C. Hu, L. Dai, *Adv. Mater.* **2017**, 29.

[9] X. Long, J. Li, S. Xiao, K. Yan, Z. Wang, H. Chen, S. Yang, *Angew. Chem. Int. Ed.* **2014**, 126, 7714.

[10] a) A. Bhaumik, P. Mukherjee, R. Kumar, *J. Catal.* **1998**, 178, 101; b) Z. Lu, W. Zhu, X. Yu, H. Zhang, Y. Li, X. Sun, X. Wang, H. Wang, J. Wang, J. Luo, X. Lei, L. Jiang, *Adv. Mater.* **2014**, 26, 2683; c) C. Ling, Y. Huang, H. Liu, S. Wang, Z. Fang, L. Ning, *J. Phys. Chem. C* **2014**, 118, 28291; d) Y. Li, C. Zhao, *ACS Catal.* **2017**, DOI: 10.1021/acscatal.6b034972535.

[11] K. S. Lakhi, D. H. Park, K. Al-Bahily, W. Cha, B. Viswanathan, J. H. Choy, A. Vinu, *Chem Soc Rev* **2017**, 46, 72.

[12] a) T. Y. Ma, S. Dai, M. Jaroniec, S. Z. Qiao, *Angew. Chem. Int. Ed.* **2014**, 53, 7281; b) J. Duan, S. Chen, M. Jaroniec, S. Z. Qiao, *ACS Nano* **2015**, 9, 931.

[13] T. Y. Ma, Y. Tang, S. Dai, S. Z. Qiao, *Small* **2014**, 10, 2382.

[14] Y. Wang, X. Wang, M. Antonietti, *Angew. Chem. Int. Ed.* **2012**, 51, 68.

[15] a) Y. Zhang, A. Thomas, M. Antonietti, X. Wang, *J. Am. Chem. Soc.* **2009**, 131, 50; b) J. H. Lee, M. J. Park, S. J. Yoo, J. H. Jang, H. J. Kim, S. W. Nam, C. W. Yoon, J. Y. Kim, *Nanoscale* **2015**, 7, 10334; c) X. Du, G. Zou, Z. Wang, X. Wang, *Nanoscale* **2015**, 7, 8701.

[16] J. Yan, Z. Fan, W. Sun, G. Ning, T. Wei, Q. Zhang, R. Zhang, L. Zhi, F. Wei, *Adv. Funct. Mater.* **2012**, 22, 2632.

[17] L. Xu, Y.-S. Ding, C.-H. Chen, L. Zhao, C. Rimkus, R. Joesten, S. L. Suib, *Chem. Mater.* **2008**, 20, 308.

[18] B. Mavis, M. Akinc, *Chem. Mater.* **2006**, 18, 5317.

[19] S. Yang, Y. Gong, J. Zhang, L. Zhan, L. Ma, Z. Fang, R. Vajtai, X. Wang, P. M. Ajayan, *Adv. Mater.* **2013**, 25, 2452.

[20] L. Li, J. Qin, H. Bi, S. Gai, F. He, P. Gao, Y. Dai, X. Zhang, D. Yang, P. Yang, *Sci. Rep.* **2017**, 7, 43413.

[21] L. Ma, H. Fan, K. Fu, S. Lei, Q. Hu, H. Huang, G. He, *ACS Sustainable Chem. Eng.* **2017**, DOI: 10.1021/acssuschemeng.7b01312.

[22] M. Jing, C. Wang, H. Hou, Z. Wu, Y. Zhu, Y. Yang, X. Jia, Y. Zhang, X. Ji, *J. Power Sources* **2015**, 298, 241.

[23] W. Liu, C. Lu, X. Wang, K. Liang, B. K. Tay, *J. Mater. Chem. A* **2015**, 3, 624.

[24] B. Dong, M. Li, S. Chen, D. Ding, W. Wei, G. Gao, S. Ding, ACS Appl. Mater. Interfaces **2017**, DOI: 10.1021/acsami.7b02693.

Note: The content of this chapter has been published in **Advanced Functional Materials.** Permission regarding copyright has been obtained from the publishers. [Yaping Chen, Qian Zhou, Guoqiang Zhao, Zhenwei Yu, Xiaolin Wang, Shi Xue Dou, Wenping Sun,* Electrochemically Inert g‐C_3N_4 Promotes Water Oxidation Catalysis. **Adv. Funct. Mater. 2018, 28, 1705583**.]

Chapter 5

5. Electrocatalytically Inactive SnS_2 Promotes Water Adsorption/Dissociation on Molybdenum Dichalcogenides for Accelerated Alkaline Hydrogen Evolution

5.1 Introduction

Our severe energy and environmental crisis makes it imperative to search for clean and sustainable energy sources as alternatives to traditional fossil fuels.[1-3] Owing to its having the highest gravimetric energy density and carbon-free emissions, hydrogen produced by renewable energy sources is considered to be the most promising energy carrier for our future society's energy.[4-5] Currently, hydrogen is mostly produced from fossil fuels by steam reforming.[6] Alternatively, photocatalytic, photoelectrocatalytic, or electrocatalytic water splitting driven by renewable energy would make hydrogen a real carrier for clean energy.[7-9] With regards to electrocatalytic water splitting, electrocatalytic performance remains unsatisfactory for both the cathodic hydrogen evolution reaction (HER) and the anodic oxygen evolution reaction (OER), although numerous research efforts have been devoted to developing efficient electrocatalysts. Currently, precious metal-based materials are the state-of-the-art catalysts for both the HER (e.g., Pt) and the OER (e.g., IrO_2), but they suffer from high cost and scarcity.[10-17] Therefore, developing earth-abundant and low-cost alternatives, such as transition metal chalcogenides, metal oxides/hydroxides, and metal alloys, is critically necessary to address this challenge for practical water splitting systems.[18-21]

Molybdenum dichalcogenides, in particular MoS_2 and $MoSe_2$, are very promising nonprecious-metal-based electrocatalysts for the HER.[22-24] Both density functional theory (DFT) calculations and experimental findings have demonstrated that the HER catalytic activity of molybdenum dichalcogenides is mainly derived from their edge sites.[25-29] In this regards, various strategies have been focused on increasing the number of exposed active sites of molybdenum-dichalcogenide-based electrocatalysts through building various nanostructures, engineering surface defects, or heteroatom doping.[30-32] Unfortunately, although the molybdenum dichalcogenide-based electrocatalysts thus developed display impressive catalytic activity in acidic media, they exhibit inferior HER activity in alkaline media due to the sluggish water dissociation kinetics. Basically, alkaline HER involves water adsorption, water

dissociation, and hydrogen recombination and release.[33] Water adsorption and dissociation take place at the beginning of the alkaline HER process and are considered to represent the rate-determining step for the alkaline HER.[34-37] Therefore, designing electrocatalysts with enhanced water adsorption and dissociation capability is the key for the promotion of alkaline HER catalytic activity. Recently, molybdenum-dichalcogenide-based heterostructures with an additional phase (e.g., $Ni(OH)_2$) anchored on MoS_2 or $MoSe_2$ nanosheets were reported as efficient alkaline HER catalysts.[38-40] The second phases usually possess strong water affinity and water adsorption capability, which are of great significance for accelerating the water dissociation kinetics of the heterostructured catalysts.[41] Meanwhile, in some cases, the presence of the second phase can also modulate the electronic structure of Mo and optimize the hydrogen adsorption energy.[42-44] On the other hand, heteroatom doping (e.g., Ni, Co) was also demonstrated to be an effective strategy for enhancing alkaline HER kinetics.[45-46]

In this work, we propose a new heterostructured design concept in order to improve the alkaline HER activity of molybdenum dichalcogenides. $MoSe_2/SnS_2$ and MoS_2/SnS_2 heterostructures with SnS_2 quantum dots decorated on the basal planes are synthesized by a universal wet-chemical strategy for enhanced alkaline HER. DFT calculations reveal that the incorporation of SnS_2 brings in the substantial enhancement of water adsorption capability of $MoSe_2$ both on the edge sites and basal planes. Benefiting from the improved water adsorption/dissociation capability, the well-defined heterostructures delivered significantly enhanced hydrogen evolution kinetics in alkaline media.

5.2. Experimental Section

5.2.1. Materials

All the chemicals were purchased from Sigma-Aldrich (A.R) and were used as received without further purification.

5.2.2. Materials Preparation

5.2.2.1. Synthesis of $MoSe_2$ Nanosheets

$MoSe_2$ nanosheets were synthesized by a modified hydrothermal process.[32] Briefly, 241.95 mg $Na_2MoO_4{\cdot}2H_2O$ was added to 20 ml deionized water (DI water) under magnetic stirring as the Mo precursor. Then, 0.1 g $NaBH_4$ was dissolved in 15 ml Ar saturated DI water in a three-neck bottle. Subsequently, 0.16 g Se powders were dispersed into the $NaBH_4$ aqueous solution under Ar flow with mild shaking until Se powders were fully dissolved to form a homogeneous transparent NaHSe solution, which was used as the Se source. Next, the Mo and Se source solutions were transferred into a 50 ml

Teflon-lined stainless steel autoclave, purged with Ar for 30 min, and then heated in an oven at 180 °C for 24 h. After cooling down to room temperature, the as-prepared product was collected by centrifugation, washed with DI water and ethanol for several times, and dried at 60 °C under vacuum overnight.

5.2.2.2. Synthesis of $MoSe_2/SnS_2$ Heterostructures

For the preparation of $MoSe_2/SnS_2$-2.5, 7.12 mg $SnCl_4 \cdot 5H_2O$ and 6 mg thioacetamide (TAA) were added together into the as-obtained $MoSe_2$ dispersion solution (0.36 mg ml^{-1} in the mixture of 15 ml DI water and 20 ml ethylene glycol). After 1 h sonication, the mixed solution was transferred into a 50 ml Teflon-lined stainless steel autoclave and heated in an electric oven at 180 °C for 24 h. After cooling down to room temperature, the obtained $MoSe_2/SnS_2$-2.5 was collected by centrifugation at 8000 rpm for 5 min, then repeatedly washed with DI water and ethanol, and finally dried at 60 °C under vacuum overnight. $MoSe_2/SnS_2$-*x* (*x* = 1.5, 5.0, 10) was prepared following the same procedure as for $MoSe_2/SnS_2$-2.5 with different molar ratios of Mo and Sn precursors (Mo/Sn = 1.5, 5.0, and 10). The Mo/Sn atomic ratios in the $MoSe_2/SnS_2$ heterostructures ($MoSe_2/SnS_2$-1.5: Mo/Sn = 3.5; $MoSe_2/SnS_2$-2.5: Mo/Sn = 4.7; $MoSe_2/SnS_2$-5.0: Mo/Sn = 7.0; $MoSe_2/SnS_2$-10: Mo/Sn = 12.6) were determined using inductively coupled plasma – optical emission spectrometry (ICP-OES, Perkin-Elmer, Optima 7300DV) with mass spectrometry.

5.2.2.3. Synthesis of MoS_2/SnS_2 Heterostructures

For the preparation of pure MoS_2, 72.6 mg Na_2MoO_4 $2H_2O$ and 45.7 mg thiourea were firstly added into DI water (35 ml) under sonication for 10 mins. Then, the homogeneous solution was transferred into a 50 mL autoclave for hydrothermal reaction at 180 °C for 24 h. After cooling down to room temperature, the as-prepared MoS_2 was collected by centrifugation, washed with DI water and ethanol several times, and dried at 60 °C under vacuum overnight. For the preparation of MoS_2/SnS_2-2.5, 7.12 mg $SnCl_4 \cdot 5H_2O$ and 6 mg TAA were added together into the as-obtained MoS_2 dispersion solution (0.232 mg ml^{-1} in the mixture of 15 ml DI water and 20 ml ethylene glycol). After 1 h sonication, the mixed solution was transferred into the 50 ml Teflon-lined stainless steel autoclave and heated in an electric oven at 180 °C for 24 h. Finally, the MoS_2/SnS_2-2.5 product was collected after centrifugation, washing, and drying. MoS_2/SnS_2-*x* (*x* = 1.5 and 5.0) was prepared following the same procedure as for MoS_2/SnS_2-2.5 with different molar ratios of Mo and Sn precursors (Mo/Sn = 1.5 and 5.0).

5.2.3. Physical Characterization

X-ray diffraction (XRD) was carried out using a GBC MMA X-ray diffractometer (λ = 1.5406 Å, 25mA, 40 Kv, step size of 0.02° s^{-1}). The morphology and microstructures of the samples were characterized by

transmission electron microscopy (TEM, JEM-2010, working voltage 200 kV). The scanning transmission electron microscopy (STEM) elemental mappings were conducted on the JEOL ARM-200F at 200 kV equipped with an EDS detector. X-ray photoelectron spectroscopy (XPS) measurements were performed on a Thermo ESCALAB 250Xi instrument with monochrome Al Kα ($h\nu$ =1486.6 eV) as the X-ray excitation source. The Mo/Sn atomic ratios in the $MoSe_2/SnS_2$ heterostructures were obtained by ICP-OES.

5.2.4. Electrochemical Measurement

All the electrochemical measurements were performed with a typical three-electrode electrochemical cell equipped with the rotating disk electrode (Pine Research Instruments, Inc.) and electrochemical workstation (Multichannel potentiostat/galvanostat VSP-300, BioLogic Science Instrument). Hg/HgO (1 M KOH solution) and Ag/AgCl (saturated KCl solution) were used as the reference electrode in 1 M KOH and 0.5 M H_2SO_4 aqueous solution, respectively. The platinum wire was employed as the counter electrode, and the glassy carbon electrode (0.196 cm^2) coated with different catalyst inks was used as the working electrode. The catalyst inks were prepared as follows. 2 mg catalyst was dispersed into a mixed solvent composed of 16 μL Nafion solution (Aldrich Co., 5 wt%), 384 μL deionized water, and 100 μL isopropanol under sonication for 30 min. 10 μL of catalyst ink (containing 40 μg of catalyst) was coated onto the polished glassy carbon electrode and dried at room temperature. The electrolyte was continuously purged with N_2 to remove O_2 during the measurements. The working electrode was constantly rotated at 1600 rpm to remove the generated H_2 and eliminate concentration polarization of electrolyte ions during electrochemical testing. Linear sweep voltammetry (LSV) polarization curves were collected at a scan rate of 5 mV s^{-1}. All LSV curves were corrected with 95% *iR*-compensation. Electrochemical impedance spectra (EIS) were collected at -0.1 V (vs. RHE) in the frequency range of 1.0 −100 kHz.

The electrochemical active surface area (ECSA) was evaluated by calculating the double-layer capacitance (C_{dl}) in 1 M KOH.[47] The cyclic voltammetry (CV) curves were performed at scan rates from 40 to 140 mV s^{-1} in the range of -100 – 0 mV vs. RHE. The C_{dl} values were calculated according to the equation:

$$j = \nu C_{dl} \quad (5.1)$$

Where the capacitive current j (A) can be obtained by $\frac{J_a - J_c}{2}$. J_a and J_c represent anodic current and cathodic current at -50 mV vs. RHE, respectively, and ν (mV s^{-1}) is the scan rate.

The turnover frequency (TOF) was calculated according to the following equation:

$$TOF = \frac{\text{Total number of } H_2 \text{ molecules per second}}{\text{Total number of active sites per unit area}} = \frac{\frac{j}{2\times q}}{\text{N}} \quad (5.2)$$

Where q = 1.6 × 10^{-19} C stands for the elementary charge, j represents current (A) from the linear sweep measurement, N stands for the number of total Mo atoms, and 2 represents that two electrons are required to generate one H_2 molecule.

5.2.5. Computational Methods

All DFT calculations were performed using the plane-wave pseudopotential method with the CASTEP[55] module in the Materials Studio software package.[56] We adopted the Perdew−Burke−Ernzerhof (PBE) exchange–correlation functional[57] corrected by the semi-empirical Grimme scheme (PBE-D)[58], ultrasoft pseudopotentials[59], and an energy cut-off of 300 eV. The convergence criteria of energy and forces for geometry optimization were 2 × 10^{-5} eV and 0.05 eV/Å, respectively. The Brillouin zone was sampled with a Monkhorst−Pack[60] grid of 4 × 4 × 1 k-points. All calculations were non-spin-polarized. The (002) planes of bulk $MoSe_2$ and SnS_2 were adopted to model the $MoSe_2$ and SnS_2 nanosheets, respectively. Two-dimensional rhombic periodic boundary conditions and slab models were applied. The vacuum layer (> 30 Å) was added to avoid interaction between adjacent images. The surface models and cell parameters are shown in Figures S7-S8 and Table S1, respectively.

Table 5.1. Cell parameters (*a*, *b*, *c* in Å; *α*, *β*, *γ* in º) for the studied systems.

	a	*b*	*c*	*α*	*β*	*γ*
$MoSe_2$ basal plane	19.96	19.96	36.07	90	90	120
SnS_2 basal plane	21.83	21.83	35.94	90	90	120
$MoSe_2$ edge	19.96	46.00	23.07	90	90	120
SnS_2 edge	21.83	43.66	22.94	90	90	120
$MoSe_2$/SnS_2 edge	19.96	46.00	23.07	90	90	120

5.3. Results and Discussion

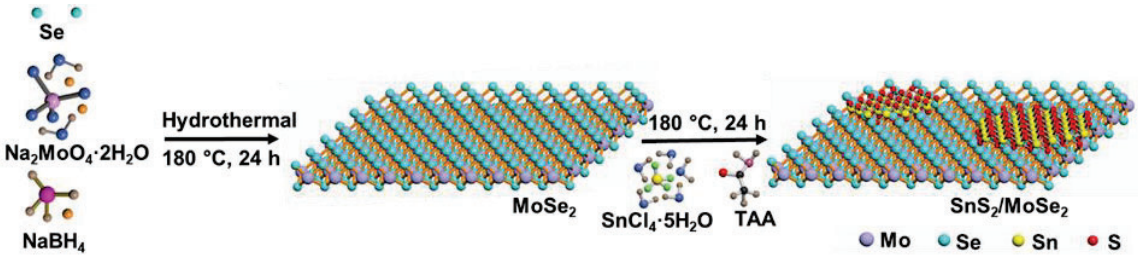

Figure 5.1. Illustration of the synthesis of $MoSe_2/SnS_2$ heterostructures.

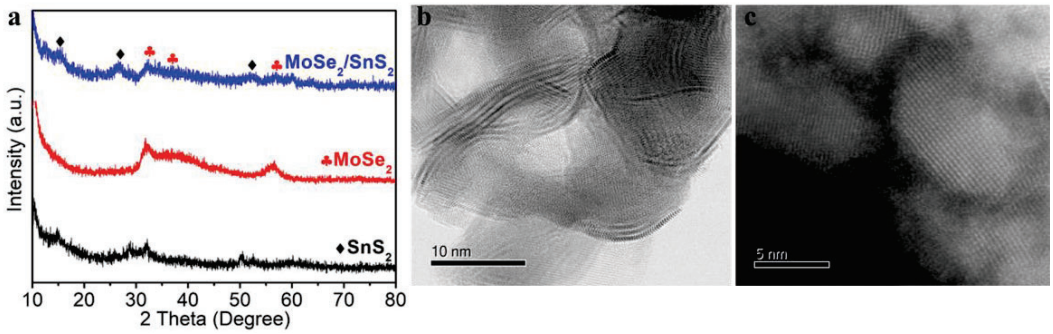

Figure 5.2. (a) XRD patterns of pure $MoSe_2$, pure SnS_2, and $MoSe_2/SnS_2$. TEM images of (b) pure MoSe2 and (c) MSSS-2.5 composite.

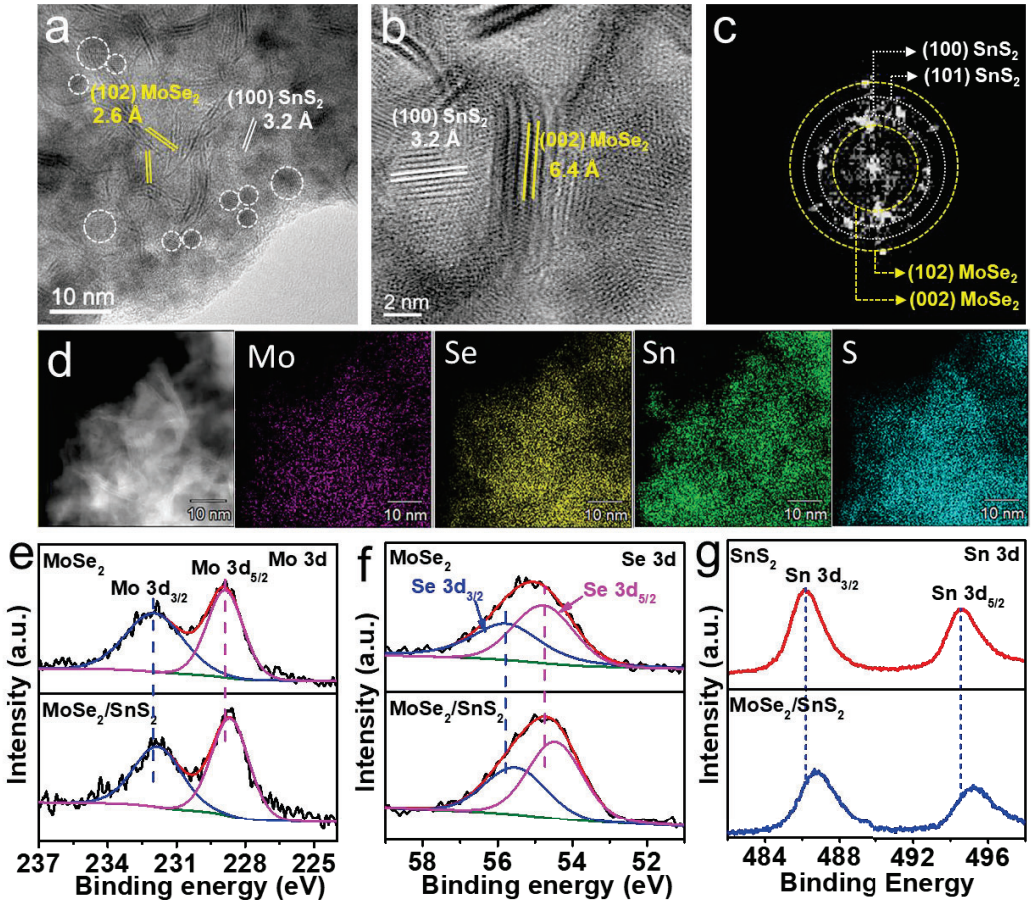

Figure 5.3. (a, b) TEM images and (c) the corresponding FFT pattern of $MoSe_2/SnS_2$-2.5 heterostructure; (d) STEM-EDS elemental mapping of Mo, Se, Sn, and S; XPS spectra of (e) Mo 3d, (f) Se 3d, and (g) Sn 3d.

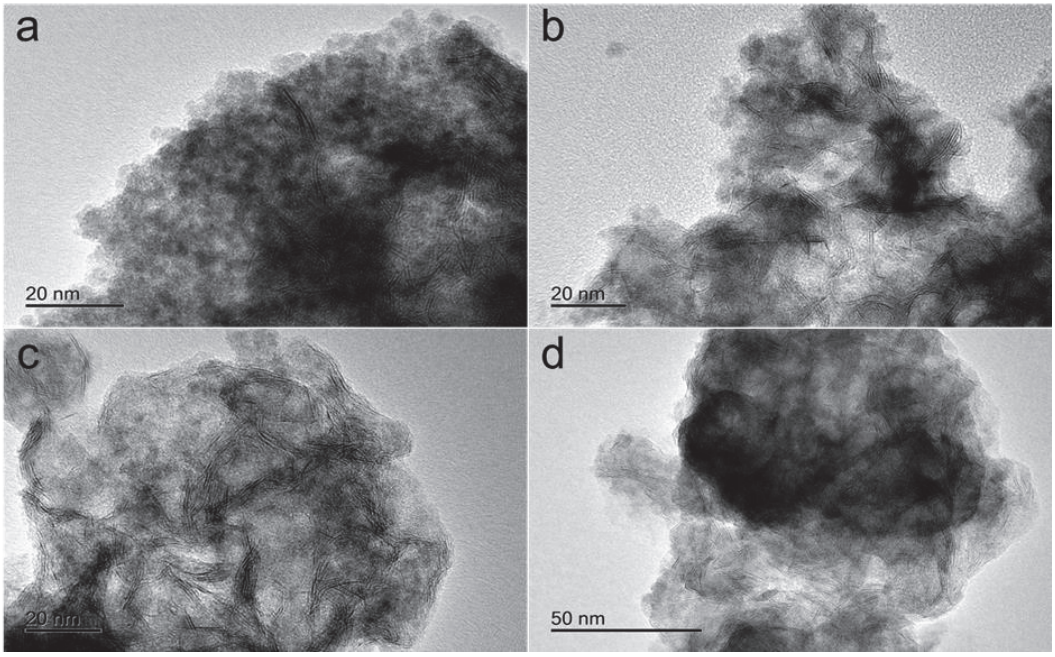

Figure 5.4. TEM images of $MoSe_2/SnS_2$-1.5 (a), $MoSe_2/SnS_2$-2.5 (b), $MoSe_2/SnS_2$-5.0 (c), and $MoSe_2/SnS_2$-10 (d).

The molybdenum dichalcogenide heterostructures were prepared via a two-step hydrothermal method, as illustrated in **Figure 5.1**. The molybdenum dichalcogenide nanosheets were first prepared, and then SnS_2 quantum dots were uniformly anchored on the nanosheet surfaces via an in-situ precipitation process (See Experimental Section for more details). The X-ray diffraction (XRD) pattern of $MoSe_2/SnS_2$ (**Figure 5.2a**) presents typical diffraction peaks that can be well indexed to SnS_2 (JCPDS No. 23-0667) and $MoSe_2$ (JCPDS No. 29-0914). **Figure 5.2b, 5.2c, and 5.3a** shows the transmission electron microscopy (TEM) analysis, SnS_2 quantum dots with a size of 3-5 nm were uniformly grown on the surfaces of $MoSe_2$ nanosheets, which could reduce agglomeration. Also, the typical lattice spacings of 0.32 and 0.26 nm could be indexed to the (100) planes of SnS_2 and the (102) planes of $MoSe_2$, respectively. In **Figure 5.3b**, the high-resolution transmission electron microscopy (HRTEM) image provides more detailed structural information. It can be shown that the markedly striped patterns are in good agreement with the $MoSe_2$ edge surface of (002) planes, while the SnS_2 quantum dots were aligned along the [001] *c*-axis in intimately contact with the $MoSe_2$ surface. The corresponding Fast Fourier transform (FFT) pattern (**Figure 5.3c**) clearly indicates the co-existence of (102) and (002) planes of $MoSe_2$, and (100) and (101) planes of SnS_2, further revealing the formation of $MoSe_2/SnS_2$ heterostructures. The scanning transmission electron microscopy (STEM) elemental mapping results further reveal the spatial

distribution of Mo, Se, Sn, and S in the $MoSe_2/SnS_2$ heterostructures (**Figure 5.3d**). Moreover, the $MoSe_2/SnS_2$ heterostructures with different Mo/Sn atomic ratios could be precisely controlled by varying the ratio of pthe recursors (**Figure 5.4a-d**).

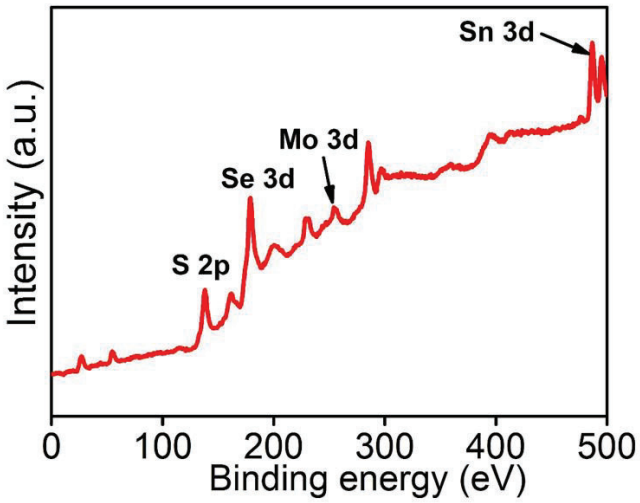

Figure 5.5. XPS survey spectrum of $MoSe_2/SnS_2$-2.5.

The X-ray photoelectron spectroscopy (XPS) survey spectrum of the $MoSe_2/SnS_2$ heterostructures confirmed the coexistence of Mo, Se, Sn, and S elements (**Figure 5.5**). After deposition of the SnS_2, the binding energies of Mo 3d and Se 3d are shifted negatively by 0.2 and 0.3 eV, respectively (**Figure 5.3e-f**). Along with the negative shift in the binding energy, the surface negative charge density of $MoSe_2$ will be increased. As a result, the H atoms of water molecules are more accessible to the negative charges, so that an attractive interaction between water molecules and the surface of $MoSe_2$ is enhanced accordingly.[26, 48] In other words, the negative shift in the binding energy for Mo and Se effectively promotes the adsorption capability of water molecules. Also, the negative shift in the binding energy for $MoSe_2$ demonstrates the transfer of electrons from SnS_2 to $MoSe_2$, which helps to improve the conductivity of $MoSe_2$.[43-44] Moreover, a positive shift of 0.5 eV can be observed for the binding energy of Sn 3d in $MoSe_2/SnS_2$ as compared to SnS_2 (**Figure 5.3g**). These results demonstrate that the charge redistribution across the interfaces of $MoSe_2/SnS_2$ heterostructures is beneficial to increase the water adsorption capability and improve the conductivity of $MoSe_2$.

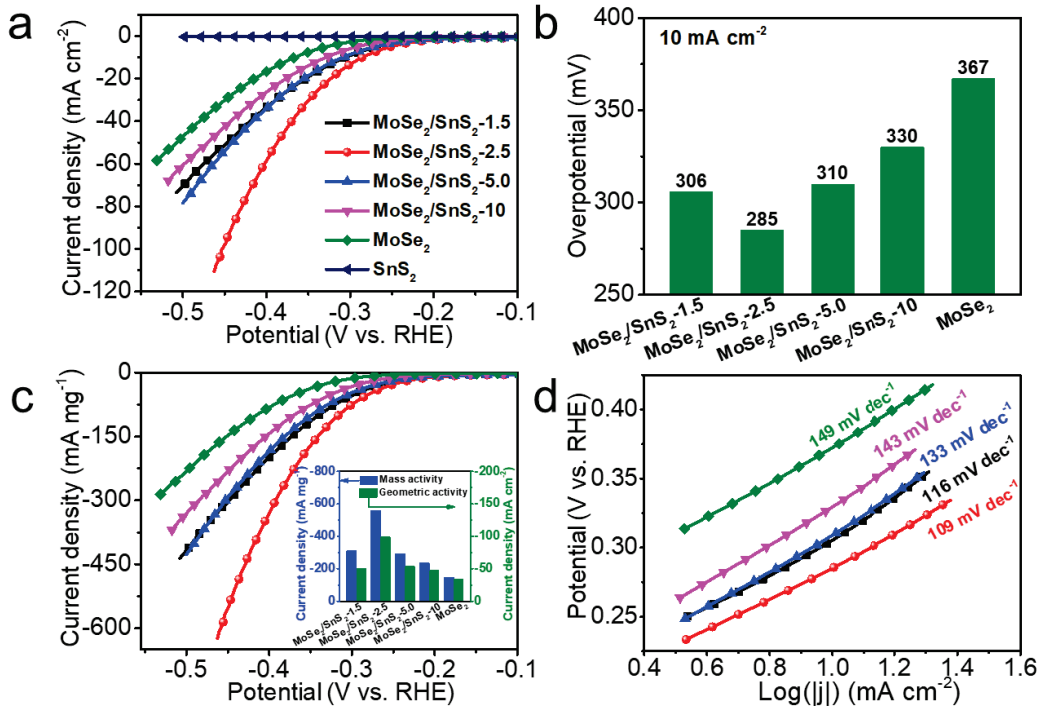

Figure 5.6. (a) LSV polarization curves measured at a scan rate of 5 mV s^{-1}; (b) Overpotential at the current density of 10 mA cm^{-2}; (c) LSV curves plotted based on $MoSe_2$ mass-normalized current density (inset: current densities at -0.45 V (vs. RHE)); (d) Tafel plots (potential vs. log(current density)) derived from LSV curves.

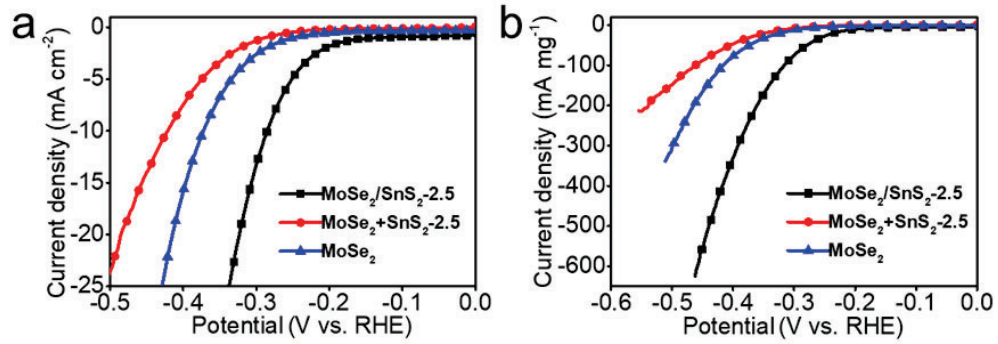

Figure 5.7. (a) LSV curves of $MoSe_2/SnS_2$-2.5, pure $MoSe_2$, and the physical mixture $MoSe_2$+SnS_2-2.5 at a scan rate of 5 mV s^{-1}. (b) LSV curves based on active $MoSe_2$ mass-normalized current density.

The HER activities of the as-prepared $MoSe_2$ and $MoSe_2/SnS_2$ heterostructured catalysts were evaluated in 1 M KOH aqueous electrolyte in a standard three-electrode system. **Figure 5.6a** shows the polarization curves after 95% *iR* correction carried out at a scan rate of 5 mV s^{-1}. For the pure SnS_2, the linear sweep voltammetry (LSV) curve displays a weak current response, demonstrating its electrocatalytic inertness in

alkaline media. The pure $MoSe_2$ needs an overpotential of 367 mV to reach a current density of 10 mA cm^{-2}. Compared to $MoSe_2$, all the $MoSe_2/SnS_2$ heterostructured catalysts show substantially enhanced catalytic activities. Specifically, the $MoSe_2/SnS_2$-2.5 heterostructured catalyst exhibits optimal HER activity and a much lower overpotential of 285 mV at 10 mA cm^{-2} (**Figure 5.6b**). Also, $MoSe_2/SnS_2$-2.5 shows the best mass activity (559 mA mg^{-1}) at 0.45 V among all the catalysts, which is superior to $MoSe_2/SnS_2$-1.5 (309 mA mg^{-1}), $MoSe_2/SnS_2$-5.0 (291 mA mg^{-1}), $MoSe_2/SnS_2$-10 (235 mA mg^{-1}), and pure $MoSe_2$ (147 mA mg^{-1}) (**Figure 5.6c and the inset**). These results indicate that SnS_2 plays a key role in promoting the HER kinetics of $MoSe_2$ in alkaline media. It is worth noting that the physically mixed sample with a molar ratio of $MoSe_2$:SnS_2 = 2.5: 1 ($MoSe_2$+SnS_2-2.5) deliveres decreased geometric and mass activities (14 mA cm^{-2} and 87 mA mg^{-1} at 0.45 V), as compared to $MoSe_2/SnS_2$-2.5 and bare $MoSe_2$ (**Figure 5.7**), revealing that the unique heterostructure morphology and interaction between $MoSe_2$ and SnS_2 are of great importance to the accelerated alkaline HER kinetics. Tafel slopes give further insights into the HER kinetics. As shown in **Figure 5.6d**, pure $MoSe_2$ shows a Tafel slope of 149 mV dec^{-1}, indicating that the kinetic rate-limiting step is the Volmer step, in which step water molecules dissociate into hydrogen intermediates and hydroxyls. Compared to $MoSe_2$, the Tafel slope of $MoSe_2/SnS_2$-2.5 is reduced to 109 mV dec^{-1}, demonstrating that the HER kinetics are determined by the Volmer step and subsequent Heyrovsky step. The enhanced kinetics can be attributed to the accelerated water dissociation process (Volmer step).[45]

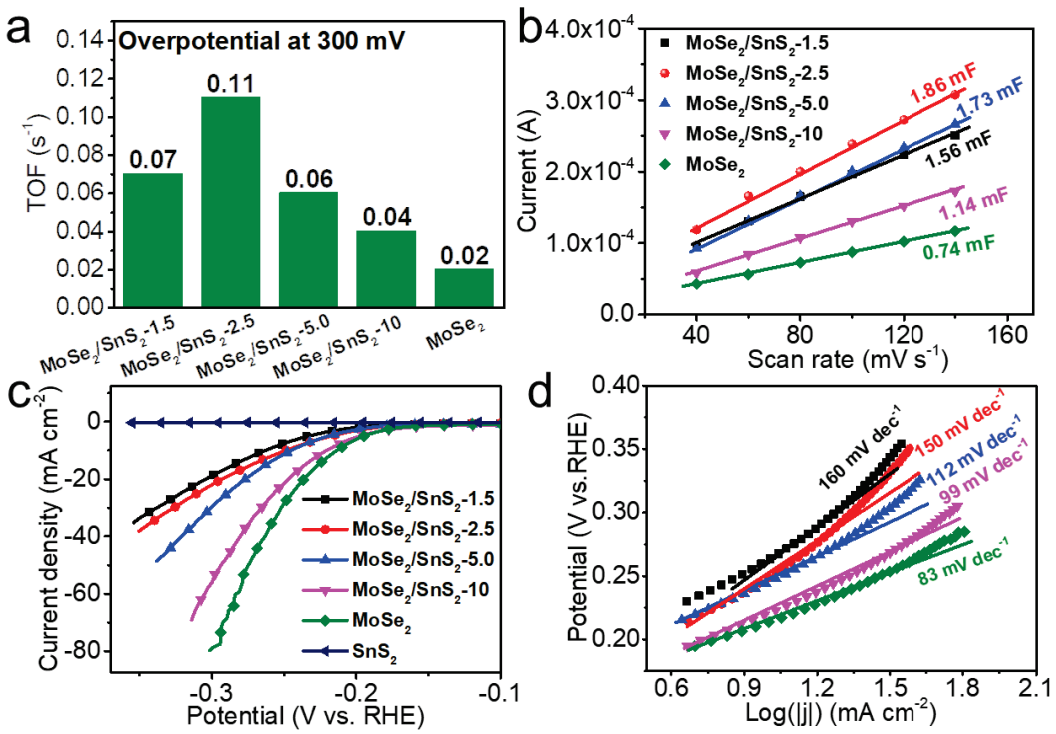

Figure 5.8. (a) TOFs of $MoSe_2/SnS_2$ heterostructures and pure $MoSe_2$ at the overpotential of 0.3 V (vs. RHE); (b) Current versus scan rate measured at 0 V (vs. RHE); (c) The LSV curves and (d) Tafel plots measured in 0.5 M H_2SO_4.

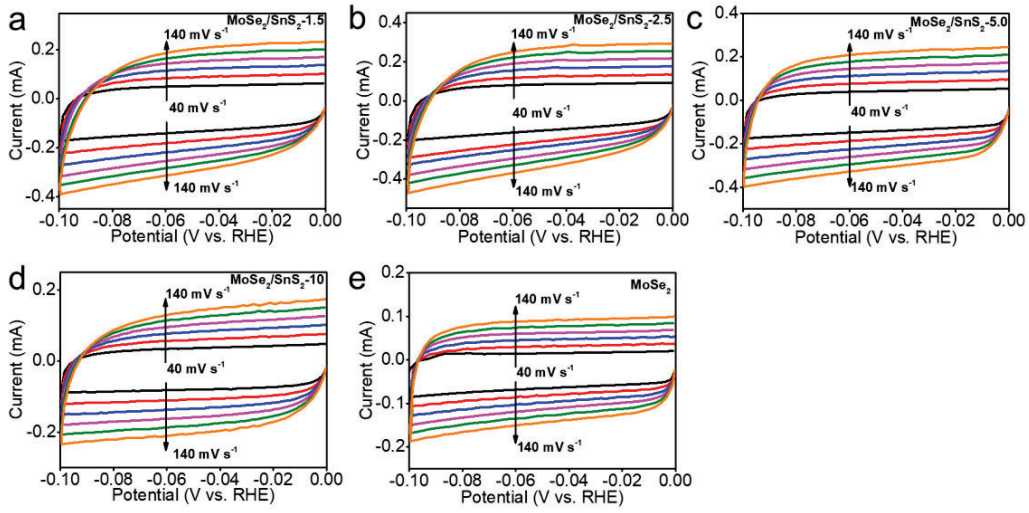

Figure 5.9. CV curves measured in a non-Faradaic region at scan rates from 40 to 140 mV s^{-1} in 1 M KOH: (a) $MoSe_2/SnS_2$-1.5, (b) $MoSe_2/SnS_2$-2.5, (c) $MoSe_2/SnS_2$-5.0, (d) $MoSe_2/SnS_2$-10, and (e) pure $MoSe_2$.

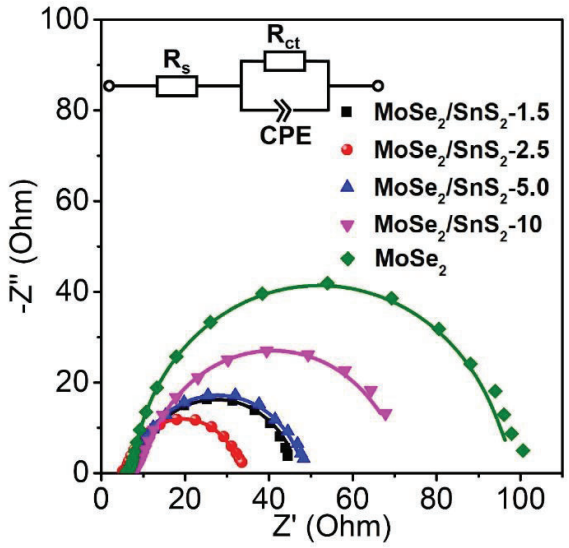

Figure 5.10. EIS spectra of $MoSe_2/SnS_2$ hybrid catalysts and $MoSe_2$ recorded at -0.1 V (vs. RHE). The curves correspond to the fitted results and the scatter plots to measurements. The inset represents the equivalent circuit model.

Table 5.2. TOFs and charge-transfer resistance values for $MoSe_2/SnS_2$ and $MoSe_2$.

	TOF (s^{-1})	Charge-transfer resistance (Ω)
$MoSe_2/SnS_2$-1.5	0.07	38.2
$MoSe_2/SnS_2$-2.5	0.11	27.4
$MoSe_2/SnS_2$-5.0	0.06	42.5
$MoSe_2/SnS_2$-10	0.04	66.4
$MoSe_2$	0.02	96

Turnover frequencies (TOFs) provide important insights in evaluating the intrinsic activity of HER catalysts. Generally, it is supposed that TOFs reflect the formation rate of hydrogen molecules per Mo atom during the HER process.[49-50] Here, we identify the TOF value of $MoSe_2/SnS_2$ catalysts based on $MoSe_2$ which provides intrinsic active sites for the HER. Although the TOF calculation here employs the total Mo atoms in the electrode as the benchmark, which may not exactly reflect the performance of the $MoSe_2/SnS_2$ heterostructures, it provides a general comparison of the HER kinetics between $MoSe_2$ and $MoSe_2/SnS_2$ composites. The $MoSe_2/SnS_2$-2.5 achieves the highest TOF as compared with other samples (**Figure 5.8a and Table 5.2**). Meanwhile, the electrochemically active surface area (ECSA), as another

critical factor for estimating the activity of electrocatalysts, was determined by measuring the double-layer capacitance (C_{dl}) in the potential range of -0.1–0 V (vs. RHE) (**Figure 5.9**). As shown in **Figure 5.8b**, all the $MoSe_2/SnS_2$ heterostructured catalysts display larger C_{dl} values than that of pure $MoSe_2$, indicating that the introduction of SnS_2 endows the heterostructured catalysts with higher active site density.[51] Moreover, the enhanced catalytic activity of $MoSe_2/SnS_2$ heterostructures was confirmed by electrochemical impedance spectroscopy (EIS). The Nyquist plots are well fitted to an equivalent circuit model (**Figure 5.10**), which consists of electrolyte resistance (R_s), charge-transfer resistance (R_{ct}), and constant phase element (CPE). All the heterostructured catalysts show much lower R_{ct} than that of bare $MoSe_2$ (**Table 5.2**), further demonstrating that the incorporation of SnS_2 is beneficial for accelerating the charge transfer and mass diffusion kinetics of $MoSe_2/SnS_2$ heterostructures under alkaline conditions.[52]

To further confirm the effect of incorporating SnS_2 on the enhanced alkaline HER activity of the $MoSe_2/SnS_2$ heterostructured catalysts, the acidic HER performances of $MoSe_2/SnS_2$ and bare $MoSe_2$ catalysts were tested in 0.5 M H_2SO_4 electrolyte. According to previously reported volcano plots, the HER kinetics of a catalyst in acidic conditions is strongly correlated with its hydrogen adsorption capability.[53-54] In sharp contrast to the bare $MoSe_2$, all the $MoSe_2/SnS_2$ heterostructures show higher overpotentials with larger Tafel slopes (**Figure 5.8c-d**). The reduced acidic catalytic activities of the $MoSe_2/SnS_2$ heterostructured catalysts demonstrate that the introduction of SnS_2 had no positive effect on optimizing the hydrogen adsorption capability. It can be inferred that the enhanced alkaline HER activity of the $MoSe_2/SnS_2$ heterostructures can be mainly attributed to the accelerated water adsorption/dissociation process.

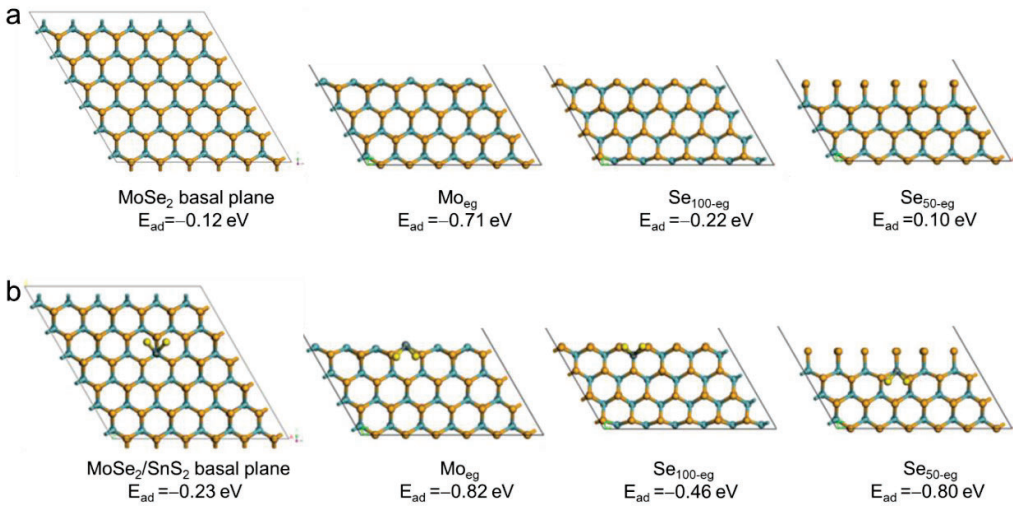

Figure 5.11. Top view of the basal plane and side views of three edge models: Mo-edge, Se-edge with 50%

selenium coverage ($Se_{50\text{-}eg}$), and Se-edge with 100% selenium coverage ($Se_{100\text{-}eg}$) of pure $MoSe_2$ (a) and $MoSe_2/SnS_2$ (b). The cyan and orange balls represent Mo and Se atoms, respectively.

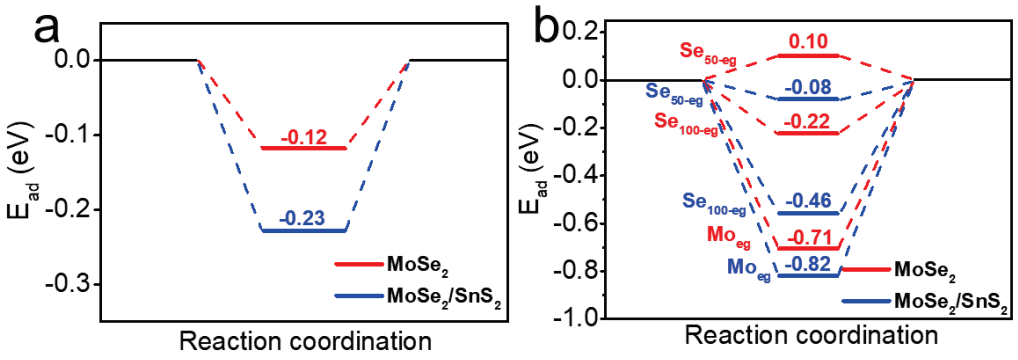

Figure 5.12. Water adsorption energy diagram of $MoSe_2/SnS_2$ and $MoSe_2$ (a) on the basal planes and (b) on the edge sites.

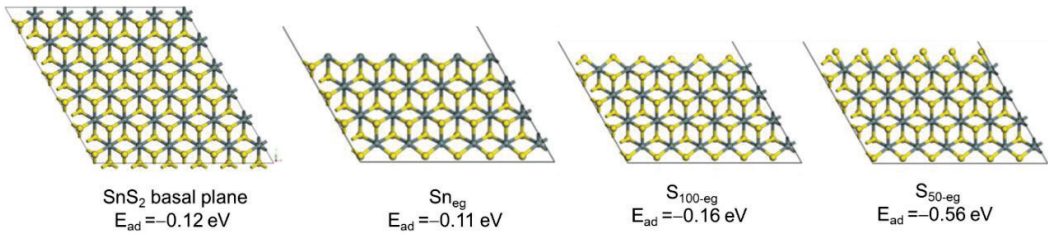

Figure 5.13. Top view of the SnS_2 basal plane and side views of three SnS_2 edge models: Sn-edge, S-edge with 50% sulfur coverage ($S_{50\text{-}eg}$), and S-edge with 100% sulfur coverage ($S_{100\text{-}eg}$). The grey and yellow balls represent Sn and S atoms, respectively.

Basically, water adsorption takes place prior to water dissociation during the alkaline HER process. Therefore, to further verify the influence of SnS_2 quantum dots on the alkaline HER kinetics of $MoSe_2$, DFT calculations were conducted to determine the water adsorption energy (E_{ad}) of the basal planes and edges of pure $MoSe_2$, SnS_2, and $MoSe_2/SnS_2$ (**Figure 5.11**). As shown in **Figure 5.12a**, the E_{ad} of the basal planes of $MoSe_2$ is -0.12 eV. After incorporating SnS_2, the E_{ad} of the basal planes of $MoSe_2/SnS_2$ decreases to -0.23 eV, suggesting that SnS_2 efficiently enhances the water adsorption capability on the basal planes of $MoSe_2$. The Mo edges, as the most stable sites for water adsorption, displays a lower E_{ad} (-0.82 eV) for $MoSe_2/SnS_2$ than that of $MoSe_2$ (-0.71 eV) (**Figure 5.12b**). Meanwhile, the Se edges with 100% and 50% Se coverage ($Se_{100\text{-}eg}$ and $Se_{50\text{-}eg}$) of $MoSe_2/SnS_2$ heterostructures also show decreased E_{ad} values relative to that of pure $MoSe_2$. These results clearly demonstrate that the incorporation of SnS_2 significantly enhances the water adsorption capability of $MoSe_2$ in the heterostructures, which is greatly

beneficial to accelerating the subsequent water dissociation kinetics. In addition, the basal planes and edges of SnS_2 also show promising water adsorption capability (**Figure 5.13**), which can further improve the water adsorption and dissociating kinetics of the $MoSe_2/SnS_2$ heterostructures.

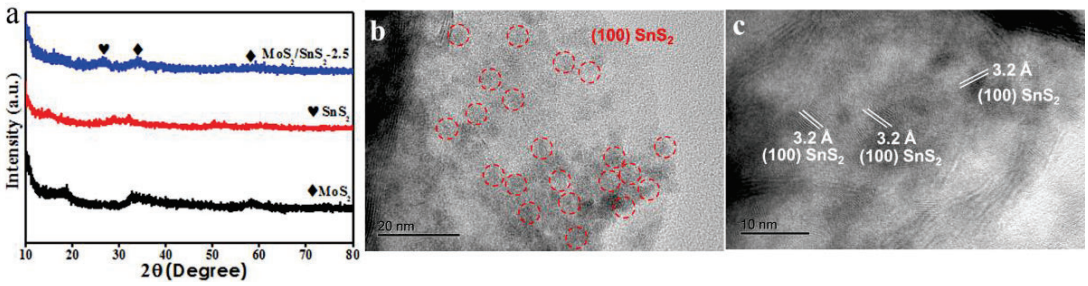

Figure 5.14. (a) XRD patterns and (b, c) TEM images of MoS_2/SnS_2-2.5 hybrid.

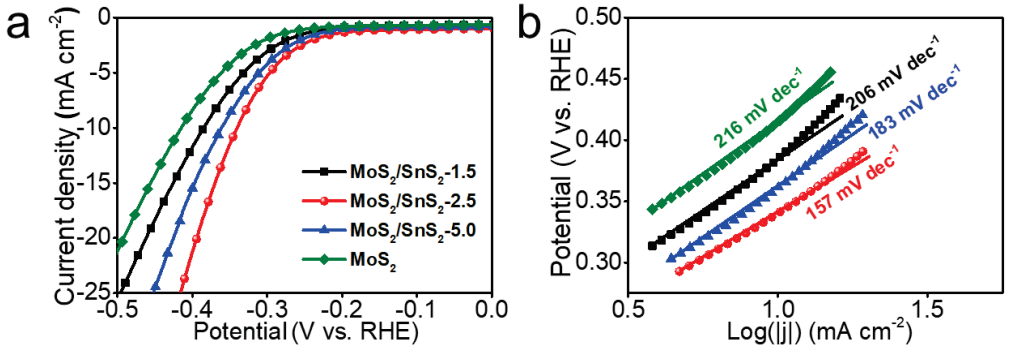

Figure 5.15. LSV curves (a) and Tafel plots (b) of MoS_2/SnS_2 and pure MoS_2 at 1 M KOH media.

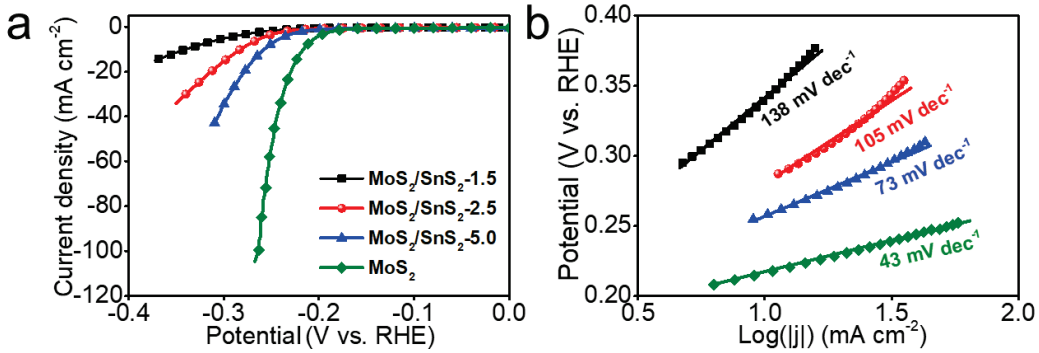

Figure 5.16. LSV curves (a) and Tafel plots (b) of MoS_2/SnS_2 and pure MoS_2 in 0.5 M H_2SO_4.

MoS_2/SnS_2 heterostructures with SnS_2 quantum dots decorated on the basal planes (**Figure 5.14a-c**), which were synthesized by a similar process to that for $MoSe_2/SnS_2$ heterostructures, were also evaluated as the catalysts for the alkaline HER. As shown in Figure **5.15a-b**, the alkaline HER activity of the heterostructured catalysts is also greatly enhanced after the introduction of SnS_2. The optimal MoS_2/SnS_2-2.5 catalyst delivers the lowest overpotential of 343 mV at 10 mA cm^{-2} with a Tafel slope of 157 mV dec^{-}

[1], while pure MoS_2 has an overpotential of 419 mV at 10 mA cm^{-2} with a Tafel slope of 216 mV dec^{-1}. Similar to the case of $MoSe_2/SnS_2$, the acidic HER performance of the MoS_2/SnS_2 heterostructures gets worse with increasing the content of inactive SnS_2 (Figure **5.16a-b**). These results demonstrate that decorating SnS_2 quantum dots on basal planes to construct heterostuctures is a universal approach to promote the alkaline HER kinetics of molybdenum dichalcogenide-based catalysts.

5.4. Conclusion

In summary, molybdenum dichalcogenide heterostructures with SnS_2 quantum dots decorated on the basal planes were designed and synthesized as efficient alkaline HER electrocatalysts. The optimal $MoSe_2/SnS_2$ heterostructured catalyst delivered a substantially lower overpotential of 285 mV as compared with $MoSe_2$ (367 mV) at 10 mA cm^{-2}. The significant improvement in alkaline HER activity is mainly due to the accelerated water adsorption/dissociation kinetics. The DFT calculations reveal that the incorporation of SnS_2 can significantly improve the water adsorption capability of $MoSe_2$, which is critical for the subsequent water dissociation process. This work opens up a new direction for the development of efficient alkaline HER electrocatalysts by engineering heterostructures.

5.5. References

[1] S. Chu, A. Majumdar, *Nature* **2012**, *488*, 294-303.

[2] J. Wang, K. Li, H.-x. Zhong, D. Xu, Z.-l. Wang, Z. Jiang, Z.-j. Wu, X.-b. Zhang, *Angew. Chem. Int. Ed.* **2015**, *127*, 10676-10680.

[3] P. Chen, T. Zhou, M. Zhang, Y. Tong, C. Zhong, N. Zhang, L. Zhang, C. Wu, Y. Xie, *Adv. Mater.* **2017**, *29*, 1701584-1701590.

[4] Z. Gao, J. Qi, M. Chen, W. Zhang, R. Cao, *Electrochim. Acta* **2017**, *224*, 412-418.

[5] J. Mahmood, M. A. R. Anjum, S.-H. Shin, I. Ahmad, H.-J. Noh, S.-J. Kim, H. Y. Jeong, J. S. Lee, J.-B. Baek, *Adv. Mater.* **2018**, *30*, 1805606-1805613.

[6] J. A. Turner, *Science* **2004**, *305*, 972-974.

[7] D. Strmcnik, M. Uchimura, C. Wang, R. Subbaraman, N. Danilovic, D. van der Vliet, A. P. Paulikas, V. R. Stamenkovic, N. M. Markovic, *Nat. Chem.* **2013**, *5*, 300-306.

[8] Y. Jiao, Y. Zheng, M. Jaroniec, S. Z. Qiao, *Chem. Soc. Rev.* **2015**, *44*, 2060-2086.

[9] M.-S. Balogun, W. Qiu, H. Yang, W. Fan, Y. C. Huang, G.-R. Li, H. Ji, Y. Tong, *Energy Environ. Sci.* **2016**, *9*, 3411-3416.

[10] J.-X. Feng, S.-Y. Tong, Y. Tong, G.-R. Li, *J. Am. Chem. Soc.* **2018**, *140*, 5118-5126.

[11] Y. Shenghua, Z.-X. Shi, J.-X. Feng, Y.-X. Tong, G.-R. Li, *Angew.Chem. Int. Ed.* **2018**, *57*, 2672-2676.

[12] W. Anliang, H. Xu, G.-R. Li, *ACS Energy Lett.* **2016**, *1*, 445-453.

[13] J. Feng, H. Xu, Y.-T. Dong, X.-F. Lu, Y.-X. Tong, G.-R. Li, *Angew.Chem. Int. Ed.* **2017**, *56*, 2960-2964.

[14] F. Li, G. Han, H.-J. Noh, Y. Lu, J. Xu, Y. Bu, Z. Fu, J.-B. Baek, *Angew. Chem. Int. Ed.* **2018**, *57*, 14139-14143.

[15] J. Mahmood, F. Li, S.-M. Jung, M. S. Okyay, I. Ahmad, S.-J. Kim, N. Park, H. Y. Jeong, J.-B. Baek, *Nat. Nanotechnol.* **2017**, *12*, 441-446.

[16] Z. Dai, H. Geng, J. Wang, Y. Luo, B. Li, Y. Zong, J. Yang, Y. Guo, Y. Zheng, X. Wang, Q. Yan, *ACS Nano* **2017**, *11*, 11031-11040.

[17] Z.-L. Wang, X.-F. Hao, Z. Jiang, X.-P. Sun, D. Xu, J. Wang, H.-X. Zhong, F.-L. Meng, X.-B. Zhang, *J. Am. Chem. Soc.* **2015**, *137*, 15070-15073.

[18] M. G. Walter, E. L. Warren, J. R. McKone, S. W. Boettcher, Q. Mi, E. A. Santori, N. S. Lewis, *Chem. Rev.* **2010**, *110*, 6446-6473.

[19] Y. Chen, Q. Zhou, G. Zhao, Z. Yu, X. Wang, S. X. Dou, W. Sun, *Adv. Funct. Mater.* **2017**, *28*, 1705583-1705590.

[20] B. M. Hunter, H. B. Gray, A. M. Müller, *Chem. Rev.* **2016**, *116*, 14120-14136.

[21] Z. Chen, Y. Song, J. Cai, X. Zheng, D. Han, Y. Wu, Y. Zang, S. Niu, Y. Liu, J. Zhu, X. Liu, G. Wang, *Angew. Chem. Int. Ed.* **2018**, *57*, 5076-5080.

[22] C. Tan, H. Zhang, *Chem. Soc. Rev.* **2015**, *44*, 2713-2731.

[23] X. Sun, J. Dai, Y. Guo, C. Wu, F. Hu, J. Zhao, X. Zeng, Y. Xie, *Nanoscale* **2014**, *6*, 8359-8367.

[24] Y. Zhang, Q. Zhou, J. Zhu, Q. Yan, S. X. Dou, W. Sun, *Adv. Funct. Mater.* **2017**, *27*, 1702317.

[25] K. Tang, X. Wang, Q. Li, C. Yan, *Adv. Mater.* **2018**, *30*, 1704779-1704786.

[26] K. K. Ghuman, S. Yadav, C. V. Singh, *J. Phys. Chem. C* **2015**, *119*, 6518-6529.

[27] C. Tsai, K. Chan, F. Abild-Pedersen, J. K. Nørskov, *Phys. Chem. Chem. Phys.* **2014**, *16*, 13156-13164.

[28] Y. Shi, Y. Zhou, D. Yang, W. Xu, C. Wang, F. Wang, J. Xu, X. Xia, H. Chen, *J. Am. Chem. Soc.* **2017**, *139*, 15479–15485.

[29] N. Xue, P. Diao, *J. Phys. Chem. C* **2017**, *121*, 26686–26697.

[30] H. Shu, D. Zhou, F. Li, D. Cao, X. Chen, *ACS Appl. Mater. Inter.* **2017**, *9*, 42688–42698.

[31] O. Lehtinen, H.-P. Komsa, A. Pulkin, M. B. Whitwick, M.-W. Chen, T. Lehnert, M. J. Mohn, O. V. Yazyev, A. Kis, U. Kaiser, A. V. Krasheninnikov, *ACS Nano* **2015**, *9*, 3274-3283.

[32] Y. Yin, Y. Zhang, T. Gao, T. Yao, X. Zhang, J. Han, X. Wang, Z. Zhang, P. Xu, P. Zhang, X. Cao, B. Song, S. Jin, *Adv. Mater.* **2017**, *29*, 1700311-1700319.

[33] K. Xu, H. Ding, M. Zhang, M. Chen, Z. Hao, L. Zhang, C. Wu, Y. Xie, *Adv. Mater.* **2016**, *29*, 1606980-1606986.

[34] G. Chen, T. Wang, J. Zhang, P. Liu, H. Sun, X. Zhuang, M. Chen, X. Feng, *Adv. Mater.* **2018**, *30*, 1706279-1706286.

[35] J. Zhang, T. Wang, P. Liu, Z. Liao, S. Liu, X. Zhuang, M. Chen, E. Zschech, X. Feng, *Nat. Commun.* **2017**, *8*, 15437-15445.

[36] M. Lao, K. Rui, G. Zhao, P. Cui, X. Zheng, S. X. Dou, W. Sun, *Angew. Chem. Int. Ed.* **2019**, *58*, 5432-5437.

[37] G. Zhao, K. Rui, S. X. Dou, W. Sun, *Adv. Funct. Mater.* **2018**, *28*, 1803291.

[38] G. Zhao, Y. Lin, K. Rui, Q. Zhou, Y. Chen, S. X. Dou, W. Sun, *Nanoscale* **2018**, *10*, 19074-19081.

[39] G. Zhao, P. Li, K. Rui, Y. Chen, S. X. Dou, W. Sun, *Chem. Eur. J.* **2018**, *24*, 11158-11165.

[40] C. Lei, Y. Wang, Y. Hou, P. Liu, J. Yang, T. Zhang, X. Zhuang, M. Chen, B. Yang, L. Lei, C. Yuan, M. Qiu, X. Feng, *Energy Environ. Sci.* **2019**, *12*, 149-156.

[41] B. Song, S. Jin, *Joule* **2017**, *1*, 220-221.

[42] B. Zhang, J. Liu, J. Wang, Y. Ruan, X. Ji, K. Xu, C. Chen, H. Wan, L. Miao, J. Jiang, *Nano Energy* **2017**, *37*, 74-80.

[43] J. Yang, C. Wang, H. Ju, Y. Sun, S. Xing, J. Zhu, Q. Yang, *Adv. Funct. Mater.* **2017**, *27*, 1703864-1703874.

[44] X. Zhou, Y. Liu, H. Ju, B. Pan, J. Zhu, T. Ding, C. Wang, Q. Yang, *Chem. Mater.* **2016**, *28*, 1838-1846.

[45] J. Zhang, T. Wang, P. Liu, S. Liu, R. Dong, X. Zhuang, M. Chen, X. Feng, *Energy Environ. Sci.* **2016**, *9*, 2789-2793.

[46] X.-Y. Yu, Y. Feng, Y. Jeon, B. Guan, X. W. Lou, U. Paik, *Adv. Mater.* **2016**, *28*, 9006-9011.

[47] C. C. McCrory, S. Jung, J. C. Peters, T. F. Jaramillo, *J. Am. Chem. Soc.* **2013**, *135*, 16977-16987.

[48] C. Ataca, S. Ciraci, *Phys. Rev. B* **2012**, *85*, 195410.

[49] Y.-C. Chen, A.-Y. Lu, P. Lu, X. Yang, C.-M. Jiang, M. Mariano, B. Kaehr, O. Lin, A. Taylor, I. D. Sharp, L.-J. Li, S. S. Chou, V. Tung, *Adv. Mater.* **2017**, *29*, 1703863-1703874.

[50] H. Li, C. Tsai, A. L. Koh, L. Cai, A. W. Contryman, A. H. Fragapane, J. Zhao, H. S. Han, H. C. Manoharan, F. Abild-Pedersen, J. K. Nørskov, X. Zheng, *Nat. Mater.* **2015**, *15*, 48-54.

[51] S. Sun, H. Li, Z. J. Xu, *Joule* **2018**, *2*, 1024-1027.

[52] Y. Wu, X. Liu, D. Han, X. Song, L. Shi, Y. Song, S. Niu, Y. Xie, J. Cai, S. Wu, J. Kang, J. Zhou, Z. Chen, X. Zheng, X. Xiao, G. Wang, *Nat. Commun.* **2018**, *9*, 1425.

[53] T. F. Jaramillo, K. P. Jørgensen, J. Bonde, J. H. Nielsen, S. Horch, I. Chorkendorff, *Science* **2007**, *317*, 100-102.

[54] J. Greeley, T. F. Jaramillo, J. Bonde, I. Chorkendorff, J. K. Nørskov, *Nat. Mater.* **2006**, *5*, 909.

[55] S. J. Clark, M. D. Segall, C. J. Pickard, P. J. Hasnip, M. J. Probert, K. Refson, M. C. Payne, *Z. Kristallogr.* **2005**, *220*, 567-570.

[56] Materials Studio, version 7.0, Accelrys Inc., San Diego, 2013.

[57] J. P. Perdew, K. Burke, M. Ernzerhof, *Phys. Rev. Lett.* **1996**, *77*, 3865-3868.

[58] S. Grimme, *J. Comput. Chem.* **2006**, *27*, 1787-1799.

[59] D. Vanderbilt, *Phys. Rev. B*, **1990**, *41*, 7892-7895.

[60] H. J. Monkhorst, J. D. Pack, *Phys. Rev. B* **1976**, *13*, 5188-5192.

Note: The content of this chapter has been published in **Nano Energy.** Permission regarding copyright has been obtained from the publishers. [Yaping Chen, Xingyong Wang, Mengmeng Lao, Kun Rui, Xiaobo Zheng, Haibo Yu, Jing Ma, Shi Xue Dou, Wenping Sun,* Electrocatalytically inactive SnS_2 promotes water adsorption/dissociation on molybdenum dichalcogenides for accelerated alkaline hydrogen evolution. **Nano Energy. 2019, 64, 103918.**]

Chapter 6

6. Hexagonal Boron Nitride as a Multifunctional Substrate for Engineering Durable Electrocatalysts towards Enhanced Oxygen Reduction Reaction

6.1. Introduction

Noble metal nanoparticles (NPs) have been the focus of intense research in the catalysis field due to the advantages of large surface-to-volume ratio and high utilization of noble metals.[1-2] Numerous studies have concentrated on enhancing the catalytic performance of noble metal NPs via a variety of nanostructure engineering strategies, including but not limited to tuning particle size, morphology and chemical composition. Basically, noble metal NPs are usually loaded on the supports to mitigate the aggregation and to achieve long-term performance durability with the aids of the strong coupling between NPs and the supports, like Pt/C electrocatalyst for fuel cells. However, although it has been well established that the supports play a pivotal role in modulating and stabilizing the NPs, there is a lack of specific research attention focused on developing new functional supports and modulating the physicochemical properties of the functional supports.

As is well-known, carbon-based materials (e.g., activated carbon, carbon nanotubes, reduced graphene oxide) are extensively deployed as functional supports for noble metal NPs and other non-noble metal catalysts due to their high conductivity and proper chemical stability. Unfortunately, a big challenge remains regarding thermodynamics instability of carbon materials, and they tend to be oxidized at high operation potentials, which would consequently damage the structural integrity of the catalyst, cause agglomeration of noble metal NPs, and eventually result in degradation of catalytic activity.[3-4] Notably, the instability of carbon support is considered to be one of the critical reasons for the inferior durability of the commercial Pt/C electrocatalyst for oxygen reduction reaction (ORR) in fuel cells. Graphene analogues, particularly reduced graphene oxide, have been extensively investigated as the active phases or functional supports for constructing hybrid electrocatalysts. Graphene-like 2D hexagonal boron nitride (h-BN), however, has not drawn intense attention in the electrocatalysis field, which is in great part due to its wide band gap (low conductivity) and electrochemical inertness. Nevertheless, h-BN is a compound possessing exceptional chemical stability and anti-oxidation/corrosion capability in harsh environments.[5-

[7] We recently found that, compared to other typical carbon-based materials, h-BN exhibits superior anti-oxidation property at high potentials **(Figure 6.1**), strongly suggesting that h-BN has great potential to work as a robust support for confining the active noble metal NPs and constructing durable heterostructured catalysts. More importantly, h-BN contains large quantities of B and N, which would provide unique chemical coordination environment and electronic interaction at the interfaces of the heterostructured catalysts. On the other hand, h-BN is superhydrophobic (superaerophilic), which means it has excellent affinity with gas bubbles in aqueous solutions.[8-9] This kind of surface property is of great importance for accelerating the kinetics of ORR, which is a typical gas-consuming reaction occurring at liquid/gas/solid interface and is closely associated with the effective adsorption of O_2.[10-12] On this basis, we hypothesize that h-BN could serve as a potential multifunctional substrate for constructing noble metal-based heterostructured electrocatalysts, particularly for electrochemical reactions occurring at high potentials or under other harsh conditions. In order to prove the hypothesis, we designed and synthesized h-BN/Pd heterostructures with Pd NPs anchored on ultrathin h-BN nanosheets towards ORR application. Interestingly, the h-BN/Pd heterostructured catalyst delivered exceptional catalytic performance in terms of specific activity and durability, and the interface chemistry in the heterostructures was also unravelled, clearly evidencing that h-BN is a multifunctional substrate for engineering durable and highly active ORR electrocatalysts.

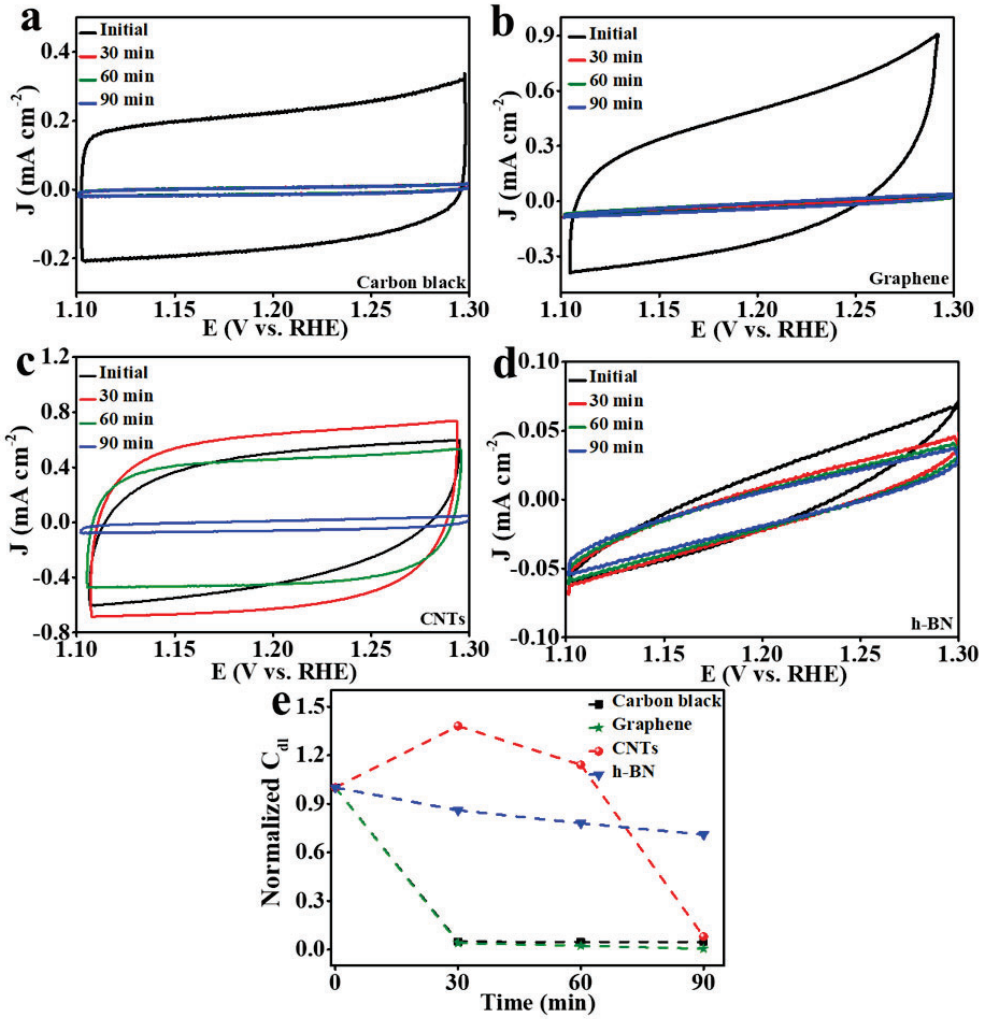

Figure 6.1. CV curves measured with different oxidation time in a non-Faradaic region in 0.1 M KOH at scan rates of 100 mV s^{-1}: (a) Carbon black, (b) graphene, (c) carbon nanotubes (CNTs), and (d) h-BN. (e) Normalized capacitance (C_{dl}) estimated by CV curves at different chronoamperometry (CA) test time of the samples.

6.2. Experimental Section

6.2.1. Materials

All the chemicals were purchased from Sigma-Aldrich (A.R) and were used as received without further purification.

6.2.2. Materials Preparation

6.2.2.1. Exfoliation of h-BN Nanosheets

The bulk h-BN was exfoliated according to the reported method with a slight modification.[46] In brief, 1 g

bulk h-BN (purchased from Alfa Aesar, Thermo Fisher Scientific, purification of 99.5%) in quartz tube was heated in a 800 °C muffle furnace for 10 min and immediately immersed into liquid N_2 taken in a special tin until the liquid N_2 completely gasified. The above procedures were repeated for five times. The exfoliated h-BN was transferred into isopropanol (IPA) and sonicated for 1 h， and centrifuged at 1500 r.p.m. for 15 min. Then the supernatant was centrifuged 10000 r.p.m. for 10 min and dried in vacuum oven overnight.

6.2.2.2. Synthesis of h-BN/C/Pd

To enhance the conductivity of heterostructures, the carbon layer was firstly wrapped on the surface of h-BN. 6 mg exfoliated h-BN and 100 mg glucose were together dispersed into 35 ml mixing solvent (the volume ratios of IPA/water equal to 3:4) and sonicated for 30 min. Next, the homogeneous solution was transferred into 50 ml Teflon lined stainless steel autoclaves for a hydrothermal process at 180 °C for 4 h. The products were further graphitized at 1000 °C for 4 h to attain h-BN/C. For the preparation of h-BN/C/Pd:17, 6 mg h-BN/C and 28.2 μl Na_2PdCl_4 (0.5 M) aqueous solution were added into 40 ml IPA solution with a sonication of 1 h. Then the homogeneous solution was reacted by reflux condensation for 30 mins at 80 °C. The h-BN/C/Pd catalyst was collected after centrifugation, washing, and drying. The h-BN/C/Pd:10 catalyst was prepared by the same procedure as for h-BN/C/Pd:17 with decreasing Na_2PdCl_4 (0.5 M) to 14.1 μl. The accurate mass ratios of Pd in h-BN/C/Pd heterostructures (Pd wt.% = 10 % for h-BN/C/Pd:10; Pd wt.% = 17 % for h-BN/C/Pd:17; Pd wt.% = 17 % for h-BN/Pd:17) were determined by inductively coupled plasma–optical emission spectrometry (ICP-OES, Perkin-Elmer, Optima 7300DV) with mass spectrometry.

6.2.2.3. Synthesis of Pd Nanoparticles

28.2 μl Na_2PdCl_4 (0.5 M) aqueous solution was dispersed in 40 ml IPA solvent and sonicated for 10 min. The uniform solution was raised to 80 °C and kept reflux condensation for 30 min. The Pd NPs were collected after centrifugation, washing, and drying.

6.2.3. Physical Characterization

X-ray diffraction (XRD) measurement was conducted on GBC MMA X-ray diffractometer (λ = 1.5406 Å, 25 mA, 40 Kv, step size of 0.02° s^{-1}). The morphology characteristic of all samples were carried out by transmission electron microscopy (TEM, JEM-2010, working voltage 200 kV). The scanning transmission electron microscopy (STEM) elemental mappings and electron energy loss spectra (EELS) were collected on the JEOL ARM-200F at 200 kV equipped with an EDS detector. X-ray photoelectron

spectroscopy (XPS) testing was carried out on a Thermo ESCALAB 250Xi instrument with monochrome Al Kα (hv = 1486.6 eV) as the X-ray excitation source.

6.2.4 X-ray Absorption Fine Structure (XAFS) Spectra Characterizations

XAFS measurements at Pd k-edge in both transmission (for Pd foil) and fluorescence (for samples) mode were carried out at beamline BL14W1 in Shanghai Synchrotron Radiation Facility (SSRF). The operation energy of storage ring was 3.5 GeV and at the current around 240 mA. The white X-ray was monochromatized using a fixed-exit double-crystal Si (111) monochromator and the energy was calibrated by using Pt foil. Pd standards and the prepared samples were compacted and collected in transmission mode at room temperature. The data analysis was performed using software Demeter as the standard data analysis procedures.[41-42] This qualitative analysis was primarily focused on the nature of the backscattering atoms as well as the bond lengths and complemented the conventional Fourier transform (FT) analysis by connecting contributions in the EXAFS spectra to the FT peaks.

6.2.5. Electrochemical Measurement

Electrochemical measurements were performed on a VSP-300 electrochemical workstation (BioLogic Science Instrument, France) connected to a rotating disk electrode (Pine Research Instruments, U.S.). All electrochemical measurements were conducted in 0.1 M KOH aqueous solution. Hg/HgO (1 M KOH solution) electrode and a platinum wire were employed as the reference electrode and counter electrode, respectively. The working electrodes were prepared by coating catalyst inks on the surface of glassy carbon electrode. The mass loading of all samples on the polished glassy carbon electrode were 200 μg cm^{-2}. To prepare the catalyst ink for h-BN/Pd/C:17 and commercial Pd/C (20 wt.% Pd), 2 mg catalysts were dispersed in the mixture of 16 μL Nafion solution (Aldrich Co., 5 wt.%), 384 μL deionized water and 100 μL isopropanol and treated with ultrasonication for 3 h. To prepare the catalyst inks for Pd NPs and h-BN/Pd:17, 1.88 mg catalysts were first mixed with 0.12 mg Vulcan XC-72 carbon black (same carbon amount with the amount of carbon layer in h-BN/Pd/C:17), and then the mixed powders were dispersed in the mixture of 16 μL Nafion solution, 384 μL deionized water and 100 μL isopropanol and treated with ultrasonication for 3 h.

Stability tests (25 °C) were carried out by 10000 cyclic voltammetry (CV) cycles between 0.4 and 1.0 V at a scan rate of 100 mV/s. Electrochemically active surface area (ECSA) was evaluated by the hydrogen underpotential deposition (Hupd) method.[35] The CV curves of the samples were recorded at the scan rate of 50 mV s^{-1} in N_2-saturated 0.1 M KOH solution. Electrochemical impedance spectra (EIS) were

measured at 0.87 V (vs. RHE) within the frequency range of 100 kHz-1Hz.

The kinetic current (J_k) can be calculated by the Koutecky–Levich equation which is represented by

$$\frac{1}{J} = \frac{1}{J_k} + \frac{1}{J_d} \quad (6.1)$$

Where J stands for the measured current and J_d for the diffusion limited current.

The number of electrons transferred (n) can be estimated by the Levich equation:

$$J_d = 0.62nFAD^{2/3}\upsilon^{-1/6}\omega^{1/2}C_{O_2} \quad (6.2)$$

where F stands for Faraday's constant (96485 C mol^{-1}). A is the area of electrode (0.196 cm^2), and D is the diffusion coefficient of O_2 in 0.1 M KOH solution (1.93×10^{-5} cm^2 s^{-1}). υ stands for the kinematic viscosity of the electrolyte (1.01×10^{-2} cm^2 s^{-1}). ω represents the angular frequency of rotation: $\omega = 2\pi f/60$, f in r.p.m. is the RDE rotation rate, and C_{O_2} is the concentration of molecular oxygen in 0.1M KOH electrolyte (1.26×10^{-6} mol cm^{-3}).

6.3. Results and Discussion

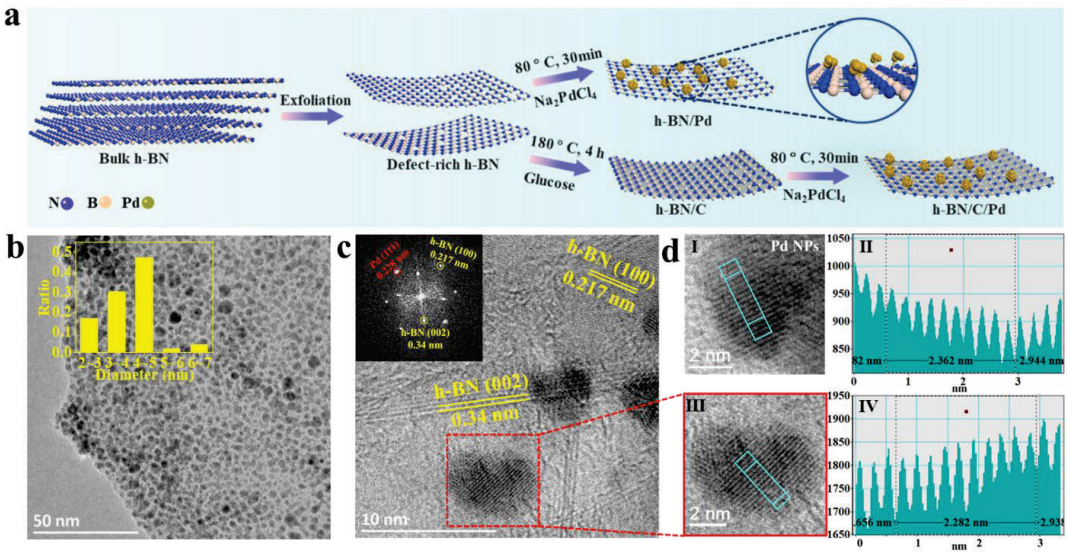

Figure 6.2. (a) Schematic illustration showing exfoliation of h-BN and preparation of h-BN/C/Pd. (b) TEM of h-BN/C/Pd:17, (inset: particle size distribution of Pd NPs). (c) HRTEM of h-BN/C/Pd:17, (inset: corresponding FFT image). (d) The HRTEM images and intensity profiles of Pd NPs (Ⅰ and Ⅱ), and h-BN/C/Pd:17 (Ⅲ and Ⅳ), respectively.

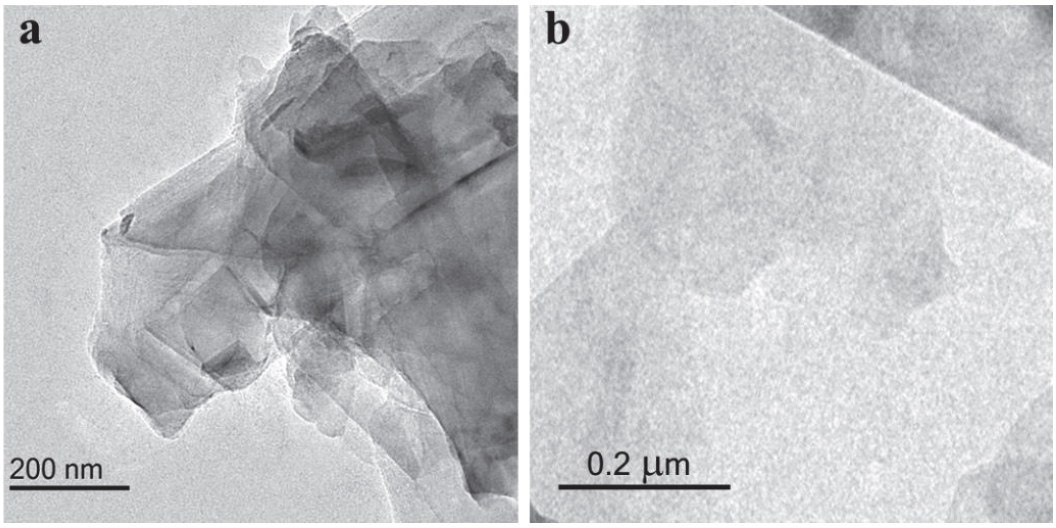

Figure 6.3. The TEM images of (a) bulk h-BN and (b) exfoliated h-BN.

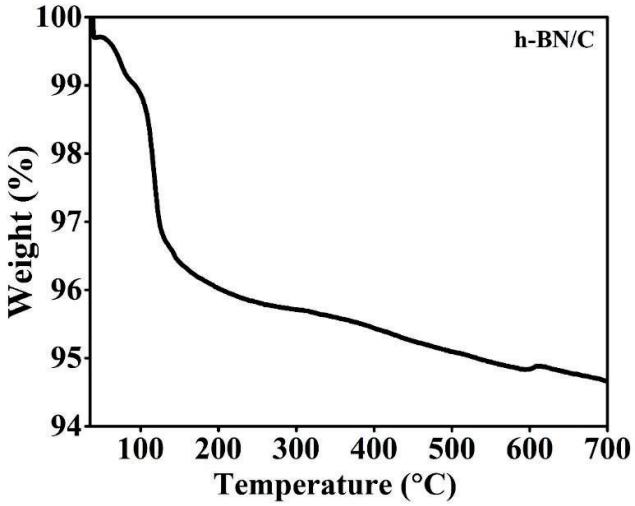

Figure 6.4. Thermogravimetry (TG) of h-BN/C.

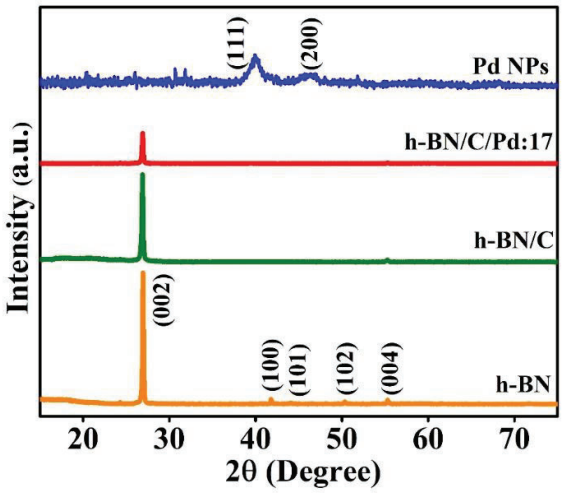

Figure 6.5. XRD patterns of Pd NPs, h-BN/C/Pd:17, h-BN/C, and h-BN.

The h-BN/Pd heterostructures were synthesized as illustrated in **Figure 6.2a** (See Experimental Section for details). Firstly, h-BN nanosheets were prepared by exfoliation with the assistance of cryogenic liquid-N_2 gasification (**Figure 6.3**). Notably, abundant N-vacancies and B-vacancies were created during the exfoliation process. Then, Pd NPs were deposited on h-BN nanosheets via a solution reduction process to obtain h-BN/Pd heterostructure. In another approach, to improve the conductivity of heterostructured catalysts, the exfoliated h-BN nanosheets were functionalized by coating thin carbon layers (h-BN/C) before the deposition of Pd NPs, which was achieved through a typical hydrothermal process with glucose as the carbon source followed by high-temperature graphitization. The content of carbon layer is estimated to be around 6 wt.% determined by thermogravimetric analysis (**Figure 6.4**). The heterostructure based on this functionalized substrate is referred as h-BN/C/Pd. The XRD patterns (**Figure 6.5**) reveal that all the diffraction peaks can be correspondingly assigned to h-BN (JCPDS No. 34-0421) and Pd (JCPDS No. 46-1043).

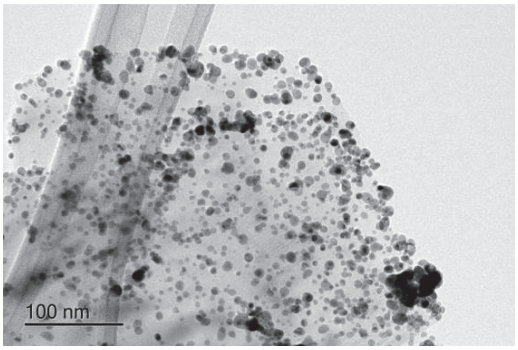

Figure 6.6. The TEM image of h-BN/Pd:17.

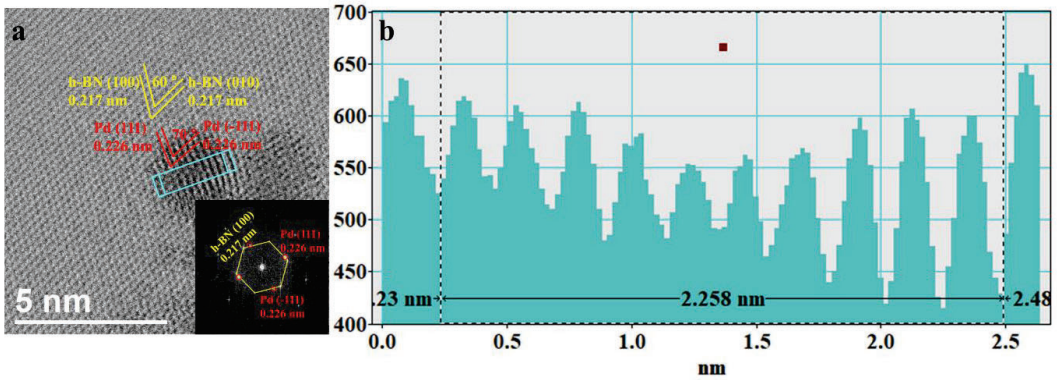

Figure 6.7. (a) The HRTEM images of h-BN/Pd:17, (inset: corresponding FFT images). (b) The intensity profile corresponding to Pd NPs of (a).

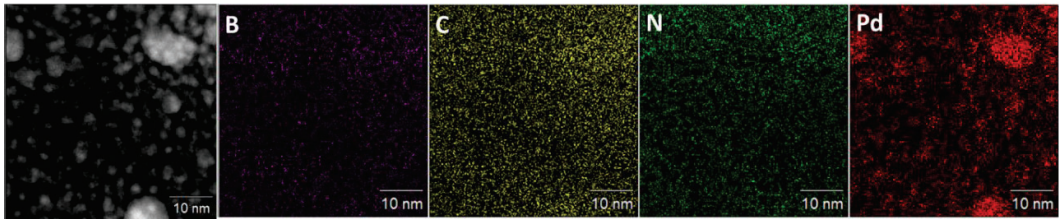

Figure 6.8. The STEM elemental mapping of h-BN/C/Pd:17.

The bright-field transmission electron microscopy (TEM) images show that Pd NPs (2-6 nm) are successfully anchored on h-BN and h-BN/C nanosheets (**Figure 6.2b and 6.6**), and the content of Pd is determined to be 17 wt% (h-BN/Pd:17 and h-BN/C/Pd:17). As can be seen from the high-resolution TEM (HRTEM) image and corresponding Fast Fourier transformation (FFT) pattern (Figure 1c), the lattice spacing of 0.217 and 0.34 nm are matched well with the (100) and (002) planes of h-BN, respectively. Meanwhile, as shown in **Figure 6.2d and 6.7**, the d-spacing of 0.282 and 0.258 can be assigned to the (111) planes of Pd in heterostructures while 0.236 agrees well with the (111) plane of Pd NPs. Clearly, there is a significant lattice contraction up to 3.5% and 4.4% (I could obtain contraction percentage related to the bulk Pd lattice: i.e. $(a-a_{Pd})/a_{Pd}\times100\%$, where a stands for lattice spacing) on Pd (111) plane after the hybridization with h-BN as compared with Pd NPs, indicating the formation of compressive lattice strain for Pd due to the confinement of h-BN. The lattice strain can be used as a main structure-relevant factor to dominate the electrocatalytic activity.[24-26] And the compressed lattice can lead to a downshift of d-band centre for Pd, which could weaken the adsorbate bond strength and accordingly facilitate the desorption of intermediates to form H_2O.[25] The scanning transmission electron microscopy (STEM) elemental mappings further demonstrate that the surface of h-BN nanosheets is decorated with uniform Pd NPs (**Figure 6.8**).

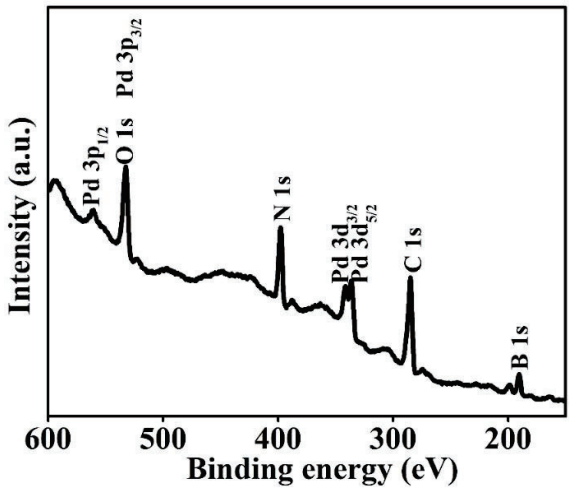

Figure 6.9. The XPS survey spectrum of h-BN/C/Pd:17.

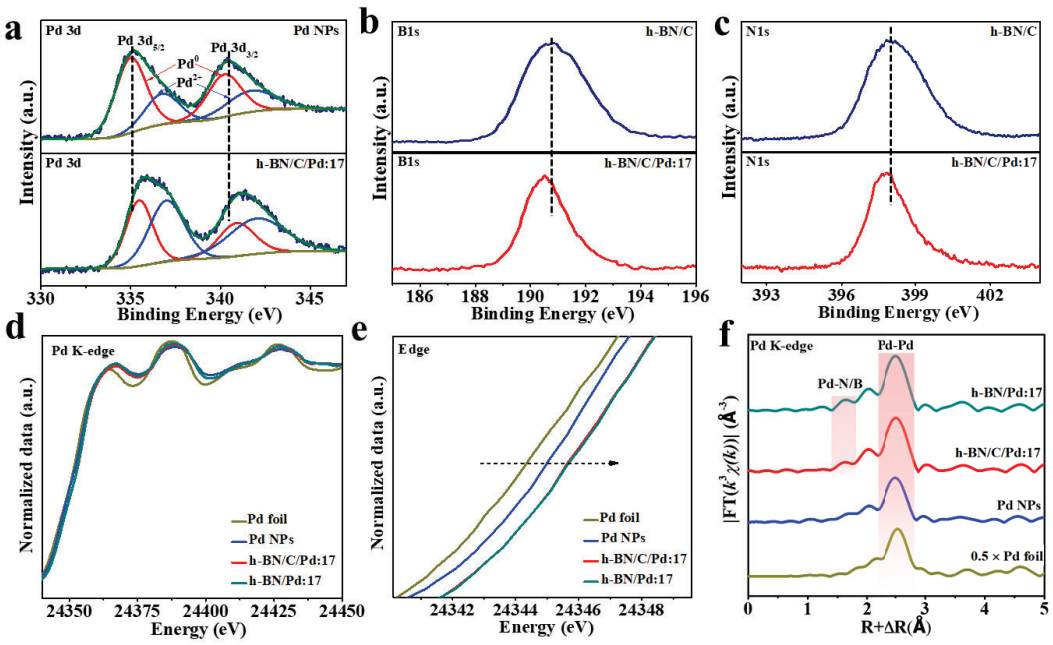

Figure 6.10. (a) XPS spectra of Pd 3d core levels for Pd NPs and h-BN/C/Pd:17. (b) and (c) XPS of B and N 1s for h-BN/C and h-BN/C/Pd:17. (d) XANES spectra measured in transmission mode near the Pd K-edge and (e) the corresponding zoom-in edge spectra. (f) The Pd K-edge k^3-weighted EXAFS oscillations.

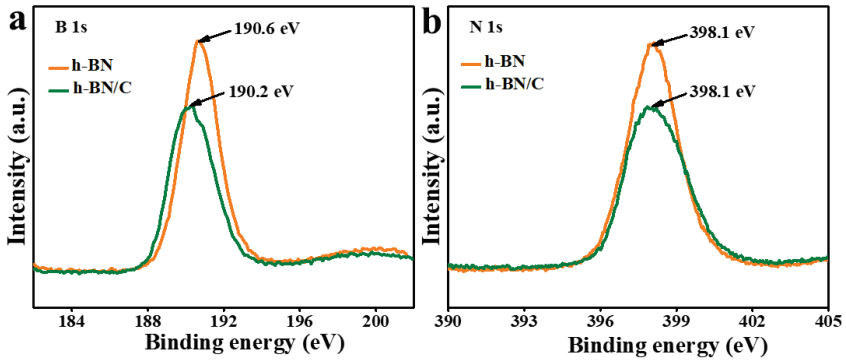

Figure 6.11. The XPS of B 1s and N 1s core levels for h-BN and h-BN/C.

The survey X-ray photoelectron spectroscopy (XPS) spectrum of h-BN/C/Pd:17 confirms the coexistence of B, N, C and Pd elements (**Figure 6.9**). **Figure 6.10a** shows high-resolution Pd 3d spectra for h-BN/C/Pd:17 and Pd NPs. Compared to the Pd NPs, the binding energy of Pd $3d_{3/2}$ and Pd $3d_{5/2}$ for h-BN/C/Pd:17 shifts positively by 0.7 eV and 0.8 eV, respectively, indicating that the electron density surrounding Pd atoms is reduced in the heterostructures. It should be noted that the upshift of binding energy indicates the downshift of d-band centre of Pd. Such electronic structure modulation of Pd is beneficial to optimize (weaken) the adsorption energy of the reaction intermediates (e.g. O_{ad} and OH_{ad}) and hence facilitate the formation of H_2O.[27-28] Meanwhile, it is clear that the ratio of oxidized Pd atoms (Pd^{2+}) to metal Pd atoms (Pd^0) in the heterostructure is increased accordingly as compared with bare Pd NPs. Basically, the change of Pd electronic structure is closely associated with the presence of h-BN, which provides unique B- and N-abundant chemical coordination environment at the heterostructure interface. Correspondingly, the binding energies of N 1s and B 1s both display evident negative shift by 0.3 eV after depositing Pd NPs (**Figure 6.10b-c**), further suggesting the strong electronic interaction between h-BN and Pd NPs at the heterostructure interface.

To further investigate the local electronic structure of Pd in the heterostructures, the Pd K-edge X-ray absorption near edge structure (XANES) and extended X-ray absorption fine structure (EXAFS) spectra were carried out. As displayed in **Figure 6.10d**, the Pd K-edge XANES spectra of h-BN/C/Pd:17 and h-BN/Pd:17 resemble those of Pd NPs and Pd foil, demonstrating that Pd mainly exists in the metallic state in the heterostructures. Meanwhile, the shift of XANES edge position demonstrates the variations in the valence state.[29-30] Clearly, the adsorption edges of both h-BN/C/Pd:17 and h-BN/Pd:17 shift positively compared with that of Pd NPs (**Figure 6.10e**), demonstrating the higher valence state as well as the decreased electron density of the Pd 4d states in the heterostructures.[31] Intriguingly, the reduced

occupation in the Pd 4d states reduces the energy of antibonding orbitals, and hence increase the filling of the antibonding, which subsequently weakens the bonding strength with the Oad and OHad intermediates.[32-33] The results are in good consistence with the XPS spectra as well. In the meantime, the B 1s XPS results demonstrate the interaction between carbon layer and boron atoms (**Figure 6.11**). However, the similar adsorption edge of h-BN/Pd:17 and h-BN/C/Pd:17 proves no apparent electronic interaction between Pd and the carbon layer. The Fourier transforms EXAFS (FT-EXAFS) spectra of the Pd K-edge is shown in **Figure 6.10f**, and the peak at around 2.5 Å is attributed to Pd–Pd bonds, further verifying the presence of metallic Pd. With regard to atom coordination at the interface, we can observe the formation of chemical bonding between Pd and h-BN. However, the bond lengths of Pd-N and Pd-B bonds are too similar to be distinguished, and thus the interfacial bonding is described as Pd-N/B (**Table 6.1**). Considering N has higher electronegativity than B, Pd-N bonding is probably dominant in the chemical coordination chemistry at the heterostructure interface. Moreover, the bond lengths of Pd-Pd in h-BN/C/Pd:17 (2.71 Å) and h-BN/ Pd:17 (2.72 Å) heterostructures are compressive in comparison with Pd NPs (2.73 Å). It has been well established that the change of bond length cause the generation of strain.[34] Accordingly, the compressed Pd-Pd bond results in compressed strain weaken the chemisorption of oxygenous intermediates, and thus benefiting the final formation of H_2O.[35-36] The intensity of Pd-Pd peak is decreased compared to that of Pd foil due to smaller particle size.[37-38]

Table 6.1. EXAFS fitting parameters at the Pd K-edge for various samples（S_0^2=0.829）

Note. [a]*N*: coordination numbers; [b]*R*: bond distance; [c]σ^2: Debye-Waller factors; [d] ΔE_0: the inner potential correction. *R* factor: goodness of fit. S_0^2 was set to 0.829, according to the experimental EXAFS fit of Pd foil reference by fixing CN as the known crystallographic value.

Sample	Shell	N[a]	R(Å)[b]	σ^2(Å^2)[c]	ΔE_0(eV)[d]	R factor
Pd foil	Pd-Pd	12	2.74	0.0056	3.6	0.0013
Pd	Pd-Pd	8.5	2.73	0.0067	-4.9	0.0028
h-BN/C/Pd:17	Pd-N/B	0.5	2.33	0.0008	-6.1	0.0013
	Pd-Pd	8.6	2.71	0.0063		
h-BN/Pd:17	Pd-N/B	0.4	2.32	0.0008	-6.6	0.0010
	Pd-Pd	8.4	2.72	0.0060		

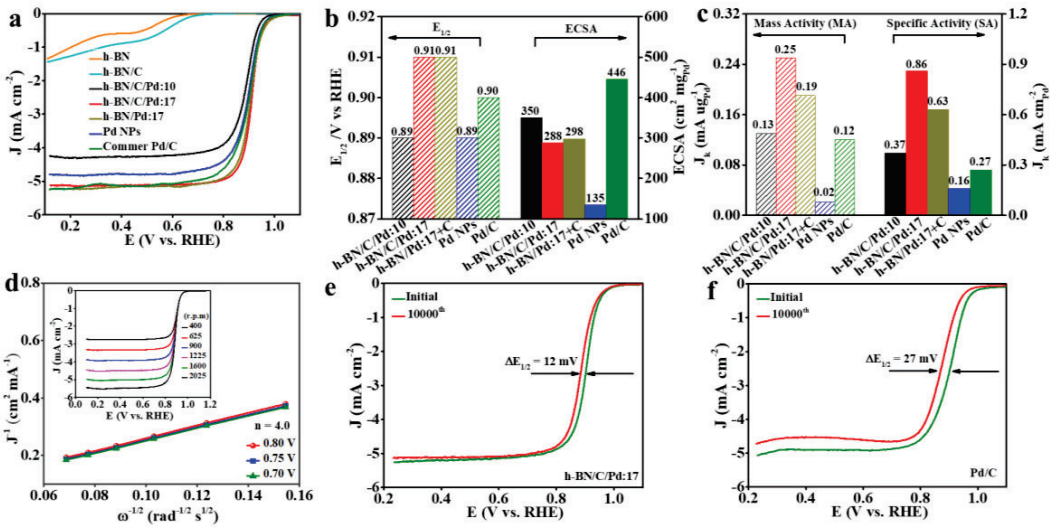

Figure 6.12. The comparison of electrochemical performance for as-prepared h-BN/C/Pd, h-BN/Pd, Pd NPs and commercial Pd/C. (a) The LSV curves performed at 1600 r.p.m. (b) The corresponding half-wave potential and ECSA (surface area normalized to mass). (c) The specific and mass activities normalized by the ECSA or the total mass of the loaded Pd, respectively. (d) The number of transfer electron determined by the LSV curves measured from 400 to 2025 r.p.m (i.e. the inset). (e) and (f) The LSV curves of h-BN/C/Pd:17 and commercial Pd/C before and after 10000 cycles in O_2-saturated 0.1M KOH, respectively.

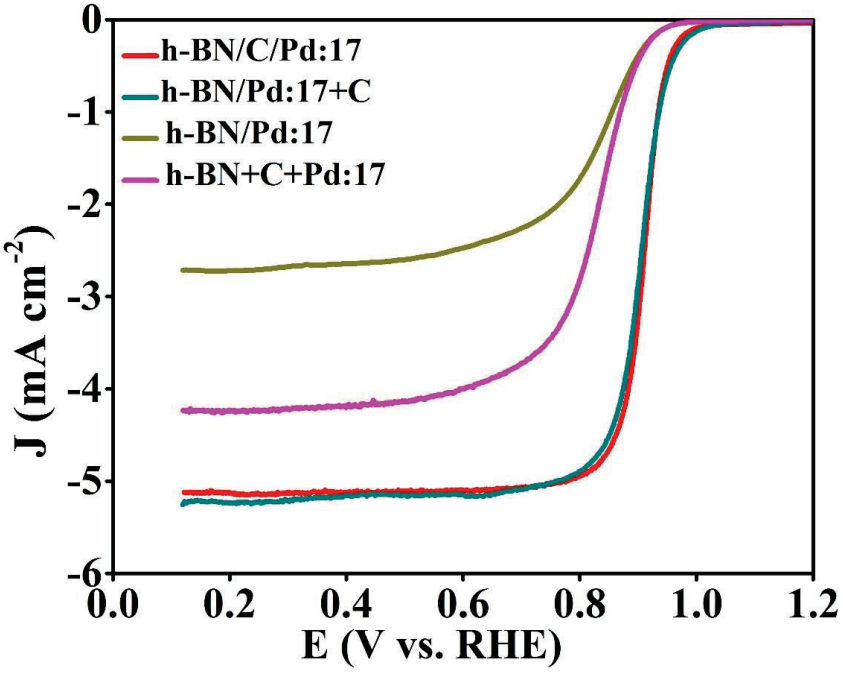

Figure 6.13. The comparison of polarization profiles for h-BN/C/Pd:17, h-BN/Pd:17, h-BN/Pd:17+C, and

h-BN+C+Pd:17.

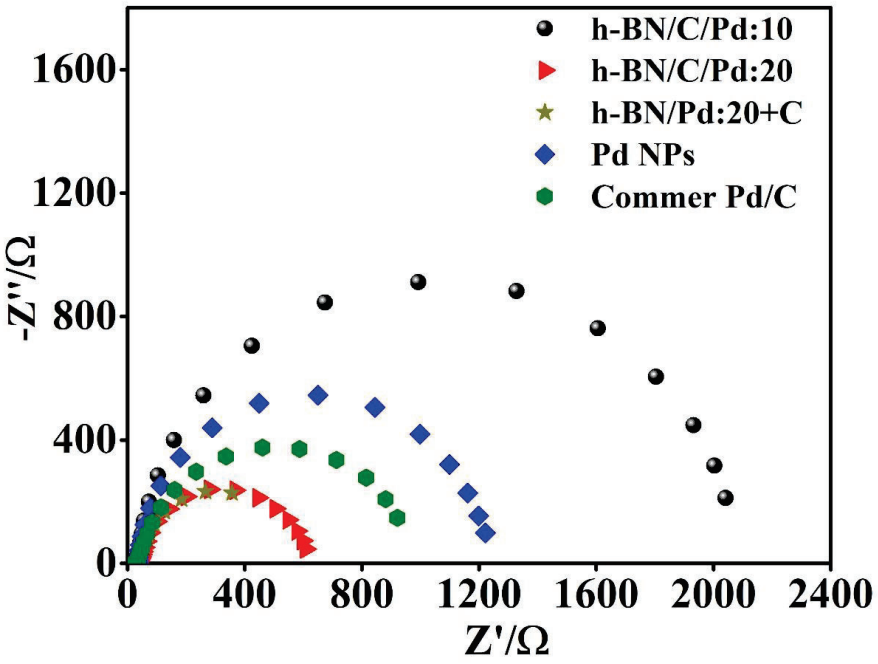

Figure 6.14. EIS of h-BN/C/Pd, h-BN/Pd, Pd NPs and commercial Pd/C tested at 0.87 V (vs. RHE).

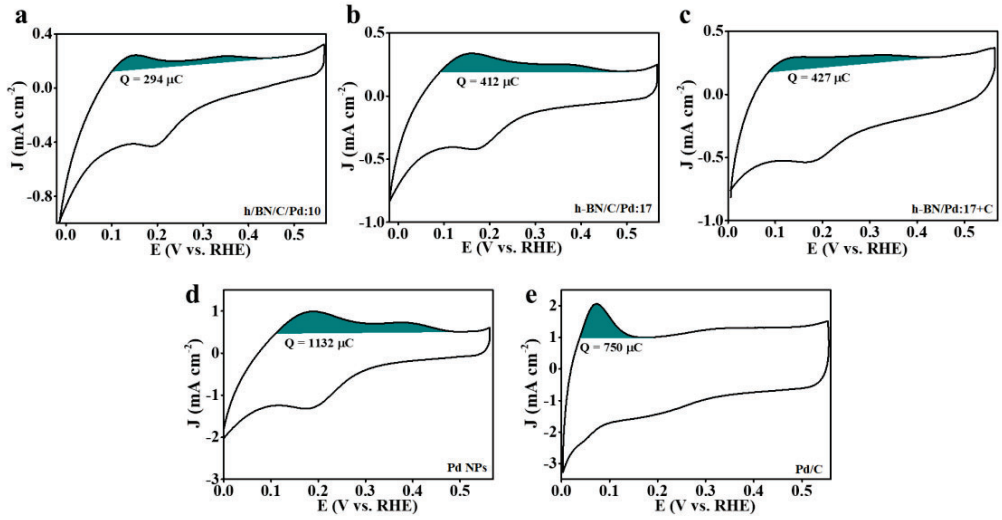

Figure 6.15. The CVs test in N_2-saturated 0.1M KOH for ECSA calculation of (a) h-BN/C/Pd:10, (b) h-BN/C/Pd:17, (c) h-BN/Pd:17, (d) Pd NPs and (e) Commercial Pd/C. Scan rates: 50 mV s^{-1}.

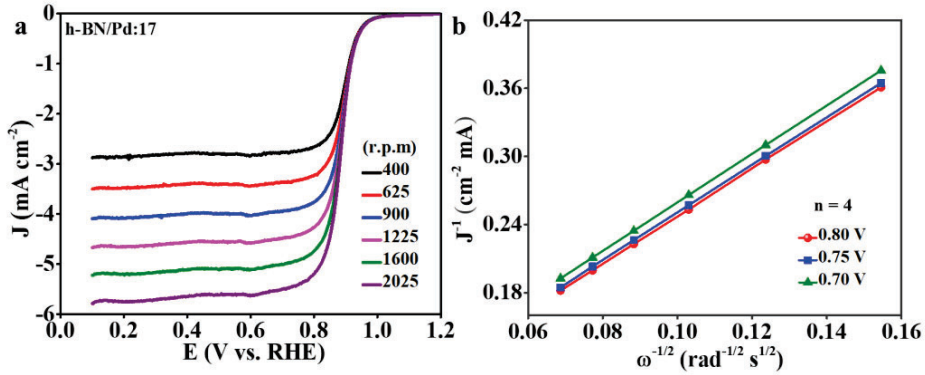

Figure 6.16. (a) The LSV curves of h-BN/Pd:17 measured from 400 to 2025 r.p.m and (b) the numbers of transfer electron calculated from (a).

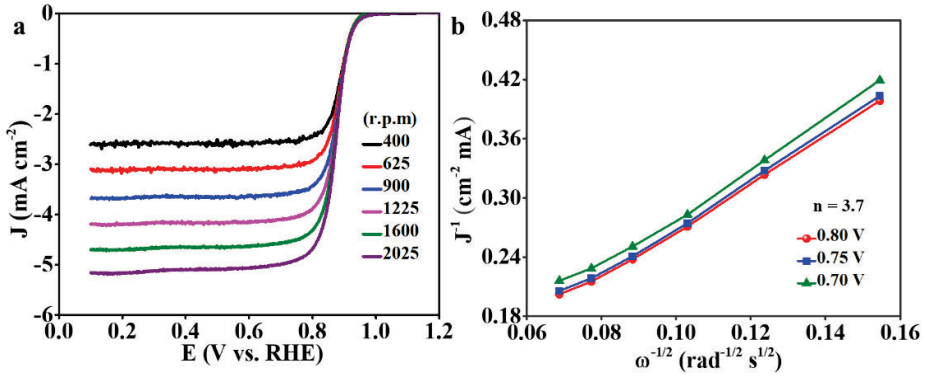

Figure 6.17. (a) The polarization profiles measured from 400 to 2025 r.p.m and (b) the numbers of transfer electron calculated from (a).

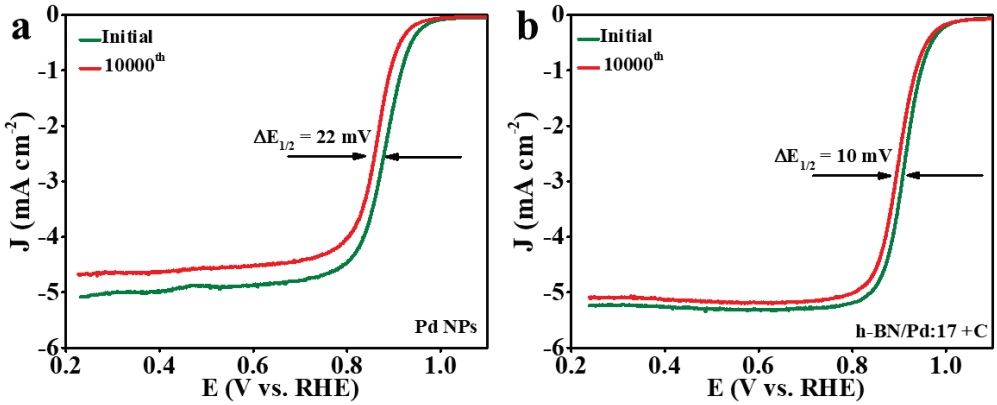

Figure 6.18. The LSV curves of (a) Pd NPs, and (b) h-BN/Pd:17+C before and after 10000 cycles in O_2-saturated 0.1M KOH.

The ORR catalytic activities of the electrocatalysts were evaluated in 0.1 M KOH aqueous solution by the typical rotating disk electrode (RDE) method. **Figure 6.12a** displays that the h-BN/C/Pd:17 and h-BN/Pd:17+C (adding 6 wt% conductive carbon (Vulcan XC-72)) heterostructured electrocatalysts deliver the best catalytic activity, much superior to Pd NPs and commercial Pd/C (20 wt.%). It can be also found that h-BN and h-BN/C nanosheets are electrochemically inert for ORR. As shown in **Figure 6.12b**, h-BN/C/Pd:17 and h-BN/Pd:17+C exhibit much higher half-wave potential ($E_{1/2}$) of 0.91 V vs. RHE than that of h-BN/C/Pd:10 (0.89 V), Pd NPs (0.89 V) and commercial Pd/C (0.90 V). These results clearly infer that the promotion of catalytic activity for h-BN/C/Pd:17 heterostructures should be closely associated with the inactive h-BN nanosheets. Notably, the ORR activity of h-BN/Pd:17 without coating carbon layer on h-BN nanosheets is much more inferior (**Figure 6.13**), while the activity is substantially enhanced and reaches as high as that of h-BN/C/Pd:17 after adding 6 wt% conductive carbon. Besides, as compared with h-BN/C/Pd:17 and h-BN/Pd:17+C, the lower activity of h-BN+C+Pd:17 (17% Pd and 6% conductive carbon physically mixed with h-BN) further reveal that the electronic modulation between Pd and h-BN is greatly important to the enhanced ORR kinetics. According the EIS results, the h-BN/C/Pd:17 and h-BN/Pd:17+C show close charge-transfer resistances, indicating that the carbon layer and carbon black make similar contributions to the charge transfer process (**Figure 6.14**). The results reveal that both the carbon layer and electronic structure modulation at the interface play negligible roles in the enhancement of catalytic activity. The electrochemical active surface area (ECSA) normalized to active Pd mass was determined by cyclic voltammograms (**Figure 6.12b and 6.15**). The h-BN/C/Pd:17, h-BN/Pd:17+C, h-BN/C/Pd:10, bare Pd NPs, and commercial Pd/C samples display the ECSA of 288, 298, 350, 446, and 135 $cm^2\ mg^{-1}_{Pd}$, respectively. For a better evaluation of catalytic activity, the mass activity (MA) and specific activity (SA) normalized by Pd metal at 0.9 V (vs. RHE) can be calculated (**Figure 6.12c**). The MA of h-BN/C/Pd:17 reaches up to 0.25 mA μg^{-1}_{Pd}, around 2 times higher than those of h-BN/C/Pd:10 and commercial Pd/C, and even 10 times greater than that of Pd NPs. The SA of h-BN/C/Pd:17 is 0.86 mA cm^{-2}_{Pd}, which is also dramatically superior to those of commercial Pd/C and Pd NPs. To further assess the reaction kinetics of the heterostructured catalysts, the linear sweep voltammetry (LSV) curves were collected at various rotation rates from 400 to 2,025 r.p.m in O_2-saturated 0.1 M KOH solution. **Figure 6.12d** shows that the electron transfer number of ORR on h-BN/C/Pd:17, which is calculated according to the Koutecky–Levich equation, is around 4.0 at 0.7–0.8 V. Meanwhile, the electron transfer is also 4.0 for the h-BN/Pd:17+C, while the value of Pd NPs

approximates 3.7 (**Figure 6.16 and 6.17**), revealing that the heterostructured catalysts achieve an enhanced selectivity toward $4e^-$ reaction process and almost complete reduction of O_2 to H_2O. In order to evaluate the durability of the electrocatalysts, CV measurements were performed at a sweep rate of 100 mV s^{-1}. After 10000 sweeping cycles, the $E_{1/2}$ for h-BN/C/Pd:17 and h-BN/Pd:17+C show very little negative shift of ~12 and ~10 mV before and after durability test. In contrast, Pd NPs and commercial Pd/C exhibit significant activity degradation, which decays the $E_{1/2}$ of ~22 and ~27 mV, respectively (**Figure 6.12d, e and 6.18**). Therefore, it can come to a conclusion that the incorporation of h-BN substrate could efficiently promote the ORR activity, selectivity and durability of Pd active centers.

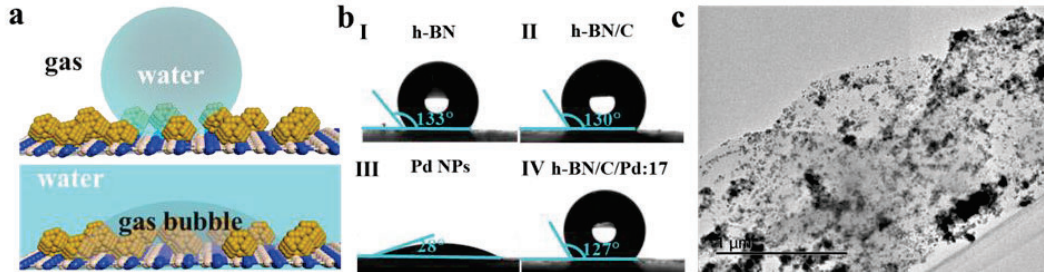

Figure 6.19. (a) Schematic illustration of the wetting state of superhydrophobic surface in air and water, respectively. (b) The measurement of the contact angle for h-BN/C/Pd:17, h-BN, h-BN/C and Pd NPs. (c) TEM image for h-BN/C/Pd:17 after 10000 cycles.

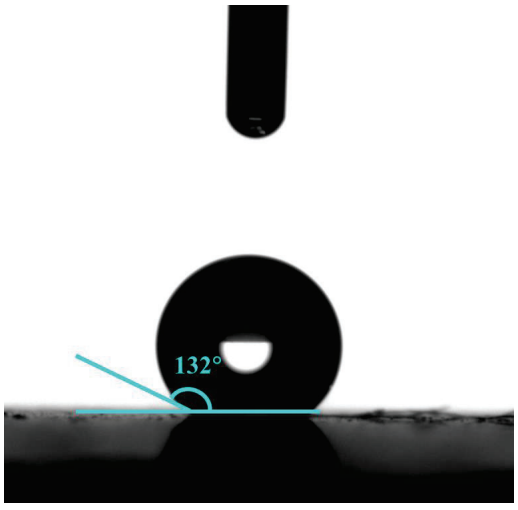

Figure 6.20. The contact angle of h-BN/Pd:17.

The exceptional catalytic performance of the h-BN/C/Pd:17 heterostructure can be ascribed to several synergistic factors as detailed below, all of which are closely related to the incorporation of multifunctional h-BN nanosheets.

Firstly, the h-BN nanosheets provide B- and N-abundant coordination environment and induce intense

electronic interaction with Pd at the heterostructure interface. The h-BN substrate can induce compressive strain on Pd surface and decrease the electron density of Pd, which efficiently lead to a downshift of Pd d-band centre. The modulations are beneficial to weaken the bonding strength of the reaction intermediate species on Pd surface accordingly. The reduced bonding strength can effectively accelerate the intermediates desorption and facilitate the formation of water.[24, 39] On the other hand, the h-BN nanosheets, serving as the catalyst supports, can uniformly disperse Pd NPs, and this could ensure the maximum exposure of active sites and hence higher ECSA. Therefore, the h-BN nanosheets can not only enhance the intrinsic activity but also improve the density of active sites of Pd.

Secondly, the hydrophobicity (aerophilicity) of the heterostructured catalysts is substantially improved after incorporating superhydrophobic h-BN nanosheets, which means much better gas affinity in the KOH solution (**Figure 6.19a**). Basically, superhydrophobicity (superaerophilicity) is a highly desired property of electrocatalysts for gas reduction and oxidation reactions, which is crucial for achieving fast gas diffusion at the catalyst surface.[21, 23] As shown in **Figure 6.19b-6.20**, the contact angle increases from 28° for bare Pd NPs to ~130° and ~132° for the heterostructures, very close to h-BN nanosheets (133°). Under this circumstance, the hydrophobic heterostructured catalyst surface is highly beneficial to promote the adsorption of O_2 and hence facilitate ORR kinetics.

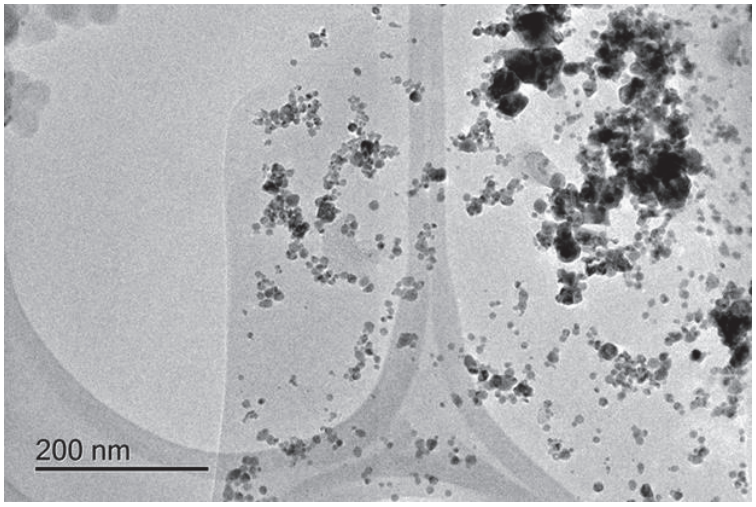

Figure 6.21. TEM images for h-BN/Pd:17+C after 10000 cycles.

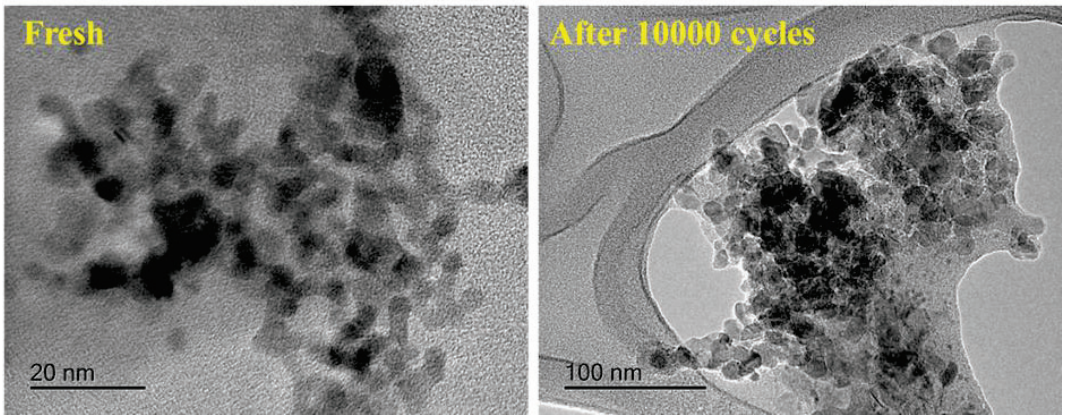

Figure 6.22. TEM images for Pd NPs before and after 10000 cycles.

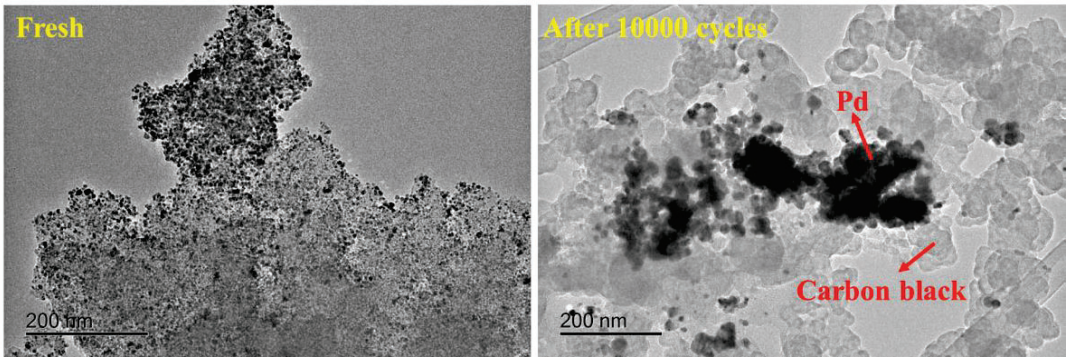

Figure 6.23. TEM images for commercial Pd/C before and after 10000 cycles.

Finally, the highly stability of h-BN nanosheets is another vital reason for the exceptional catalytic activity, particularly the durability of the heterostructured catalysts. The TEM images show that Pd still maintains the uniform dispersion on h-BN support after long cycling as compared with Pd NPs and commercial Pd/C (**Figure 6.19c and 6.21-23**), indicating the excellent structure stability of h-BN/C/Pd:17 and h-BN/Pd:17. These results further suggest that the h-BN can efficiently confine the Pd NPs via strong interfacial coupling to assure the structure integrity of heterostructures and high catalytic activity.

6.4. Conclusion

In summary, h-BN nanosheets are for the first time demonstrated as a multifunctional support for engineering durable and efficient heterostructured electrocatalysts for ORR. The multifunctional h-BN as a platform not only suppresses the agglomeration of Pd NPs, maximizing the exposure of active sites, but also endows the heterostructures with a superhydrophobic surface, facilitating the adsorption capability and diffusion kinetics of O_2. More importantly, due to the strongly chemical confinement of robust h-BN NSs, Pd achieves compressive strain and descending surface electron density, which lead to the downshift

of Pd d-band center, and accordingly weakening the adsorption capability of intermediates on Pd active centers. Therefore, these results further demonstrate that engineering heterostructures with well-defined interface provides a feasible strategy for the application in catalytic field.

6.5. References

[1] M. A. Newton, Chem. Soc. Rev. 2008, 37, 2644-2657.

[2] B. R. Cuenya, Thin Solid Films 2010, 518, 3127-3150.

[3] Y. Xu, B. Zhang, Chemical Society Reviews 2014, 43, 2439-2450.

[4] L. Du, Y. Shao, J. Sun, G. Yin, J. Liu, Y. Wang, Nano Energy 2016, 29, 314-322.

[5] B.-W. Zhang, Z.-C. Zhang, H.-G. Liao, Y. Gong, L. Gu, X.-M. Qu, L.-X. You, S. Liu, L. Huang, X.-C. Tian, R. Huang, F.-C. Zhu, T. Liu, Y.-X. Jiang, Z.-Y. Zhou, S.-G. Sun, Nano Energy 2016, 19, 198-209.

[6] X. Zhou, J. Qiao, L. Yang, J. Zhang, Adv. Energy Mater. 2014, 4, 1301523-1301547.

[7] Z. Zhuang, S. A. Giles, J. Zheng, G. R. Jenness, S. Caratzoulas, D. G. Vlachos, Y. Yan, Nat. Commun. 2016, 7, 10141-10148.

[8] J. P. Meyers, R. M. Darling, J. Electrochem. Soc. 2006, 153, A1432-A1442.

[9] J. Chen, J. B. Siegel, T. Matsuura, A. G. Stefanopoulou, J. Electrochem. Soc. 2011, 158, B1164-B1174.

[10] Y. Shao-Horn, W. C. Sheng, S. Chen, P. J. Ferreira, E. F. Holby, D. Morgan, Top. Catal. 2007, 46, 285-305.

[11] S. Maass, F. Finsterwalder, G. Frank, R. Hartmann, C. Merten, J. Power Sources 2008, 176, 444-451.

[12] W. Zhu, Z. Wu, G. S. Foo, X. Gao, M. Zhou, B. Liu, G. M. Veith, P. Wu, K. L. Browning, H. N. Lee, H. Li, S. Dai, H. Zhu, Nat. Commun. 2017, 8, 15291-15297.

[13] A. Guha, T. Veettil Vineesh, A. Sekar, S. Narayanaru, M. Sahoo, S. Nayak, S. Chakraborty, T. N. Narayanan, ACS Catal. 2018, 8, 6636-6644.

[14] J. Li, N. Lei, L. Guo, Q. Song, Z. Liang, ChemElectroChem 2017, 10.1002/celc.201701056, n/a-n/a.

[15] Q. Zhang, J. Yu, P. Ebert, C. Zhang, C.-R. Pan, M.-Y. Chou, C.-K. Shih, C. Zeng, S. Yuan, ACS Nano 2018, 10.1021/acsnano.8b04444.

[16] Z. Liu, Y. Gong, W. Zhou, L. Ma, J. Yu, J. C. Idrobo, J. Jung, A. H. MacDonald, R. Vajtai, J.

Lou, P. M. Ajayan, Nat. Commun. 2013, 4, 2541-2548.

[17] J. Zhang, Y. Yang, J. Lou, Nanotechnology 2016, 27, 364004-364010.

[18] F. Mahvash, S. Eissa, T. Bordjiba, A. C. Tavares, T. Szkopek, M. Siaj, Sci. Rep. 2017, 7, 42139-42113.

[19] W. Lei, D. Portehault, D. Liu, S. Qin, Y. Chen, Nat. Commun. 2013, 4, 1777-1783.

[20] Y. Ide, F. Liu, J. Zhang, N. Kawamoto, K. Komaguchi, Y. Bando, D. Golberg, J. Mater. Chem. A 2014, 2, 4150-4156.

[21] W. Xu, Z. Lu, X. Sun, L. Jiang, X. Duan, Acc. Chem. Res. 2018, 51, 1590-1598.

[22] C. Yu, P. Zhang, J. Wang, L. Jiang, Adv. Mater. 2017, 29, 1703053-1703065.

[23] P. Wang, T. Hayashi, Q. a. Meng, Q. Wang, H. Liu, K. Hashimoto, L. Jiang, Small 2017, 13, 1601250-1601256.

[24] P. Strasser, S. Koh, T. Anniyev, J. Greeley, K. More, C. Yu, Z. Liu, S. Kaya, D. Nordlund, H. Ogasawara, M. F. Toney, A. Nilsson, Nat. Chem. 2010, 2, 454.

[25] M. Luo, S. Guo, Nature Reviews Materials 2017, 2, 17059.

[26] M. Chen, D. Kumar, C.-W. Yi, D. W. Goodman, Science 2005, 310, 291-293.

[27] G. E. McGuire, G. K. Schweitzer, T. A. Carlson, Inorg. Chem. 1973, 12, 2450-2453.

[28] Z. Chen, Y. Song, J. Cai, X. Zheng, D. Han, Y. Wu, Y. Zang, S. Niu, Y. Liu, J. Zhu, X. Liu, G. Wang, Angew. Chem. Int. Ed. 2018, 57, 5076-5080.

[29] Z. Liu, K. Handa, K. Kaibuchi, Y. Tanaka, J. Kawai, Spectrochim. Acta Part B At. Spectrosc. 2004, 59, 901-904.

[30] J. E. Müller, O. Jepsen, J. W. Wilkins, Solid State Commun. 1982, 42, 365-368.

[31] M. Tromp, J. A. van Bokhoven, G. P. F. van Strijdonck, P. W. N. M. van Leeuwen, D. C. Koningsberger, D. E. Ramaker, J. Am.Chem. Soc. 2005, 127, 777-789.

[32] V. Stamenkovic, B. S. Mun, K. J. J. Mayrhofer, P. N. Ross, N. M. Markovic, J. Rossmeisl, J. Greeley, J. K. Nørskov, Angew. Chem. Int. Ed. 2006, 45, 2897-2901.

[33] L. Zhang, G. Zhou, J. Chem. Phys. 2016, 144, 144706-144711.

[34] Y. Suo, L. Zhuang, J. Lu, Angewandte Chemie 2007, 119, 2920-2922.

[35] M.-H. Shao, K. Sasaki, R. R. Adzic, J. Am. Chem. Soc. 2006, 128, 3526-3527.

[36] G. Wang, J. Guan, L. Xiao, B. Huang, N. Wu, J. Lu, L. Zhuang, Nano Energy 2016, 29, 268-274.

[37] A. M. Beale, B. M. Weckhuysen, Physical Chemistry Chemical Physics 2010, 12, 5562-5574.

[38] S. Mukerjee, J. McBreen, J. Electroanal. Chem. 1998, 448, 163-171.

[39] A. Nilsson, L. G. M. Pettersson, B. Hammer, T. Bligaard, C. H. Christensen, J. K. Nørskov, Catal. Lett. 2005, 100, 111-114.

[40] W. Zhu, X. Gao, Q. Li, H. Li, Y. Chao, M. Li, S. M. Mahurin, H. Li, H. Zhu, S. Dai, Angew.Chem. Int. Ed. 2016, 55, 10766-10770.

[41] M. Newville, J. Synchrotron Rad. 2001, 8, 322-324.

[42] B. R. M. Newville, J. Synchrotron Rad. 2005, 12, 537-541.

Chapter 7

7. General Conclusions and Outlook

7.1. General Conclusions

In this doctoral thesis work, heterostructured electrocatalysts with well-defined interface towards enhanced OER, HER, and ORR kinetics are summarized. The construction of heterointerface in three heterostructured electrocatalysts has created a series of novel physicochemical properties and synergistic effects, efficiently optimizing the affinity of reactants, intermediate species, or products, and facilitating the electrocatalytic kinetics.

Specifically, in GCNN heterostructures, owing to the superhydrophilicity of functionalized GCN, the surface wettability of GCNN (contact angle 0°) was substantially improved as compared with bare $Ni(OH)_2$ (contact angle 21°). Besides, GCN nanosheets can effectively suppress $Ni(OH)_2$ aggregation to help expose more active sites. Benefiting from the well-defined catalyst surface/interface, the optimal GCNN hybrid showed significantly enhanced electrochemical performance over bare $Ni(OH)_2$ nanosheets, although GCN is electrochemically inert.

For the $MoSe_2/SnS_2$ heterostructures, due to the presence of SnS_2 quantum dots, the dissociation kinetics of the heterostructures and water adsorption capability of $MoSe_2$ nanosheets can be significantly enhanced. Meanwhile, the coupled SnS_2 via strong chemical bonds at the interface of heterostructures efficiently avoids the agglomeration of active $MoSe_2$ nanosheets, facilitating to maintain the exposure of active sites. As a results, the optimal $MoSe_2/SnS_2$ heterostructured catalysts delivers a much lower overpotential of 285 mV than $MoSe_2$ (367 mV) to reach a current density of 10 mA cm^{-2} in 1 M KOH. DFT calculations further reveal that the presence of SnS_2 significantly promotes the water adsorption capability of $MoSe_2$ nanosheets.

In h-BN/Pd heterostructured electrocatalysts, the robust h-BN were served as a durable platform to ensure the structural integrity of the heterostructured catalyst, uniform distribution of Pd NPs and maximal exposure of the active sites. More importantly, the h-BN is capable of modulating the electronic structure of Pd active centers by establishing unique heterostructrued interfaces, downshifting the position of Pd d-band center accordingly and eventually optimizing the affinity with the reaction intermediates for faster reaction kinetics. Meanwhile, due to the presence of superhydrophobic h-BN, an unique

superhydrophobic surface of the heterostructures have been created, which promoted the adsorption capability and diffusion kinetics of O_2. As a results, benefiting from the favorable characters of constructing well-defined heterointerface, the optimal heterostructured catalyst delivers exceptional ORR catalytic performance with a high half-wave potential, enhanced mass and specific activity, and decent durability. Therefore, engineering well-defined heterointerface based on 2D-material-based heterostructures is a promising strategy for electrocatalysis applications.

7.2. Outlook

Even though substantial efforts have been devoted to the design and development of 2Dmaterial-based heterostructured electrocatalysts with well-defined interface, the precisely controllable synthesis and cost-effective commercial applications remain challenging. Therefore, more attentions should be paid to developing 2D material-based heterostructures in the following aspects:

Firstly, one of the greatest challenges relies on how to achieve precisely controllable construction and understanding of hetero-interface in 2D nanomaterial-based heterostructures with desired chemical composition, coordination chemistry, and geometric structure.

Secondly, although there have been remarkable progresses in the development of high-performance 2D heterostructured electrocatalysts, some fundamental principles for their activity origins and relevant structure-property relationships in many electrocatalytic processes are still unclear. For example, the obstacles facing the alkaline HER and acidic OER are their inconclusive activity descriptors. This is mainly because of the limited approaches to monitoring the real electrocatalytic reaction processes and the complex interface chemistry of the heterostructured electrocatalysts.

Thirdly, ex-situ advanced characterizations have been extensively applied in the investigation of the structure evolution of the electrocatalyst over the electrochemcial reactions. However, these technologies cannot probe the most important factors, i.e. the reaction intermediates, during the electrocatalytic processes. Appropriate *in-situ* and operando characterization techniques (such as *in-situ* TEM, XAS, XPS, IR, and Raman) need to be developed to gain more in-depth understanding of the electrochemical reactions and to clearly unravel relevant fundamental mechanisms.

Finally, the practical application of 2D material-based heterostructured electrocatalysts is still a big concern. The large-scale production and cost of electrocatalysts are still bottlenecks towards commercial application. Further, specific efforts should also be made to evaluate the catalytic performance in

prototype devices.

Appendix A: Publications

1. **Yaping Chen**, Xingyong Wang, Mengmeng Lao, Kun Rui, Xiaobo Zheng, Haibo Yu*, Jing Ma, Shi Xue Dou, Wenping Sun*. Electrocatalytically inactive SnS_2 promotes water adsorption/dissociation on molybdenum dichalcogenides for accelerated alkaline hydrogen evolution. **Nano Energy** 2019, 64, 103918.
2. **Yaping Chen**, Qian Zhou, Guoqiang Zhao, Zhenwei Yu, Xiaolin Wang, Shi Xue Dou, Wenping Sun*. Electrochemically Inert g‐C_3N_4 Promotes Water Oxidation Catalysis. **Adv. Funct. Mater.** 2018, 28, 1705583.
3. **Yaping Chen**, Kun Rui*, Jixin Zhu, Shi Xue Dou, Wenping Sun*. Recent Progress on Nickel‐Based Oxide/(Oxy) Hydroxide Electrocatalysts for the Oxygen Evolution Reaction. **Chem. Eur. J.** 2019, 25, 703.
4. Jiayi Chen, Dr. Peixin Cui, Guoqiang Zhao, Dr. Kun Rui, Mengmeng Lao, **Yaping Chen**, Dr. Xusheng Zheng, Prof. Yinzhu Jiang, Prof. Hongge Pan, Prof. Shi Xue Dou, Dr. Wenping Sun*. Low‐Coordinate Iridium Oxide Confined on Graphitic Carbon Nitride for Highly Efficient Oxygen Evolution. **Angew. Chem. Int. Ed.** 2019, 58.
5. Xiaobo Zheng, **Yaping Chen**, Xusheng Zheng, Guoqiang Zhao, Kun Rui, Peng Li, Xun Xu, Zhenxiang Cheng, Shi Xue Dou, Wenping Sun*. Electronic Structure Engineering of $LiCoO_2$ toward Enhanced Oxygen Electrocatalysis. **Adv. Energy Mater**. 2019, 9, 1803482.
6. Guoqiang Zhao, Xingyong Wang, Shaolan Wang, Kun Rui, **Yaping Chen**, Haibo Yu*, Jing Ma, Shi Xue Dou, Wenping Sun*. Heteroatom‐doped $MoSe_2$ Nanosheets with Enhanced Hydrogen Evolution Kinetics for Alkaline Water Splitting. **Chem. Asian J.** 2019, 14, 301.
7. Jiayi Chen Guoqiang Zhao Yaping Chen Dr. Kun Rui Dr. Hui Mao Prof. Shi Xue Dou Dr. Wenping Sun*. Iron‐Doped Nickel Molybdate with Enhanced Oxygen Evolution Kinetics. Chem. Eur. J. 2019, 25, 280.
8. Qian Zhou, Guoqiang Zhao, Kun Rui, **Yaping Chen**, Xun Xu*, Shi Xue Dou, Wenping Sun*. Engineering additional edge sites on molybdenum dichalcogenides toward accelerated alkaline hydrogen evolution kinetics. **Nanoscale**, 2019, 11, 717-724.
9. Liangqi Gui, **Yaping Chen**, Beibei He, Geng Li, Jianmei Xu, Qing Wang, Wenping Sun, Ling Zhao*. Nickel‐Based Bicarbonates as Bifunctional Catalysts for Oxygen Evolution and Reduction Reaction in Alkaline Media. **Chem. Eur. J.** 2018, 24, 17665.

10. Guoqiang Zhao, Peng Li, Dr. Kun Rui, **Yaping Chen,** Prof. Shi Xue Dou, Dr. Wenping Sun*. $CoSe_2/MoSe_2$ Heterostructures with Enriched Water Adsorption/Dissociation Sites towards Enhanced Alkaline Hydrogen Evolution Reaction**. Chem. Eur. J.** 2018, 24, 11158.
11. Qian Zhou, **Yaping Chen**, Guoqiang Zhao, Yue Lin*, Zhenwei Yu, Xun Xu*, Xiaolin Wang, Hua Kun Liu, Wenping Sun*, Shi Xue Dou. Active-Site-Enriched Iron-Doped Nickel/Cobalt Hydroxide Nanosheets for Enhanced Oxygen Evolution Reaction. **ACS Catal.** 2018, 86, 5382-5390.
12. Guoqiang Zhao, Yue Lin*, Kun Rui, Qian Zhou, **Yaping Chen**, Shi Xue Dou, Wenping Sun*. Epitaxial growth of $Ni(OH)_2$ nanoclusters on MoS_2 nanosheets for enhanced alkaline hydrogen evolution reaction. **Nanoscale**, 2018, 10, 19074-19081.
13. Mengmeng Lao, Guoqiang Zhao, Xin Li, **Yaping Chen,** Shi Xue Dou, Wenping Sun*. Homogeneous Sulfur–Cobalt Sulfide Nanocomposites as Lithium–Sulfur Battery Cathodes with Enhanced Reaction Kinetics. **ACS Appl. Energy Mater**.2018, 11, 167-172.

Appendix B: Conferences & Activities

1. The 2016 International Symposium on Innovative Materials and Physics, North Wollongong, Australia, 20^{th} – 22^{nd} of November 2016

2. The 2019 International Symposium on Future Materials, North Wollongong, Australia, 30^{th} Jan – 1^{st} of Feb 2019

3. 2019 UOW-USTC Joint Research Workshop, North Wollongong, Australia, 19^{th} – 21^{st} of Aug 2019

Appendix C: Scholarships & Awards

1. 2016-2020 UOW-CSC Joint Scholarship